The Interplay of System Dynamics and Dry Friction: Shakedown, Ratcheting and Micro-Walking

vorgelegt von
Dipl.-Ing. Robbin Wetter
geb. in Berlin

von der Fakultät V Verkehrs- und Maschinensysteme
der Technischen Universität Berlin
zur Erlangung des akademischen Grades

Doktor der Ingenieurwissenschaften
- Dr.-Ing. -

genehmigte Dissertation

Promotionsausschuss

Vorsitzender:	Prof. Dr.-Ing. Christian Oliver Paschereit
Gutachter:	Prof. Dr. rer. nat. Valentin L. Popov
Gutachter:	Prof. Dr.-Ing. habil. Manfred Zehn
Gutachter:	Dr. Sc. Alexander Filippov

Tag der wissenschaftlichen Aussprache: 27. Januar 2016

Berlin 2016

Acknowledgements

This thesis was created during my work as a scientific assistant at the Department of System Dynamics and Friction Physics at the Institute of Mechanics at the Technische Universität Berlin. I am especially grateful to my supervisor and chair of the department Prof. Valentin Popov for his guidance and continued support. His encouragements and his many helpful suggestions as well the great freedom during my work were essential to me. I also thank Prof. Manfred Zehn and Prof. Alexander Filippov for their work as referees in the doctoral committee and many valuable discussions. Their quick assessment was a great help in the special situation after the death of Professor Zygmunt Rymuza in December 2015. I am also grateful to Prof. Christian Paschereit for taking the chair of the doctoral committee.

The ten years at the department were a very special time for me and I am very grateful for having met so many inspiring colleagues and friends. In particular, I would like to thank Roman Pohrt for his willingness to discuss so many ideas, Tobias Rademacher for his thorough proofreading and Jasminka Starcevic for her help in the laboratory. Last but not least I would like to thank my wonderful wife Miriam for her patience and support without which this work would not have been possible.

Abstract

This thesis discusses the influence of vibrations in dynamic systems with dry friction. Force locked connections such as screws, bolts and interference fits are in practice often subject to external vibrations. This may lead to an incremental slip of the contact interface and failure of the connection, even if the tangential force is insufficient to cause complete sliding. Vibrations also affect systems with gross sliding such as brakes, clutches and joints. Their frictional resistance strongly depends on system dynamics and its corresponding variables such as mass, velocity and stiffness.

As a generic model for a force locked connections under the influence of vibrations, the so called oscillating rolling contact is introduced. It consists of a tangentially loaded contact between two bodies, where the upper body follows an oscillating rocking motion. For the analysis the well-known Method of Dimensionality Reduction (MDR) is used and three-dimensional simulations are performed. In addition, an experimental rig is used for comparison. The results show that the oscillatory rolling influences the pressure distribution and the contact region. Together with the tangential load, this rocking motion causes incremental sliding processes and a macroscopic rigid body motion. In case that the rolling amplitude is sufficiently small, the slip ceases after the first few periods. The residual force in the contact withstands the tangential load and the system reaches a new equilibrium: a so called *shakedown* occurs. Otherwise a continuing macroscopic rigid body motion is induced where one side of the contact alternately sticks, while the other slips. This effect is referred to as *ratcheting*. Using the MDR analytical failure criteria, i.e. the so called shakedown limits, are derived as a function of the rolling amplitude and the tangential load. These are in very good agreement with the experimental results and the three-dimensional simulations. Furthermore, the incremental shift per period in case of ratcheting is determined.

In order to examine the influence of system dynamics on sliding friction, the micro-walking machine is introduced as a model. It consists of a rigid body with a number of elastic contact spots that is pulled by a constantly moving base. In addition to an experimental rig, numerical integration and an extensive parameter study are used for the analysis. The results show that the frictional resistance almost vanishes if a certain parameter range is met. If so, self-excited oscillations occur that lead to a particular dynamic mode where the motion is characterized by a strong correlation between low or even zero normal forces and a fast forward motion. This effect is referred to as *micro-walking* and leads to a theoretical reduction of the frictional resistance of up to 98 %. These results are confirmed by the experiments where the maximal reduction is 73 %.

Following the analysis and identification of the relevant parameter ranges for all of the three effects, their occurrence in technical systems discussed. In addition guidelines are given for possible technical applications.

Kurzzusammenfassung

Diese Arbeit beschreibt den Einfluss von Vibrationen in dynamischen Systemen mit trockener Reibung. Kraftschlüssige Verbindungen wie Schrauben, Bolzen und Presspassungen sind in der Praxis häufig externen Vibrationen ausgesetzt. Dies kann zu einem inkrementellen Schlupf in der Kontaktfläche und einem Versagen der Verbindung führen, auch wenn die Tangentialkraft nicht ausreicht, vollständiges Gleiten zu erzeugen. Vibrationen beeinflussen ebenso das Verhalten von Systemen, in denen komplettes Gleiten auftritt. Beispiele hierfür sind Bremsen, Kupplungen und Gelenke. Deren Reibwiderstand hängt stark von der Systemdynamik und den Einflussgrößen wie Masse, Geschwindigkeit oder Steifigkeit ab.
Als allgemeines Modell einer kraftschlüssigen Verbindung unter dem Einfluss von Vibrationen dient der sogenannte oszillierende Rollkontakt. Dieser besteht aus einem tangential belasteten Kontakt zweier Körper, wobei der obere eine oszillierende Wipp-Bewegung ausführt. Für die Analyse werden die Methode der Dimensionsreduktion (MDR) verwendet und dreidimensionale Simulationen durchgeführt. Ein Versuchsstand dient zur Verifikation. Es zeigt sich, dass das oszillierende Rollen die Druckverteilung und die Kontaktfläche variiert. Zusammen mit der tangentialen Belastung erzeugt dies ein inkrementelles Gleiten und eine makroskopische Starrkörperbewegung. Im Falle einer ausreichend kleinen Rollamplitude stoppt das Gleiten nach einigen Perioden. Die Restkraft im Kontakt widersteht der tangentialen Belastung und das System erreicht einen neuen Gleichgewichtszustand: ein sogenannter *Shakedown* tritt auf. Andernfalls wird eine fortgesetzte Starrkörperbewegung induziert, bei der abwechselnd eine Seite des Kontaktes haftet, während die andere gleitet. Dies wird als *Ratcheting* bezeichnet. Mit Hilfe der MDR werden Versagenskriterien als Funktion der Rollamplitude und der Tangentialkraft hergeleitet. Diese sogenannten Shakedown-Grenzen stimmen sehr gut mit den experimentellen Ergebnissen und den dreidimensionalen Simulationen überein. Zusätzlich wird für den Fall des Ratcheting die inkrementelle Verschiebung bestimmt.
Zur Untersuchung des Einflusses der Systemdynamik auf die Gleitreibung dient die sogenannte Mikro-Laufmaschine. Diese besteht aus einem starren Körper mit einer Anzahl von elastischen Kontaktstellen, der von einem konstant bewegten Fußpunkt gezogen wird. Neben einem Versuchsstand werden zur Analyse numerische Integration und umfangreichen Parameterstudien verwendet. Die Ergebnisse zeigen, dass der Reibungswiderstand fast verschwindet, wenn ein bestimmter Parameterbereich eingestellt wird. Es treten selbsterregte Schwingungen auf, die zu einem charakteristischen dynamischen Modus führen. Die Bewegung ist durch eine starke Korrelation zwischen niedrigen oder verschwindenden Normalkräften und einer schnellen Vorwärts-Bewegung gekennzeichnet. Dieses sogenannte *Micro-Walking* führt zu einer theoretischen maximalen Reduzierung des Reibungswiderstandes von bis zu 98 %. Dies konnte experimentell bestätigt werden, wobei die maximale Reduktion im Experiment bei 73 % lag.
Nach der Analyse und der Identifizierung der relevanten Parameterbereiche für alle drei Effekte wird ihr Vorkommen in technischen Systemen diskutiert. Darüber hinaus werden Leitlinien für mögliche technische Anwendungen gegeben.

Contents

List of Figures

List of Tables

Nomenclature

Parameters with Latin Letters

symbol	unit	parameter
a	m	contact radius
a_i	-	factor value i in DoE method
A_s	m^2	cross sectional area of spring rod
$\mathcal{A}_c$	m^2	contact area
$\mathcal{A}_{slip}$	m^2	slip area
b	m	slip radius
b_i	-	factor value i in DoE method
c	m	stick radius
c_s	$\mathrm{m\,s}^{-1}$	speed of sound
c_{sd}	m	stick radius after shakedown
d	m	indentation depth
D	m	contact disc diameter of micro-walking machine
D_b	m	bulk body diameter of micro-walking machine
D_c	m	contact length
E	$\mathrm{N\,m}^{-2}$	Young's modulus
E^*	$\mathrm{N\,m}^{-2}$	effective Young's modulus
$f\left(x_i, \alpha_j\right)$	1	model function for least square method
f_M	1	friction parameter in the model of Martins et al.
f_s	1	normalized spring force of base spring
f_{samp}	Hz	sampling frequency of micro-walking machine test rig
f_T	1	normalized tangential force
$f_{T,lim}$	1	normalized maximal force
f_x	N	tangential spring force of elastic foundation
f_z	N	normal spring force of elastic foundation
$\bar{f}_s$	1	mean of normalized spring force of base spring
$\tilde{f}_s$	1	normalized spring force of base spring
$\tilde{f}_x$	N	test tangential spring force of elastic foundation
f_0	Hz	excitation frequency of rolling body test rig
f_1	Hz	first eigenfrequency of rolling body test rig
F_{bZ}	N	elastic force of beam model of the spring
F_{cZ}	N	contact force of beam model of the spring
F_N	N	normal force
$F_{N1/2}$	N	normal force of contact springs
F_R	N	resistance force
F_s	N	spring force of base spring
F_T	N	tangential force

symbol	unit	parameter
$F_{T,max}$	N	maximum holding force
$F_{T1/2}$	N	tangential force of contact springs
F_W	N	resistance force of cross roller table
$\bar{F}_{Ni}$	N	average mean normal force
g	$\mathrm{m\,s^{-2}}$	gravitational acceleration
$g\,(x)$	m	equivalent profile function
G	-	function for determination of measurement uncertainty
G	$\mathrm{N\,m^{-2}}$	shear modulus
G^*	$\mathrm{N\,m^{-2}}$	effective shear modulus
G'	$\mathrm{N\,m^{-2}}$	storage modulus of standard rubber model
G''	$\mathrm{N\,m^{-2}}$	loss modulus of standard rubber model
h	m	lever arm of base spring
$h\,(r)$	m	profile function
h_M	1	ratio of height and width in the model of Martins et al.
$h_k\,(x)$	m	actual profile function
$h_0\,(x)$	m	initial profile function
Δh	m	height difference between bearing and contact point
I_s	$\mathrm{m^4}$	geometrical moment of inertia
k	m	constant of proportionality
k_s	$\mathrm{N\,m^{-1}}$	spring stiffness of base spring
k_x	$\mathrm{N\,m^{-1}}$	tangential spring stiffness of contact spots
k_z	$\mathrm{N\,m^{-1}}$	normal spring stiffness of contact spots
$\tilde{k}_s$	$\mathrm{N\,m^{-1}}$	effective spring stiffness of base spring
Δk_x	$\mathrm{N\,m^{-1}}$	tangential spring stiffness of elastic foundation
Δk_z	$\mathrm{N\,m^{-1}}$	normal spring stiffness of elastic foundation
l_s	m	length of spring rod of micro-walking machine
l_1	m	length of centre part of micro-walking machine
l_2	m	length of side disc of micro-walking machine
$\mathcal{L}_c$	m	contact width
m	kg	mass of the micro-walking machine
m_T	kg	mass of weight pot and weight
$M_{b\Phi}$	N m	elastic moment of beam model of the spring
$M_{c\Phi}$	N m	moment of contact of beam model of the spring
$p\,(x)$	$\mathrm{N\,m^{-2}}$	pressure distribution
p_0	$\mathrm{N\,m^{-2}}$	maximal pressure
p_{01-12}	1	coefficients of polynomial fit function
p_0'	$\mathrm{N\,m^{-2}}$	reduced pressure at boundary of cylindrical contact
r	m	coordinate in polar-coordinate system
r	1	Bravais-Pearson correlation coefficient
r_s	m	radius of cross sectional area of spring rod
r_0	m	constant radius in 2-D displacement function

symbol	unit	parameter
R	m	radius of sphere and cylinder
R_c	m	radius of contact disc of micro-walking machine
R_{1D}	m	radius of stretched 1-D profile
s	m	coordinate of spring position in MDR model
s_M	1	stiffness parameter in the model of Martins et al.
$s_{1/2}$	1	normalized motion of contact spots
$s'_{1/2}$	1	normalized velocity of contact spots
S_j	-	sum of squared deviations for set j of model parameters
S_s	1	frequency spectrum of normalized spring force
t	1	dimensionless time
t	1	correction term of student-t distribution
t_{dim}	s	dimensional time
t_{is}	1	relative stick time of instability
$t_{s1/2}$	1	relative stick time of contact spots
t_0	1	point in time after the transient process
t^*	1	shifted time
$\bar{t}$	1	conditioned and normalized time
T	s, 1	time of observation
T_c	s	characteristic time of loading
$T_{s1/2}$	s	stick time of contact spots
u	1	normalized displacement
$u_{n1/2}$	1	normalized normal deflection of contact springs
u_{lim}	1	normalized maximal rigid body displacement
$u_{n1/2}$	1	normalized tangential deflection of contact springs
u_{sd}	1	normalized shakedown displacement
u_{stat}	1	normalized static displacement
$u_x(x)$	1	normalized tangential displacement of particles
$u_{x1/2}$	1	normalized tangential deflection of contact springs
$u_{z1/2}$	1	normalized normal deflection of contact springs
$\bar{u}$	1	conditioned and normalized displacement
$\tilde{u}_{x1/2}$	1	normalized test tangential deflection of contact springs
$\tilde{u}_{s1/2}$	1	normalized test tangential deflection of contact springs
$\tilde{u}_{z1/2}$	1	normalized test normal deflection of contact springs
$\bar{u}_{z1/2}$	1	normalized normal deflection of contact springs
Δu	1	normalized incremental displacement
U	m	relative displacement of particles
U_{max}	m	maximal static displacement of spherical contact
U_0	m	maximal static displacement of cylindrical contact
U_{rt}	m	ratcheting displacement
U_{sd}	m	shakedown displacement
U_{stat}	m	static stick region displacement

symbol	unit	parameter
U_x	m	tangential displacement of particles
$U_x(x)$	m	tangential displacement of springs of elastic foundation
$U_{x1/2}$	m	tangential deflection of contact springs
$\tilde{U}_x(x)$	m	test tangential displacement of springs of elastic foundation
U_z	m	vertical displacement of particles
$U_z(x)$	m	vertical displacement of springs of elastic foundation
$U_{z1/2}$	m	normal deflection of contact springs
ΔU	m	incremental displacement
ΔU_s	m	rigid body shift per time step
$\Delta \bar{U}$	m	displacement caused by height difference
$\dot{U}$	$\mathrm{m\,s^{-1}}$	slip velocity of particles
v	$\mathrm{m\,s^{-1}}$	velocity
$var(f_s)$	$\mathrm{m\,s^{-1}}$	revolving variance of spring force
v_0	$\mathrm{m\,s^{-1}}$	velocity of base point of micro-walking machine
Δv	$\mathrm{m\,s^{-1}}$	limiting velocity in μ-function
Δv_1	$\mathrm{m\,s^{-1}}$	velocity difference of MDR model of rolling contact
w	1	normalized rolling amplitude
w_{lim}	1	normalized maximal rolling amplitude
W	m	rolling amplitude
W_{fric}	N m	frictional dissipation per time step
W_0	N m	frictional dissipation per cycle of tangential loading
ΔW	m	incremental increase of rolling amplitude
x	m	coordinate in Cartesian coordinate system
x	1	normalized lateral coordinate of translational motion
x_i	-	specific value of a measurement i
x_s	1	normalized lateral coordinate of base point
x'	1	normalized lateral velocity of micro-walking machine
x'_s	1	normalized lateral velocity of base point
x''	1	normalized lateral acceleration of translational motion
$\bar{x}$	-	arithmetic mean value of measurements
Δx	m	grid-size of MDR and CONTACT models
$\Delta \bar{x}$	1	normalized difference of lateral coordinate of translational motion
$\Delta \tilde{x}$	1	normalized difference of lateral coordinate of translational motion
X	m	lateral coordinate of translational motion
$\ddot{X}$	$\mathrm{m\,s^{-2}}$	lateral acceleration of translational motion
y	m	coordinate in Cartesian coordinate system
y_i	-	specific value of a measurement variable i
$\bar{y}$	-	arithmetic mean value of measurements
$\hat{y}_i$	-	fit value of a measurement variable i
δy_i	-	residual of a measurement variable i
Δy	m	grid-size of CONTACT models

symbol	unit	parameter
z	m	coordinate in Cartesian coordinate system
z	1	normalized vertical coordinate of translational motion
z_{stat}	1	normalized static vertical displacement
z''	1	normalized vertical acceleration of translational motion
$\tilde{z}$	1	normalized vertical coordinate of translational motion
Z	m	vertical coordinate of translational motion
$\ddot{Z}$	$\mathrm{m\,s^{-2}}$	vertical acceleration of translational motion
$2a$	m	height of micro-walking machine
$2b$	m	width of micro-walking machine
$2t_D$	s	size of Dirichlet window for revolving variance

Parameters with Greek Letters

symbol	unit	parameter
α_j	-	set j of model parameters
β	1	Dundurs' constant
γ	$\mathrm{s\,m^{-1}}$	steepness parameter in μ-function
ε	1	relative accuracy of output variables
ε_{xx}	1	tangential strain
ζ	m	moving coordinate
η	m	coordinate in Cartesian coordinate system
η	Pa s	viscosity of standard rubber model
η	1	constant of proportionality of incremental displacement
η_{exp}	1	constant of proportionality-experiment
η_{fit}	1	constant of proportionality-fit
η_{MDR}	1	constant of proportionality-MDR
Θ	$\mathrm{kg\,m^2}$	rotational inertia of micro-walking machine
κ	1	mapping parameter
κ_{1-8}	1	non-dimensional parameters of micro-walking machine
μ	1	coefficient of friction
μ_c	1	critical coefficient of friction
μ_e	1	effective coefficient of friction
μ_k	1	kinematic coefficient of friction
μ_s	1	static coefficient of friction
ν	1	Poisson's ratio
ξ	m	coordinate in Cartesian coordinate system
ξ_x	1	creep ratio of 3-D rolling contact
ξ_1	1	creep ratio of 1-D rolling contact

symbol	unit	parameter
$\sigma_{\bar{x}}$	-	standard deviation of the mean value
$\sigma_{\bar{y}}$	-	standard deviation of the mean value
τ	s	characteristic period of micro-walking machine
$\tau\,(x)$	$\mathrm{N\,m^{-2}}$	traction distribution
τ_{max}	$\mathrm{N\,m^{-2}}$	traction bound
τ_r	s	relaxation time
τ_R	$\mathrm{N\,m^{-2}}$	resistance traction
$\tau_1\,(x)$	$\mathrm{N\,m^{-2}}$	static traction distribution
$\tau_{1-sd}\,(x)$	$\mathrm{N\,m^{-2}}$	shakedown traction distribution
$\tau_2\,(x)$	$\mathrm{N\,m^{-2}}$	additional static traction distribution
$\tau_{2-sd}\,(x)$	$\mathrm{N\,m^{-2}}$	shakedown traction distribution
τ_2	$\mathrm{N\,m^{-2}}$	correctional traction term
τ_{21}	$\mathrm{N\,m^{-2}}$	correctional shakedown traction term
τ_{22}	$\mathrm{N\,m^{-2}}$	correctional shakedown traction term
φ	1	normalized rigid body rotation angle
φ''	1	normalized angular acceleration of rigid body
$\tilde{\varphi}$	1	normalized rigid body rotation angle
Φ	1	rotation angle of rigid body
$\ddot{\Phi}$	$1/\mathrm{s^2}$	angular acceleration of rigid body
ω	1/s	angular velocity of rolling sphere
ω_{sim}	1	normalized characteristic frequency of simulation
Ω_{exp}	1/s	characteristic frequency of experiment
Ω_{sim}	1/s	characteristic frequency of simulation

Chapter 1

Introduction

Frictional resistance is a crucial parameter in various technical, seismological and even biological systems. The core problem can be broken down to the frictional interaction of two bodies as depicted in Fig. 1.1 (a) that is often modelled using the so called Coulomb's law of dry friction. This model goes back to the works of Amontons [1] and Coulomb [2] and gives a proportional relation between the normal load F_N and the tangential load F_T of the contact.

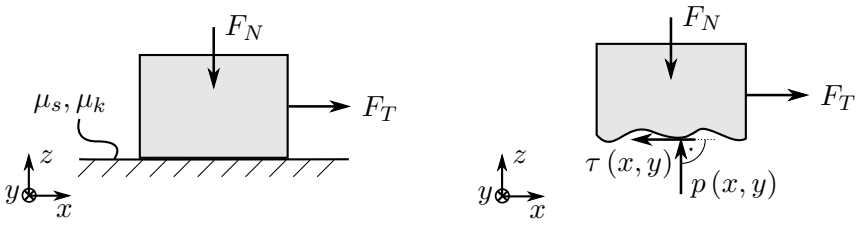

(a) macroscopic system (b) microscopic contacts

Fig. 1.1: frictional contact of two bodies loaded in the normal and tangential direction with F_N and F_T. (a) macroscopic system. (b) free body diagram with microscopic contacts

However, one distinguishes two cases. If F_T falls below the maximum holding force $F_{T,max}$ the system remains at rest:

$$F_T \leq F_{T,max} = \mu_s F_N \ . \tag{1.0.1}$$

This refers to the state of stick. Otherwise a relative movement of the two bodies occurs, where each of the two is subjected to the resistance force F_R which is caused by dissipative processes in the contact:

$$F_R = \mu_k F_N \ . \tag{1.0.2}$$

This refers to the state of slip, where the resistance force acts in the opposite direction of the slip direction. The two constants of proportionality denote the so called static (μ_s) and dynamic (μ_k) coefficient of friction. One explanation for the proportionality

of Coulomb's law lies in the contact properties of rough surfaces. According to the theory by Bowden and Tabor [3] rough surfaces consist of numerous small *hills* named asperities. Thus, the two bodies only touch in a few contact spots where, in case of dry metals, cold-weld junctions are formed. Assuming that the number of contact spots is proportional to the normal load, the coefficient of friction equals the ratio of the traction necessary to shear the cold-weld junctions and the penetration hardness. This explains also why experimentally, the static coefficient μ_s often exceeds the kinetic one μ_k since the metallic junctions become stronger after the surfaces have been in static contact for some time [4]. The coefficients are determined experimentally and are classified for a large number of combinations of contacting materials. This often leads to the widespread misconception of Coulomb's law of dry friction according to which the coefficients of friction are true constants that only depend on intrinsic properties of the materials in contact [5]. In fact they depend on small scale effects in the contact and are influenced by a various time and environmental conditions for both lubricated and dry contacts[1] [3]. In particular, the material combination, the contact geometry, chemical reactions, the temperature and the normal force itself all play an important role [5]. The static coefficient is also affected by the history of the contact, as evidenced by the fact that it increases with time [4, 7]. Furthermore, the kinetic coefficient is strongly affected by dynamic influences as sliding velocity [8] and vibrations [9]. This is a particular problem as it affects every measurement apparatus, i.e. tribometer, that is used for determination of the coefficients. On the one hand, this limits the value of tabulated coefficients as the influence of the tribometer used in the experiment remains vague. On the other hand, this is a possible explanation for difficulties on the reproducibility of measurement of coefficients that are determined with different tribometers under otherwise similar conditions [10].
In order to illustrate the basic underlying mechanism that is responsible for the influence of the systems motion, i.e. the system dynamics, one can consider a microscopic model of dry friction with only one constant coefficient μ. This coefficient is intended to reflect all microscopic influences on the surface that depend on the material pairing. Regardless whether the system consists of one single contact or numerous contact zones as in rough surfaces, the contact loads will occur as a stress distribution on the real contact area $\mathcal{A}_c$. One distinguishes the pressure $p(x, y)$, which is the stress that acts perpendicular to the tangent of the contact surface, and the traction $\tau(x, y)$, which acts parallel to the tangent, as shown in Fig. 1.1 (b). Thus, the microscopic equivalent to Coulomb's law states that a particle at the contact surface at position (x, y) is at rest as long as:

$$\tau(x, y) \leq \tau_{max} = \mu p(x, y) \ , \tag{1.0.3}$$

and starts to slip as soon as this so called traction bound, i.e. the local maximal tangential load, is exceeded. In this case, the particle is subjected to a resistance traction:

$$\tau_R(x, y) = \mu p(x, y) \ . \tag{1.0.4}$$

[1] It should be emphasized that Coulomb was already fully aware of these many influences and also presented a lot of experimental work on this subject as shown in the article of Popova and Popov [6].

For real static systems or stationary dynamic systems with constant relative velocity between the two contacting bodies, the microscopic criteria (1.0.3) and (1.0.4) would not imply any difference to the macroscopic criteria (1.0.1) and (1.0.2), except for the constant μ. However, the case is different if one considers a pressure distribution $p\,(x, y, t)$ that varies in time. The particles on the surface will start to slip whenever the traction bound (1.0.3) is exceeded. Assuming that adjacent contact zones are sufficiently far away from one another they could be regarded as being independent. This gives the possibility that some of them are in a state of stick (stick zones) while others are in a state of slip (slip zones). This applies even under the assumption that the macroscopic tangential force does not exceed the maximal tangential load at any time:

$$F_T\,(t) = \int_{\mathcal{A}_c} \tau\,(t)\mathrm{d}A < \mu F_N\,(t) \quad \forall t\,. \tag{1.0.5}$$

In case that slip occurs successively in *all* the contact zones it would consequently accumulate to a continued rigid body motion even if assumption (1.0.5) is never violated. For instance, one can consider an elastic substrate and a rigid block that is constantly loaded as in Fig. 1.2 (a). A slight oscillatory rotation will lead to a time varying pressure such that slip alternately occurs on one side while the other side sticks as shown in Fig. 1.2 (b). Thus within every period the system will move an incremental step ΔU to the right as shown in Fig. 1.2 (c). The micro-slip induces a rigid body motion. However, this scenario also requires that the slip is always directed in the same direction, otherwise no net rigid body motion would occur.

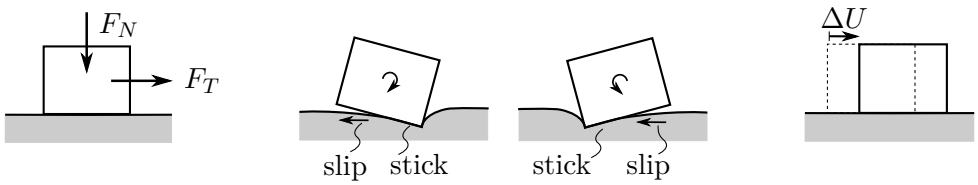

(a) rigid block (b) alternating slip (c) motion

Fig. 1.2: (a) constantly loaded rigid block on elastic substrate. (b) oscillatory rotation leads to varying slip and stick zones. (c) micro-slip causes rigid body motion ΔU

Considering mechanical systems with friction this introductory example raises several issues. Firstly, micro-slip can lead to failure of nominally static systems. By this, one means the effect that micro-slip can cause relative motion of technical components that should actually not move according to the macroscopic criterion (1.0.1). Secondly, micro-slip can explain the dynamic influence on the frictional resistance of systems with gross slip. This describes the effect that a macroscopic motion that appears as smooth sliding can in fact be superposed by microscopic vibrations in the contact zone. These vibrations might reduce the frictional resistance of the overall system such that it is actually lower than estimated considering the macroscopic criterion (1.0.2).

1.1 State of Scientific Research

In the following section some important works will be introduced that serve as the starting point for the following analysis. A more or less arbitrary classification into nominally static and dynamic systems is chosen, although such a strong distinction does not exist. Here, nominally static refers to systems in which no gross sliding and thus no relative motion of components is initially expected. Dynamic refers to the opposite, those systems in which gross sliding and relative motion is expected to occur.

1.1.1 Nominally Static Systems

Force locked connections are found in various technical systems. These nominally static frictional contacts[2] are crucial for the generation of solid detachable and non-detachable connections between technical components. Examples include bolted connections [11, 12], machining fixtures [13], interference fits [14] or dovetail connections on the hub of fan-blades [15]. The tangential load capacity of these systems is primarily determined by the macroscopic normal load F_N and the coefficient of friction μ. According to Coulomb's law of dry friction such a connection holds as long as the macroscopic tangential load F_T falls below the maximum holding force $F_{T,max}$ of equation (1.0.1). Due to vibrations, the macroscopic loads often either consist of a significant static part superposed by small oscillations, or the overall loads are constant and there occur only oscillations of the stress distribution. For example, in the dovetail connections of turbine blades the radial centrifugal force pulls the dovetail into the socket while there is a superimposed vibration in the plane of the fan. These scenarios can lead to a periodic incremental slip $U(x, y)$ of the particles in the interface, even if F_T is far below $F_{T,max}$, i.e. appears insufficient to cause complete sliding [16]. Possible consequences of this are micro-slip [17] and fretting fatigue [18, 19] of the relevant components.

Frictional Shakedown Churchmann and Hills [20] and Antoni et al. [21] showed that under certain conditions, it happens that the interface slip ceases after the first few oscillation periods. This is the case, if the initial displacement of particles generates a residual force in the interface, which is sufficiently strong to prevent any further slip. Subsequently, the entire contact will finally remain in a state of stick even if the oscillation is continued. Due to the strong analogy to the shakedown state in solid mechanics, in which the deformed bodies only show plastic strain in the first few loading cycles and pure elastic response afterwards [22], this effect is referred to as frictional shakedown [23]. Consequently, Klarbring et al. transferred the well-known Melan theorem for plastic shakedown [24] to both discrete [25] and continuous systems [26] with Coulomb friction and incomplete contact, i.e. systems in which the contact area does not change during the loading cycle. The shakedown theorem states that if there exists a safe shakedown displacement of particles in the interface $\tilde{U}(x, y)$ for which the whole system is in a state of stick, then the actual slip displacement $U(x, y)$ will monotonically reach

[2] This refers to connections that are intended to hold.

$\tilde{U}(x, y)$ for all $(x, y) \in \mathcal{A}_c$. Thus, a system that is subjected to an oscillating load, will shakedown and monotonically reach a safe shakedown displacement, i.e. an equilibrium state without any slip and dissipation, even if the oscillation is continued. One important requirement for this is an uncoupled system, meaning that tangential displacements in the interface do not influence the pressure and vice versa. However, in case of coupled two dimensional discrete systems, shakedown is also possible, if the friction coefficient in each node is less than a critical value, which depends on the coupling between adjacent nodes [25].

Ratcheting In case that the system exceeds the shakedown limits, i.e. the prerequisites for a safe shakedown to occur, the micro-slip continues and the system exhibits steady state slip. One possible scenario is that the micro-slip occurs in different contact areas for each loading cycle. In turn, the accumulation over all the cycles leads to a rigid body motion. This case is referred to as ratcheting due to the similarity to plasticity, where ratcheting specifies an accumulating deformation that usually leads to plastic collapse of the system [22, 23]. Antoni et al. stated that ratcheting can lead to significant global relative displacement between components and can account for the failure of some assembly parts in mechanical structures [21]. Mugadu et al. introduced a rigid flat punch loaded by a constant tangential force insufficient to cause gross sliding [27]. A constant normal force that moves backwards and forwards on the punch causes micro-slip that alternately migrates in from one side of the contact. This induces a rocking motion of the punch such that it walks across an elastic half plane by a constant increment in each loading cycle, even though the global friction limit is not exceeded at any time. Nowell used numerical methods to also study the case for a normal force being strong enough to completely lift the punch from the ends [28]. Ciavarella extended the model taking into account dissimilar materials and showed that dissimilarity decreases the load needed for ratcheting to occur and increases the slip per cycle [29].

Cyclic Slip In addition, it is possible, that a mechanical system with friction exhibits reversing slip with no net rigid body displacement. This case is referred to as cyclic slip in accordance to the cyclic plasticity case [23]. Ciavarella showed that for the walking punch model cyclic slip only occurs for dissimilar materials, as for similar materials, a constant tangential load leads to a constant direction of slip [29].

1.1.2 Dynamic Systems

Many systems also exhibit sliding friction [30]. This describes the situation when two contacting bodies move relatively to each other. Examples include brakes [31], clutches [32], machine tool slide-ways [33], joints in technical [34] and biological systems [35] and even seismological systems as tectonic plates [36]. Generally spoken, sliding friction occurs whenever F_T exceeds the maximum holding force. The system is then subjected to the resistance force F_R as in equation (1.0.2) that is caused by dissipative processes in the contact. Despite the fact that the kinetic coefficient of friction μ_k can be measured

with little difficulty under laboratory conditions, there exist severe dynamic influences. Firstly, this makes it very difficult to predict the coefficients a priori from first principles. Secondly, this limits the value of tabulated coefficients as the influence of the tribometer used in the experiment remains unclear [5, 37].

System Dynamics Dynamic influences on the frictional resistance include for instance damping, self-excited and externally excited vibrations, the velocity, the contact stiffness and the interaction between the structural dynamic behaviour and the excitation by the frictional force [5]. In particular the impact of system dynamics on the interface response of frictional contacts is a crucial factor. This is mainly caused by a coupling between the in-plane and out of plane vibrations in sliding systems [38]. An important work is the experiment of Tolstoi, who studied the interaction of the tangential and normal degree of freedom [39]. He found that tangential slip events are accompanied by an upward movement of the contacting body and that damping increases the frictional resistance. In addition, he used piezo actuators to induce externally excited vibrations in the normal direction. Through resonance effects, the frictional resistance was reduced between 35 % and 85 %. Godfrey used electrical resistance measurements and showed that this effect is due to a reduction of the metal-to-metal contact zone induced by decreasing loads. The reduction in the coefficient of friction was therefore characterized as apparent [40]. Polycarpou and Soom used linear dynamic models to compute the normal motion of a lubricated sliding system. They concluded that the instantaneous normal separation significantly affects the friction force. A good representation of the dynamics of the sliding system in the normal direction is therefore very important [41, 42, 43]. Several authors added a rotational degree of freedom. By this, they considered that the kinematic coupling between normal, tangential and rotational motion leads to varying forces and moments what in turn influences the friction [10, 44, 45]. Twozydlo et al. modelled a typical pin-on-disk apparatus consisting of rigid bodies with elastic connections. They showed that coupling between rotational and normal modes induces self-excited oscillations. In combination with high-frequency stick-slip motion, these oscillations reduce the apparent kinetic coefficient of friction. A particular pin-on-disk experimental set-up gave good qualitative and quantitative correlation with numerical results [46]. Adams examined a beam that is in frictional contact with an elastic foundation [47]. In this model the interplay of the friction force and moments at the interface and the bending of the beam leads to instabilities that increase with increasing coefficient of friction. This self-excited oscillation leads to a partial loss of contact and a stick-slip motion.

Slip Waves Despite discrete lumped parameter models, many authors considered interface waves with separation between contacting half-spaces. Caminou and Dundurs investigated the so-called *carpet-fold* motion, which gives the possibility of a sliding motion between two identical bodies without interface slipping [48], i.e. without frictional resistance. Adams examined elastic half-spaces in dry contact and concluded that the deformation along the interface and slip wave propagation is a potential destabilizing mechanism for steady sliding [49]. Although his model uses a constant coefficient of

friction without distinction between the static and kinetic case, he demonstrated that interface slip waves may be responsible for the apparent velocity-dependence of friction coefficient measurements [50]. The apparent coefficient of friction can decrease with increasing sliding speed due to the carpet-fold motion.

1.2 Objective

On basis of the studies described above, theoretical models and experiments are to be developed in order to examine the influence of micro-slip on the macroscopic behaviour of mechanical systems with friction. As sketched in Fig. 1.3 system dynamics and micro-slip affects nominally static systems as well as dynamic systems.

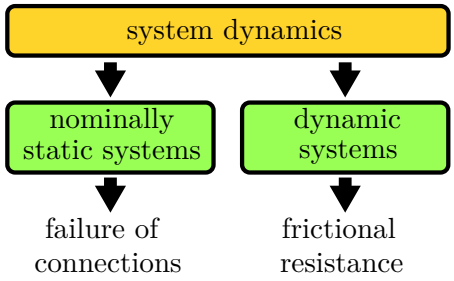

Fig. 1.3: sketch of the influence of system dynamics on systems with friction

Starting from the distinction introduced in section 1.1 the objective of this work is structured as follows.

Shakedown and Ratcheting Shakedown characterizes the effect that oscillatory frictional slip causes a state of residual stress that inhibits or reduces the slip in subsequent cycles. It is worthwhile to predict under which conditions a system responses like this because shakedown is one way to prevent for instance fretting or failure of force locked connections. So far the theory of frictional shakedown was examined only for complete contacts but much less is known for the case where the contact area changes with time [29]. In addition, many studies are based on numerical simulations and the results are often difficult to interpret and cannot easily been transferred to slightly modified systems [28]. Thus, the objective is to introduce a frictional system with an incomplete contact and to study the different scenarios that occur if this system is subjected to oscillating loads. More specifically the first objectives for this work are as follows:

- Development of generic models for incomplete contacts
- Analysis of the shakedown process and the final shakedown state
- Derivation of the shakedown limits, i.e. failure criteria
- Examination of the ratcheting phenomenon in incomplete contacts

Dynamic Influences on Sliding Friction Vibrations in the normal direction decrease the frictional resistance of mechanical systems. This effect has been known for long and is also applied in technical systems [39, 51]. Furthermore friction and certain dynamic coupling effects can lead to instabilities [49, 50]. This raises the question to what extent these self-excited vibrations can lead to a self-excited reduction of the macroscopic frictional resistance. In case that the corresponding amplitudes are of a microscopic character, they could be superimposed to an apparently smooth sliding motion of the system while being undetected. Hence, it is one aim of this work to develop a model that exhibits this kind of behaviour. More specifically, the further objectives are as follows:

- Introduction of a model that captures dynamic influences on sliding friction
- Investigation of the post-instability behaviour and analysis of the parameters
- Analysis of the underlying basic mechanisms for the reduction

In order to achieve these aims, classical contact mechanics, the well-known Method of Dimensionality Reduction, several numerical simulation tools and experiments are being used. The final goal is not only to gain a deeper understanding of the effects of shakedown, ratcheting and walking, but also to give guidelines for the construction of real technical systems. Examples range from force-locked connections to mechanical drives and to tribometers.

1.3 Structure

Methods and theories that are important for the further analysis are introduced in chapter 2. In addition to a short description of important contact systems, the Method of Dimensionality Reduction is described and different aspects of the modelling of dry friction are discussed. This gives the fundamentals for the next steps of the analysis. Firstly, chapter 3 focuses on shakedown and ratcheting in incomplete contacts. Several models are introduced and analysed and the shakedown limits are derived. Secondly, in chapter 4, the phenomenon of self-induced oscillations and the resulting reduction of sliding friction is discussed. Both topics are followed by an experimental investigation. The experimental rigs that are used in the analysis and the experimental procedures are introduced in chapter 5. Finally a conclusion and an outlook are given in chapter 6. In the appendix, for reasons of reproducibility, methods and theories are described that are used in this work but do not contribute substantially to the results.

Chapter 2

Fundamentals and Methods

In general, mechanical systems with friction are influenced by a complex interaction of different phenomena:

Rigid Body Motion The relative motion of the contacting bodies influences the stresses in the contact. The motion has its origin in the forces and moments acting on the bodies but is also influenced by inertia effects.

Contact Mechanics The stresses in the contact lead to deformation of the materials of the contacting bodies and thus change the contact area. This deformation depends on the geometry of the bodies as well as their material behaviour.

Friction The distribution of stick and slip in the contact area is a result of the contact stresses. However, this in turn affects the forces acting on the bodies.

These many cross influences complicate the understanding and the analysis of the interplay of system dynamics and friction. In the following section, the basic tools and models used in this work are introduced. In addition to a brief summary of important contact systems, the Method of Dimensionality Reduction (MDR) is introduced. Furthermore, some important aspects in the modelling of frictional systems are discussed. This enables an accurate and efficient modelling of mechanical systems with friction under consideration of dynamic influences.

2.1 Contact Mechanics

In case that the contact area and the slope of the geometry of the bodies, respectively their deformation, are small in comparison to the size of the contacting bodies, they may be represented by half-spaces [52]. This assumption describes a semi-infinite body whose only boundary is an infinite plane what greatly simplifies the calculation of elastic contact problems. In general, one distinguishes two qualitatively different kind of contacts,

depending on the geometry of the contacting bodies [52]. The first kind is characterized as complete and occurs whenever the contact area is independent of the force. As an example, one can consider a flat-ended punch which is pressed into an elastic half-space, as shown in Fig. 2.1 (a). This often leads to difficulties in the analysis of systems where both bodies are elastic, because the contact pressure will be singular at the edges of the contact and the punch cannot be modelled as a semi-infinite body. Therefore, solutions of incomplete contacts mostly assume a rigid punch. The second kind of contacts is characterized as incomplete and occurs when the contact area changes with the loading. These systems are found when two convex bodies come into contact as shown in Fig. 2.1 (b). In this case, the two bodies initially only touch in one point. As the applied load increases, the contact area increases as well. In contrast to the former case, the contact pressure falls continuously to zero at the edges for incomplete contacts.

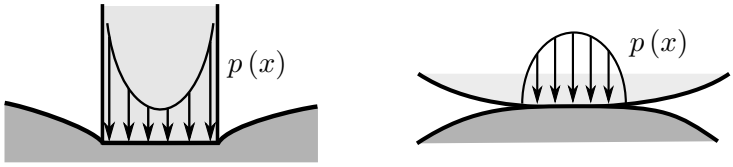

(a) complete contact (b) incomplete contact

Fig. 2.1: (a) complete contact: contact area is independent from loading. (b) incomplete contact: contact area changes during loading [52]

Moreover, the contact can be assumed as decoupled if the so-called Dundurs' constant β is equal to zero [53]. For plane strain β is given as:

$$\beta = \frac{1}{2} \frac{\frac{1}{G_1}(1-2\nu_1) - \frac{1}{G_2}(1-2\nu_2)}{\frac{1}{G_1}(1-\nu_1) + \frac{1}{G_2}(1-\nu_2)} , \tag{2.1.1}$$

where G_i and ν_i are the shear modulus respectively Poisson's ratio for the two contacting bodies. The uncoupling condition is satisfied for the following cases [54]:

1. both bodies consist of the same material
2. both bodies are incompressible, $\nu_1 = \nu_2 = 0.5$
3. one body is incompressible and the other body is rigid
4. the contact is frictionless, $\mu = 0$

This condition is also referred to as elastically similar and indicates that the integrals describing the normal and tangential loading are uncoupled [52]. As a consequence, variations in the normal force will not induce any tangential displacement and vice versa. Hence, the normal and tangential direction can be analysed separately and their superposition then gives the overall solution. In addition, the initial contact problem

of two elastic bodies can be transferred to the indentation of an elastic half-space by a rigid punch, where the effective, elastic modules are defined as [55]:

$$E^* = \left(\frac{1-\nu_1}{2G_1} + \frac{1-\nu_2}{2G_2} \right)^{-1} \quad \text{and} \quad G^* = \left(\frac{2-\nu_1}{4G_1} + \frac{2-\nu_2}{4G_2} \right)^{-1} . \tag{2.1.2}$$

Throughout this work, only contacts that are uncoupled and fulfil the half-space assumption are considered. Consequently, all systems introduced will be from the latter type, i.e. indentation of an elastic half-space by a rigid punch. In the following, a few results and methods of classical contact mechanics that are important for the further analysis are summarized. Please refer to the well-known books of Popov [55] or Johnson [56] for a detailed representation of the derivations.

2.1.1 Spherical Normal Contact

Consider the classical Hertzian contact [57] of an elastic half-space and a rigid sphere, which is loaded in the z-direction with the normal force F_N as shown in Fig. 2.2 (a). The radius of the sphere R is chosen as an effective radius of a contact consisting of two elastic spheres with particular radii R_i [55]:

$$R = \left(\frac{1}{R_1} + \frac{1}{R_2} \right)^{-1} . \tag{2.1.3}$$

Instead of solving this initial contact problem, where neither the stress distribution nor the area of contact are known initially, one usually considers the deformation of the half-space by a given stress distribution. In the classic works of contact mechanics these direct solutions are then used as bricks for the solution of the initial contact problem [55].

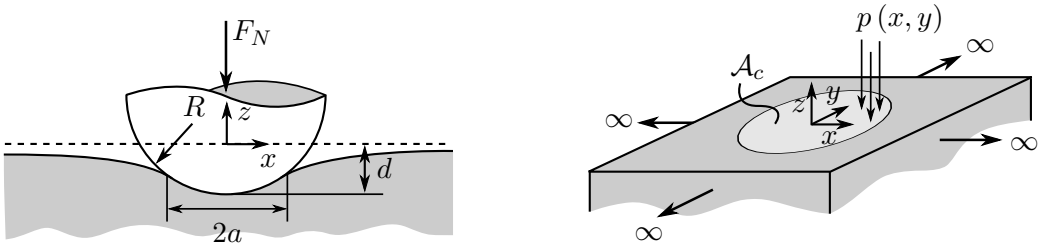

(a) contact problem (b) direct problem

Fig. 2.2: (a) contact problem: indentation of an elastic half-space by a rigid sphere. (b) direct problem: elastic half-space loaded by a pressure distribution

Sphere and half-space will only touch within a circular area $\mathcal{A}_c$ with radius a in the centre of the contact. This contact area is loaded with the pressure $p\,(x,y)$ that leads to a vertical displacement of the particles U_z on the surface ($z = 0$). It is maximal in the centre ($x = 0, y = 0, z = 0$), where U_z matches the indentation depth d that is defined as the vertical shift of the sphere. Pressure and normal displacement in the contact

area are related through the following integral equation, that is given by the potential functions of Boussinesq and Cerruti [56, 58]:

$$U_z(x,y) = \frac{1}{\pi E^*} \iint_{\mathcal{A}_c} \frac{p(\xi,\eta)}{s} \mathrm{d}\xi \mathrm{d}\eta \quad \text{for} \quad x,y \in \mathcal{A}_c \,, \tag{2.1.4}$$

where:

$$s = \sqrt{(\xi - x)^2 + (\eta - y)^2} \,. \tag{2.1.5}$$

In case of the rigid sphere, the displacement U_z of particles in the contact must match the difference of the indentation d and the initial separation $h(r)$, i.e. the profile of the sphere. Using the parabolic approximation[1] for $R \gg d$ [55] this yields:

$$U_z(r) = d - h(r) = d - \frac{r^2}{2R} \,, \tag{2.1.6}$$

where $r = \sqrt{x^2 + y^2}$. The following pressure is given by the Hertz theory of the frictionless contact between two bodies of revolution [57]:

$$p(r) = p_0 \left(1 - \left(\frac{r}{a}\right)^2\right)^{1/2} \,. \tag{2.1.7}$$

This pressure fulfils the integral of equation (2.1.4) with U_z as in (2.1.6). Here the maximal pressure p_0 and the contact radius a are given as:

$$p_0 = \frac{2}{\pi} E^* \left(\frac{d}{R}\right)^{1/2} \,,\; a = \sqrt{Rd} \,. \tag{2.1.8}$$

Finally, the relation between normal force and indentation yields:

$$F_N = \frac{4}{3} E^* R^{1/2} d^{3/2} \,. \tag{2.1.9}$$

2.1.2 Spherical Tangential Contact

As a consequence of the decoupling assumption, the tangential contact can simply be modelled as a superposition of the normal contact by a tangential loading F_T in the x-direction. Coulomb type of friction with finite constant coefficient μ between the two surfaces is assumed. The tangential load is compensated by an initially unknown frictional shearing traction $\tau(x,y)$ on the surface of the half-space. In case that F_T is insufficient to cause gross sliding, i.e. $F_T < \mu F_N$, the contact area will be divided into a stick region delimited by the stick radius c in the centre and an annular slip region on the edge, as shown in Fig. 2.3 (a). Inside the stick region, the surface displacement

[1] The exact profile is given as: $h(r) = R - \sqrt{R^2 - r^2}$.

of particles U_x in the direction of F_T must be constant, whereas in the slip region, the traction must match the traction bound:

$$\begin{aligned} \text{stick-region:} \quad & 0 \leq \sqrt{x^2+y^2} \leq c \quad \Rightarrow U_x(x,y) = \text{const.} \ , \\ \text{slip-region:} \quad & c < \sqrt{x^2+y^2} \leq a \quad \Rightarrow \tau(x,y) = \mu p(x,y) \ . \end{aligned} \tag{2.1.10}$$

The problem corresponds to finding the correct shearing traction distribution that causes this contact configuration [58]. As for the normal direction, traction and tangential displacement in the contact area are again related through an integral equation, that is given by the potential functions of Boussinesq and Cerruti [56, 58]:

$$U_x(x,y) = \frac{1}{2\pi G} \iint_{\mathcal{A}_c} \tau(x,y) \left(\frac{1-\nu}{s} + \nu \frac{(\xi - x)^2}{s^3} \right) \mathrm{d}\xi \mathrm{d}\eta \quad \text{for} \quad x, y \in \mathcal{A}_c \ . \tag{2.1.11}$$

Here s is defined as in equation (2.1.5) and G and ν are given as:

$$G = \left(\frac{1}{G_1} + \frac{1}{G_2} \right)^{-1}, \quad \nu = G \left(\frac{\nu_1}{G_1} + \frac{\nu_2}{G_2} \right) \ . \tag{2.1.12}$$

Cattaneo [59] and Mindlin [60] independently presented a method of solution for elliptic contacts for this configuration known as incipient sliding.

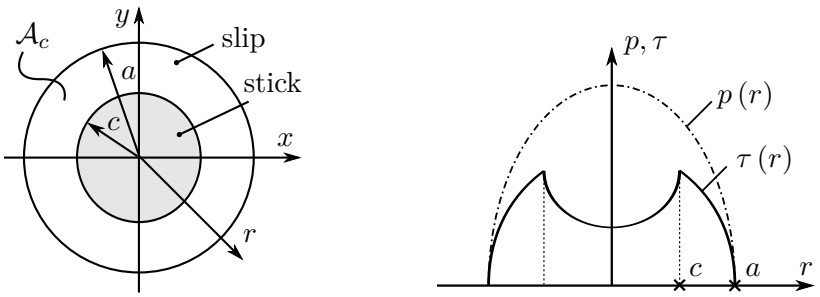

(a) contact regions (b) traction distribution

Fig. 2.3: (a) contact area with contact radius a and slip-radius c. (b) stress distribution in the contact area

A good description of their procedure is given in book of Popov [55]. The starting point is the case off full sliding, where the tangential traction must match the traction bound in the entire contact area:

$$\tau(r) = \mu p_0 \left(1 - \left(\frac{r}{a} \right)^2 \right)^{1/2} \quad \text{for} \quad 0 \leq r \leq a \ . \tag{2.1.13}$$

Now, to maintain sticking in case of incipient slip, the traction in the stick region must be a superposition of two elliptical distributions of the Hertzian type:

$$\tau(r) = \mu p_0 \left(1 - \left(\frac{r}{a} \right)^2 \right)^{1/2} - \tau_2 \left(1 - \left(\frac{r}{c} \right)^2 \right)^{1/2} \quad \text{for} \quad 0 \leq r \leq c \ . \tag{2.1.14}$$

These tractions cause a parabolic surface displacement in the stick region [55]:

$$U_x(x,y) = \mu p_0 \frac{\pi}{32Ga}\left(4(2-\nu)a^2 - (4-3\nu)x^2 - (4-\nu)y^2\right) \\ -\tau_2 \frac{\pi}{32Gc}\left(4(2-\nu)c^2 - (4-3\nu)x^2 - (4-\nu)y^2\right) \quad \text{for } 0 \le r \le c\,, \quad (2.1.15)$$

that must be constant in accordance to the no slip condition, i.e. $U_x = U_{stat} = \text{const.}$. Finally, this gives the correctional traction-term:

$$\tau_2 = \mu p_0 \frac{c}{a}\,. \quad (2.1.16)$$

The complete traction distribution is as shown in Fig. 2.3 (b). In addition, the stick radius c as well as the constant displacement in the stick region yield:

$$c = a\left(1 - \frac{F_T}{\mu F_N}\right)^{1/3}\,, \quad (2.1.17)$$

$$U_{stat} = U_x(x,y) = \mu \frac{E^*}{G^*} d\left(1 - \left(1 - \frac{F_T}{\mu F_N}\right)^{2/3}\right) \quad \text{for} \quad r \le c\,. \quad (2.1.18)$$

For axially symmetric, three-dimensional contacts the tangential problem can also be solved using the principle of Ciavarella [61, 58] and Jäger [62]. According to this, the tangential contact problem can be analysed as one of two normal contacts: the actual normal contact and an additional normal contact for a reduced load, that provides the correction of the tangential traction in the stick area.

2.1.3 Steady State Rolling Contact

Consider a rigid sphere with radius R that rolls on an elastic half-space with shear modulus G and Poisson's ratio ν. As depicted in Fig. 2.4 (a), the sphere rotates with an angular velocity ω while it moves to the right with the forward velocity v and is loaded with F_N and F_T. Between the surfaces applies dry friction of the Coulomb type with finite constant coefficient μ. The case $v = \omega R$ refers as *pure* rolling and can only be obtained for infinite friction $\mu \to \infty$ or vanishing tangential force[2]. In case of *tractive* rolling, i.e. $F_T \neq 0$, occurs a difference between the circumferential velocity and the forward velocity, whose relative ratio is defined as the creep ratio [55]:

$$\xi_x = \frac{v - \omega R}{v}\,. \quad (2.1.19)$$

For $\omega R > v$ the friction force on the sphere is pointing forward and the system corresponds to a driven wheel. Otherwise, the friction force is pointing backwards and the system corresponds to a braking wheel. Reynolds identified creep as the reason for rolling resistance and described that it is caused by both, elastic deformation of the contacting bodies and relative displacement of particles in the interface [63]. The creep tries to drag

[2] One also distinguishes between *free* and *tractive* rolling, i.e. $F_T = 0$ respectively $F_T \neq 0$.

the sphere surface particles over the substrate and can be seen as an average amount of slip. Considering one particle on the surface of the wheel, the contact configuration can be explained as follows. When entering the contact area at the leading edge, the particle is free of stress. As the sphere rolls forward, it sticks to a particle of the opposing surface and is strained by the overall motion difference between the two bodies. This leads to a shear stress, which increases until the traction bound is reached and the particle starts to slip. As for the tangential contact, the contact area is thus divided into a stick and a slip region, the only difference being that the stick area is shifted to the leading edge and the slip area is shifted to trailing edge. As the state of each surface particle varies over time, one considers the steady rolling state[3] and uses a coordinate system that moves along with the contact.

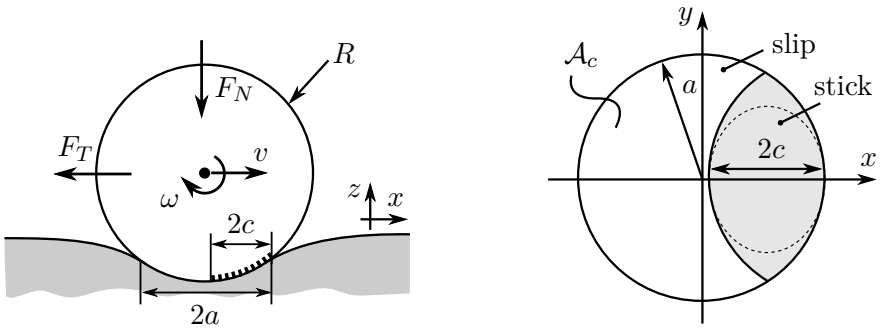

(a) tractive rolling of sphere (b) contact region

Fig. 2.4: (a) tractive rolling contact of rigid sphere and elastic half-space. The sphere moves with velocity v and rotates with angular velocity ω. (b) contact area with contact radius a and spindle-shaped stick region with half-width c

Hence, in the sticking region, the mass flow of substrate particles that move to the left with velocity v must match the mass flow of sphere particles that move to left with velocity ωR. This gives the relation between creep-ratio and strain as [55]:

$$\xi_x = \frac{\varepsilon_{xx}}{1+\varepsilon_{xx}} \approx \varepsilon_{xx} \ . \tag{2.1.20}$$

Again, the normal and tangential problem are decoupled, such that the contact radius $2a$ is directly given by the Hertzian theory. The stick region is a spindle- or lemon shaped area of width $2c$ as shown in Fig. 2.4 (b). One can assume it to be elliptically shaped[4] in order to give a closed form solution for the traction and creep [56]. In this case, the solution procedure resembles to the static problem as in section 2.1.2. Given the relation

[3]The transient starting process of the rolling is neglected.

[4]This is clearly an error, since the leading edge is located outside the stick region.

(2.1.20), the creep ratio[5] for the rolling sphere finally results to [64]:

$$\xi_x = -\frac{4-3\nu}{4\,(1-\nu)}\frac{\mu a}{R}\left(1-\left(1-\frac{F_T}{\mu F_N}\right)^{1/3}\right)\,, \tag{2.1.21}$$

and the half-width of the stick region yields:

$$c = a\left(1-\frac{F_T}{\mu F_N}\right)^{1/3}\,. \tag{2.1.22}$$

2.2 The Method of Dimensionality Reduction

Given the approaches introduced in the former sections, incomplete contacts can in principle be calculated using a stepwise equilibrium approach on basis of the actual pressure and traction distribution. However, there exist several serious difficulties. Often the exact distribution of pressure remains unknown [55]. Another problem is given by the different boundary conditions which have to be satisfied for the stick and slip zones when the configuration of these zones is not known in advance [56]. In addition, it often remains vague whether a closed form solution of the integrals can be found. Furthermore, numerical simulations, e.g. the boundary element method (BEM), are numerically very expensive as the corresponding stiffness matrix is dense.
The well-known Method of Dimensionality Reduction (MDR) offers a solution to these problems for a variety of applications. The MDR is based on the observation that close analogies exist between certain types of three-dimensional contact problems and one-dimensional contacts consisting of independent contact elements. The basic idea was firstly described in [65] and in the PhD thesis of Geike [66]. A more detailed description is given with the book of Popov and Heß[67]. The physical background of the MDR lies in the proportionality of the stiffness of a three-dimensional contact to the associated contact length instead of its contact area [68], what leads to certain mapping *rules*. Heßderived the exact mapping rules for axial symmetric bodies in various normal contact configurations including adhesion [69]. If these rules are fulfilled, the macroscopic properties of the new system coincide exactly with those of the initial system. Thus, the MDR is not an approximation but transfers the initial problem to an equivalent one. According to this, solving contact problems, either analytical or numerical, is trivialized [67]. There is a wide number of applications and further developments of the MDR ranging from rough surfaces [70, 71] to viscous media [72], fretting wear [73] and the modelling of stick-slip drives [74]. The MDR is exact for uncoupled ($\beta = 0$), rotational symmetric, three-dimensional normal and tangential contacts that satisfy the half-space assumption [67]. It consists essentially of two basic steps, as illustrated concisely in [75].

[5]This result is valid only in case that one of the contacting bodies is rigid. If both bodies are from the same material the creep ratio is doubled [56].

First Step of MDR In this, the three dimensional bodies in contact are replaced by an equivalent elastic or viscoelastic foundation and a rigid indenter. For an elastic contact, the correct equivalent foundation must consist of linear springs with normal stiffness Δk_z and tangential stiffness Δk_x as shown in Fig. 2.5 (a):

$$\Delta k_z = E^* \Delta x \quad \text{and} \quad \Delta k_x = G^* \Delta x \; . \tag{2.2.1}$$

Here Δx is the distance between adjacent springs, i.e. the grid-size. As the springs are independent from one another, in the equivalent model remains only one dimension.

(a) elastic half-space (b) one-dimensional system

Fig. 2.5: (a) initial three-dimensional system: elastic half-space. (b) equivalent one-dimensional system: elastic foundation with independent linear springs. First step of MDR

Second Step of MDR In this, the initial three dimensional profile $h\,(r)$ is transformed into a one-dimensional profile function $g\,(x)$ as shown in Fig. 2.6:

$$g\,(x) = |x| \int_0^{|x|} \frac{h'\,(r)}{\sqrt{x^2 - r^2}} \mathrm{d}r \; . \tag{2.2.2}$$

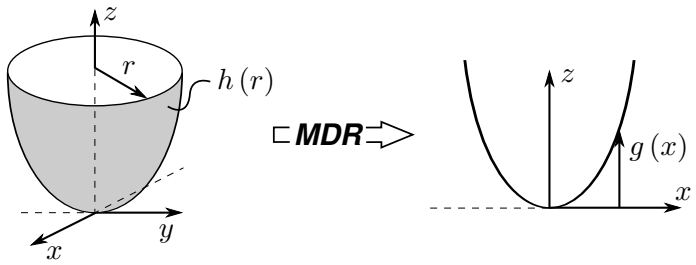

Fig. 2.6: transformation of the three-dimensional profile $h\,(r)$ into a one-dimensional equivalent profile $g\,(x)$. Second step of MDR

If these rules are fulfilled, the macroscopic properties of the one-dimensional system exactly match those of the initial three-dimensional system. However, special care must be taken not to violate the initial assumptions of the MDR. The following sections describe the application of the MDR to the tangential contact as well as the steady state rolling contact.

2.2.1 Spherical Tangential Contact using MDR

Consider a three-dimensional contact of a rigid sphere with radius R that is pressed into an elastic half-space by the normal force F_N and subsequently loaded in the tangential direction with F_T. Coulomb friction with constant μ is assumed. In the first step of the MDR, the elastic half-space is replaced by an equivalent system consisting of independent linear springs with normal stiffness Δk_z and tangential stiffness Δk_x as in equation (2.2.1). In the second step of the MDR the approximation of the initial three-dimensional profile of the sphere as in equation (2.1.6):

$$h\left(r\right) = \frac{r^2}{2R} \tag{2.2.3}$$

is mapped to a one-dimensional profile according to equation (2.2.2):

$$g\left(x\right) = |x| \int_0^{|x|} \frac{1}{R} \frac{r}{\sqrt{x^2 - r^2}} \mathrm{d}r \,, \tag{2.2.4}$$

$$g\left(x\right) = \frac{x^2}{R} \,. \tag{2.2.5}$$

This result can be interpreted as a stretch of the initial profile [76], where the new radius of the one-dimensional profile R_{1D} yields:

$$R_{1D} = \frac{1}{2} R \,. \tag{2.2.6}$$

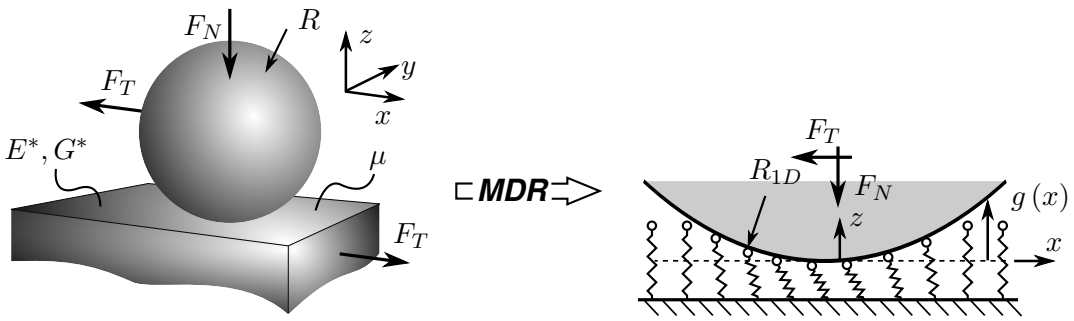

(a) three-dimensional contact (b) one-dimensional system

Fig. 2.7: (a) initial three-dimensional, tangentially loaded, elastic contact. (b) equivalent one-dimensional system consisting of an elastic foundation with stretched radius R_{1D}

Fig. 2.7 gives the initial three-dimensional system (a) and the equivalent one- dimensional model (b). The major advantage of the MDR is that the integral equations with mixed boundary conditions that arise in contact mechanics, are replaced by simple algebraic equations [67]. Instead of a pressure and traction distribution one only needs to know

the displacement of the springs in the normal and tangential direction U_z and U_x. The corresponding spring forces are then given by the relations:

$$f_z(x) = \Delta k_z U_z(x) \quad \text{and} \quad f_x(x) = \Delta k_x U_x(x) \ . \tag{2.2.7}$$

The missing displacements can be derived by kinematic considerations, as all springs are independent from one another. In case of the normal direction, the deflection U_z for all springs in contact is simply determined by the difference between the profile $g(x)$ and the indentation depth d:

$$U_z(x) = d - g(x) = d - \frac{x^2}{R} \ \text{ for } \ -a \leq x \leq a \ . \tag{2.2.8}$$

Given the condition that U_z must be zero at the contact edges $x = \pm a$ and equation (2.2.8) the missing contact radius yields:

$$U_z(|x| = a) = 0 = d - \frac{a^2}{R} \Rightarrow a = \sqrt{Rd} \ . \tag{2.2.9}$$

This corresponds exactly to the well-known result of the Hertzian contact [55], see (2.1.8). The macroscopic normal force F_N must match the overall normal force of the springs:

$$F_N = \int_{\mathcal{F}} \mathrm{d}F_z \ . \tag{2.2.10}$$

With the relation:

$$\mathrm{d}F_z = \lim_{\Delta x \to 0} \frac{\Delta k_z}{\Delta x} U_z \mathrm{d}x = E^* U_z \mathrm{d}x \tag{2.2.11}$$

and equation (2.2.8) this yields:

$$F_N = 2\int_0^a E^* U_z \mathrm{d}x = 2\int_0^a E^* \left(d - \frac{x^2}{R}\right) \mathrm{d}x \ , \tag{2.2.12}$$

$$F_N = \frac{4}{3} E^* R^{1/2} d^{3/2} \ , \tag{2.2.13}$$

what is again equivalent to the well-known Hertzian contact [55], see (2.1.9). The tangential displacement can be derived as follows. For F_T insufficient to cause complete sliding, i.e. $F_T < \mu F_N$, slipping will only occur at the boundary area of the contact. In this region, the forces of the springs equal the traction bound, what in connection with equations (2.2.7) and (2.2.8) gives:

$$f_x(x) = \mu f_z(x) \Rightarrow U_x(x) = \mu \frac{E^*}{G^*} \left(d - \frac{x^2}{R}\right) \ . \tag{2.2.14}$$

The centre region remains in a state of stick and is delimited by the stick radius c. Here, the tangential displacement is constant and matches the displacement between sphere and substrate U_{stat}. Taken together the tangential contact configuration reads:

$$\begin{aligned} \text{stick-region:} \quad & 0 \leq |x| \leq c \quad \Rightarrow U_x(x) = U_{stat} \ , \\ \text{slip-region:} \quad & c < |x| \leq a \quad \Rightarrow U_x(x) = \mu \tfrac{E^*}{G^*} \left(d - \tfrac{x^2}{R}\right) \ . \end{aligned} \tag{2.2.15}$$

The missing stick radius can be derived from the condition that the displacements must be continuous at the edge of the stick region $x = \pm c$. With equation (2.2.15) this yields:

$$U_{stat} = U_x\left(x = c\right) = \mu\frac{E^*}{G^*}\left(d - \frac{c^2}{R}\right) \Rightarrow c^2 = R\left(d - \frac{G^*}{E^*}\frac{U_{stat}}{\mu}\right) . \tag{2.2.16}$$

The macroscopic force F_T must match the overall normal force of the springs:

$$F_T = 2\int_0^c G^* U_{stat}\mathrm{d}x + 2\int_c^a \mu E^*\left(d - \frac{x^2}{R}\right)\mathrm{d}x . \tag{2.2.17}$$

Together with (2.2.16) this gives the static displacement as:

$$U_{stat} = \mu\frac{E^*}{G^*}d\left(1 - \left(1 - \frac{F_T}{\mu F_N}\right)^{2/3}\right) . \tag{2.2.18}$$

Finally, inserting (2.2.18) into (2.2.16) yields the stick radius as:

$$c = a\left(1 - \frac{F_T}{F_N}\right)^{1/3} . \tag{2.2.19}$$

Again, c and U_{stat} correspond to the well-known results of the three-dimensional system [55], see (2.1.17) and (2.1.18). This shows that tangentially loaded contacts of a rigid sphere and an elastic half-space can be mapped exactly to an equivalent one-dimensional system. This applies for tangential contacts of arbitrarily shaped bodies as well, as long as the assumptions of axial symmetry and decoupled displacements are not violated [67].

2.2.2 Steady-State Rolling Contact using MDR

In this section it is shown that three dimensional tractive rolling contacts can be mapped to a one-dimensional equivalent system as well. Starting point is the steady state rolling contact between an elastic half-space and a rigid sphere as introduced in section 2.1.3. The sphere is pressed into the half-space by the normal force F_N and is tangentially loaded with F_T. The sphere moves with velocity v in the x-direction and rotates with an angular velocity ω, as shown in Fig. 2.8 (a).

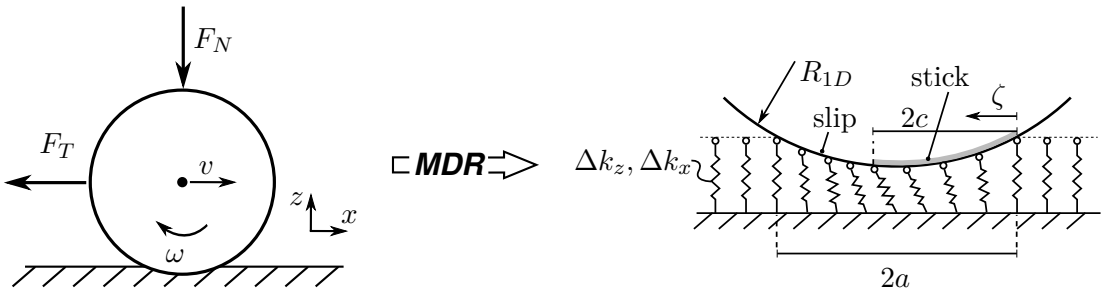

(a) rolling contact (b) equivalent system

Fig. 2.8: (a) steady state rolling contact between a sphere and an elastic half-space. (b) one-dimensional equivalent system with constantly moving coordinate ζ

Again, in the first step of MDR, the elastic half-space is replaced by an elastic foundation that consists of a number of similar independent springs with normal stiffness Δk_z and tangential stiffness Δk_x as in equation (2.2.1). Likewise, the radius of the MDR system R_{1D} is stretched as $R_{1D} = 1/2R$ according to second step of MDR (2.2.2). With this, the MDR system gives the exact relations between load, contact configuration and rigid body displacement for the normal contact, as shown in section 2.2.1 [67]. Thus, indentation depth d and contact radius a correspond exactly to the Hertzian contact and one only has to consider the uncoupled tangential problem.
As in the static case, the contact region is divided into a stick- and a slip-region. At the leading edge at the right side of the contact, the springs are initially completely relaxed. As soon as they touch the sphere they start to stick. The tangential force of an arbitrary spring f_x then increases with the further rolling due to the elastic displacement. Its normal force f_z initially increases as well until the lowest point of the sphere rolls past it. The normal force then decreases until finally f_x exceeds the friction bound $f_{T,max} = \mu f_z$ and the spring starts to slip. In consequence, the contact region is divided into a stick-region at the leading edge and a slip-region at the trailing edge, as shown in Fig. 2.8 (b). For further consideration, the co-moving coordinate ζ is chosen that has its origin exactly at the leading edge and moves with the sphere as shown in Fig. 2.8 (b). The tangential displacement $U_x(\zeta)$ of an arbitrary spring at position ζ then corresponds to the so far unknown path difference $\Delta v_1 t = (\omega R - v)\, t$ between the sphere and the substrate. With $\zeta = vt$ it follows:

$$U_x(\zeta) = \Delta v_1 t = \Delta v_1 \frac{\zeta}{vt} t = \frac{\Delta v_1}{v} \zeta \,, \tag{2.2.20}$$

what gives the tangential force for the springs in the stick region $0 \leq \zeta \leq 2c$:

$$f_x(\zeta) = \Delta k_x U_x(\zeta) = \Delta k_x \frac{\Delta v_1}{v} \zeta \,. \tag{2.2.21}$$

In the rest of the contact region $2c \leq \zeta \leq 2a$, the springs are slipping:

$$f_x(\zeta) = \mu f_z(\zeta) = \mu \Delta k_z U_z(\zeta) \,. \tag{2.2.22}$$

The missing normal displacement $U_z(\zeta)$ is given by the indentation of the rigid sphere into the elastic foundation of independent springs. With the indentation depth d and the approximation of the profile of the sphere for $R \gg d$ as in in equation (2.1.6) follows:

$$U_z(\zeta) = d - \frac{(a-\zeta)^2}{2R_1} = \frac{2a\zeta - \zeta^2}{R} \,. \tag{2.2.23}$$

The unknown stick-radius is given by the stick condition at $\zeta = 2c$:

$$\begin{aligned} f_x(2c) &= \mu f_z(2c) \,, \\ \Delta k_x \frac{\Delta v_1}{v} 2c &= \mu \Delta k_z \frac{4ac - 4c^2}{R} \,, \\ \Rightarrow c &= a - \frac{1}{2} \frac{G^*}{E^*} \frac{R}{\mu} \frac{\Delta v_1}{v} \,. \end{aligned} \tag{2.2.24}$$

As the displacement and the contact radii are known, one can determine the macroscopic force F_T via integration. Using equations (2.2.21) - (2.2.24) the tangential force reads:

$$F_T = \int_0^{2c} G^* \frac{\Delta v_1}{v} \zeta \mathrm{d}\zeta + \int_{2c}^{2a} \mu E^* \frac{2a\zeta - \zeta^2}{R} \mathrm{d}\zeta = \frac{4}{3} \frac{\mu}{R} E^* \left(a^3 - c^3\right) . \tag{2.2.25}$$

Division of equation (2.2.25) by the well-known Hertzian relation of equation (2.1.9) initially yields:

$$\frac{F_T}{F_N} = \mu \left(1 - \left(\frac{c}{a}\right)^3\right) . \tag{2.2.26}$$

Rearranging this equation, one obtains the same expression for the stick-radius as for the initial three-dimensional case as in equation (2.1.22) or shown in [55]:

$$\frac{c}{a} = \left(1 - \frac{F_T}{\mu F_N}\right)^{1/3} . \tag{2.2.27}$$

In addition rearranging (2.2.24) and inserting (2.2.27) gives the creep ratio ξ_1 of the one-dimensional MDR model:

$$\xi_1 = -\frac{\Delta v_1}{v} = -\frac{1}{2} \frac{E^*}{G^*} \frac{\mu a}{R} \left(1 - \left(1 - \frac{F_T}{\mu F_N}\right)^{1/3}\right) . \tag{2.2.28}$$

Given the relations for the effective modules [55]:

$$E^* = \frac{2G}{1-\nu} \quad \text{and} \quad G^* = \frac{4G}{2-\nu} , \tag{2.2.29}$$

one can compare the one-dimensional creep with the original creep ξ_x as stated in equation (2.1.21):

$$\xi_x = \frac{v - \omega R}{v} = -\frac{4 - 3\nu}{4\,(1-\nu)} \frac{\mu a}{R} \left(1 - \left(1 - \frac{F_T}{\mu F_N}\right)^{1/3}\right) . \tag{2.2.30}$$

This yields the following relation between the creep ratios:

$$\xi_1 = \frac{4\,(2-\nu)}{(4-3\nu)} \xi_x . \tag{2.2.31}$$

Equation (2.2.31) shows that the result of the one-dimensional system must be scaled in order to determine the correct creep of the three-dimensional system. The deviation is due to the asymmetry in the tangential stress distribution of the rolling contact [55, 56] that contradicts the MDR assumption of rotational symmetry of the contact configuration. In summary it shows that the MDR enables the mapping of the three-dimensional tractive rolling contact to a one-dimensional equivalent system. Thus the MDR allows to analyse more complex problems, such as the oscillating rolling contact as introduced in section 3.1. However, it must be ensured that the influence of potential contradictions to the MDR assumptions are cautiously taken into account.

2.3 Modelling of Frictional Systems

In this section some important aspects considering the modelling of frictional systems are briefly described. The principles introduced will be used in the following chapters.

2.3.1 Separation of Scales

As mentioned in the introduction of this chapter, one important characteristic of friction is the interaction between various factors as for instance the local deformation in the contact and the macroscopic motion of the system. However, under certain assumptions it is possible to separate certain time and space scales that contribute to the system.

Quasi-Statics The main requirement is quasi-statics of the contact problem [55]. A contact can be assumed to be quasi-static as long as its characteristic time of loading T_c is much larger than the time an elastic wave in the continuum needs to travel a distance of the order of the contact length D_c [67]:

$$T_c \gg \frac{D_c}{c_s} \,, \tag{2.3.1}$$

where c_s denotes the speed of sound of the material. This is fulfilled in most tribologic systems, as the speed of sound of the materials is much larger than the relative movement of components, which determines the contact time T_c. In consequence, the contacts instantaneously reach the equilibrium state. Thus, even in case of an unsteady loading one can apply static equilibrium conditions in every time step to calculate the forces and deformations in the contact.

Elastic Energy The linear elastic deformations in the contact decrease with $1/r$, with r being the distance to the contact area. In addition, the stresses and strains decrease in proportion to $1/r^2$. Therefore, the elastic energy of the deformation is concentrated in a volume with linear dimensions of the order of the contact width D_c [65]. The elastic energy of the contacts can thus be characterized as a *local* quantity that only depends on the conditions at the vicinity of the contact. In consequence it is independent from the size of the macroscopic body as well as other contacts of the system, as long as the distance between adjacent contacts is larger than their contact length [55].

Kinetic Energy In contrast, under most conditions, the kinetic energy of systems involving frictional contacts is a *non-local* quantity that is independent from the contact configuration. The kinetic energy of the system as a whole corresponds to the kinetic energy of the bulk body. Thus, the inertial properties of the system can be sufficiently described by the rigid body dynamics of the bulk body[65].

It should be emphasized that the elastic and kinetic energy of the system are not truly independent as both are connected through the forces and moments that act in the

contact and on the rigid body, i.e. Newton's third law. But both are decoupled through the separation of space scales. In case of dynamic problems this gives the possibility to determine the rigid body motion using the equations of motion and then solve for the contact configuration in every time step. In turn the resulting forces and moments serve as input parameters for determination of the next step of the rigid body motion.

2.3.2 Modelling of Coulomb Friction in Dynamic Systems

Once the static maximum holding force $F_{T,max} = \mu_s F_N$ is exceeded and sliding has started, the friction force drops to its lower kinetic value $F_R = \mu_k F_N$, where $\mu_k < \mu_s$. In addition, it was shown in numerous experiments that the kinetic friction is a function of the relative velocity v with a negative slope [77, 78, 9, 79]. This phenomenon is also referred to as *rate weakening* [38]. Both effects lead to a non-linear behaviour of mechanical systems with dry friction. A stick-slip motion may occur where the sliding surfaces alternately switch between sticking and slipping [3]. In the modelling, the distinction initially leads to a set of differential equations with discontinuous right hand side. One widespread solution is to apply a smoothing method for the frictional coefficient [9, 80] what yields a system of ordinary differential equations. A popular approach is to apply a velocity dependent coefficient as shown in Fig. 2.9 [81]:

$$\mu_k(v) = \mu_s \frac{2}{\pi} \frac{\arctan(\gamma v)}{1 + \frac{|v|}{\delta v}} , \tag{2.3.2}$$

where v denotes the relative velocity between the surfaces. In equation (2.3.2), the limiting velocity δv defines the velocity range in which static friction applies and γ determines the steepness around $v = 0$. However, this type of model has several drawbacks. Firstly, the unknown and in principle arbitrary parameters δv and γ need to be determined and there is no standard rule for their estimation. Secondly, this type of model cannot accurately represent sticking, since it allows a nearly stationary system, i.e. $v \to 0$, to accelerate even if the net tangential forces are less than the maximum holding force [38, 82]. This was also examined in detail by Elmer who states that any kinetic friction law as in (2.3.2) becomes invalid if:

$$v < \frac{D_c}{T_c} , \tag{2.3.3}$$

where D_c denotes the microscopic length scale and T_c the macroscopic time scale, i.e. the contact time [83]. Increasing the steepness parameter γ will improve the approximation around $v = 0$. However, this will also lead to large computation times as the differential equations become stiff, particularly in case of large frictional resistance. Another popular model is the so called force-balance method developed by Karnopp [84]. Here, for $v > \delta v$ the friction force is a function of the sliding velocity. For $v < \delta v$ the friction force is determined as such that it balances all other forces in the tangential direction in case of sticking, i.e. leads to zero acceleration, or matches the friction bound in case of slipping. An important extension of the force balance method is the switch model developed by

Leine et al. [81]. On basis of the velocity and the external forces it is determined whether the system slips or sticks and the corresponding time derivatives are chosen, i.e. the differential equation is changed. One drawback of the models introduced is their inability to describe so-called pre-sliding, an effect that is caused by the elastic deformation of the contact whenever a sticking system is loaded tangentially. This is effect is captured by the elastoplastic friction model [85] which is an extension of the commonly used Dahl-model [86]. However, the model consists of a number of empirical parameters which are difficult to determine. Some can be measured while others have to be chosen arbitrarily, so that they are more likely fitting parameters by nature [74]. In addition, Oden and Martins conclude that the exact slope of the friction function is not defined uniquely by the nature of the surfaces in contact, but is rather a consequence of all the dynamic variables involved [9]. Thus it is not only affected by the slip velocity but also by inertia and stiffness properties of the frictional system. Finally, a clear understanding of frictional sliding phenomena at small speeds has not been yet achieved and none of the models proposed has gained general acceptance [10].

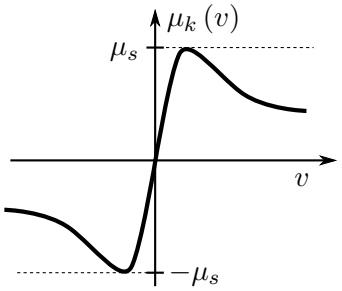

Fig. 2.9: smooth model function of velocity dependent coefficient of friction

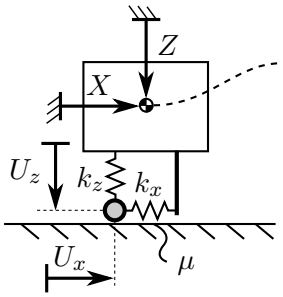

Fig. 2.10: rigid slider with elastic contact modelled as a linear spring

2.3.3 Algorithm for the Modelling of Contacts

The objective of this study is in particular to identify the influence of microscopic effects, e.g. the spatial variations of pressure and traction and the distribution of stick and slip in the contact interface, on the macroscopic behaviour of the system. Parameters that can be rather characterized as empirical, e.g. γ or δv, complicate the clear interpretation of the results. Thus, it is convenient to use a relatively simple friction model for the contact itself in order to separate the influences of system dynamics. This corresponds to the approach of Martins et al. [10]. Their model neglects the distinction between static and kinetic case and the dependency on the relative velocity. However, they were able to simulate apparently smooth sliding motions with apparent coefficients of kinetic friction smaller than the static one and also stick-slip oscillations. Hence, their relatively simple contact model and the interplay with the system dynamics reflects the experimentally observed dependencies on the velocity, although these dependencies are not considered in the initial contact model, i.e. μ is not a function of time or velocity.

Likewise in our model, the elastic deformations of the contact are taken into account without distinction between static and kinetic coefficient of friction. The model that is used in this work and its corresponding equations of motions are described in detail in section 4.1. In order to explain the basic principle, the rigid slider with two degrees of freedom X and Z is introduced, which is depicted in Fig. 2.10. On basis of the separation of scales approach as described in section 2.3.1 the contact is modelled as a linear spring with normal stiffness k_z and tangential stiffness k_x and corresponding spring deflections U_z and U_x. Thus, the spring forces are given as:

$$F_z = k_z U_z \quad \text{and} \quad F_x = k_x U_x \; . \tag{2.3.4}$$

Coulomb's law of dry friction applies in the contact with a microscopic coefficient of friction μ. Therefore the contact sticks whenever:

$$|F_x\,(t)\,| \leq \mu F_z \Leftrightarrow k_x |U_x\,(t)\,| \leq \mu k_z U_z\,(t) \; . \tag{2.3.5}$$

The deflections are dependent variables that are directly determined by the motion of the system, i.e. they depend on the translation X and Z. The time derivative of the normal spring deflection equals the normal velocity:

$$\dot{U}_z\,(t) = \dot{Z}\,(t) \; . \tag{2.3.6}$$

In accordance to the switch model [81] the friction force F_R and the tangential spring deflection are given by a case distinction. For this purpose a test deflection is calculated assuming sticking of the contact:

$$\tilde{U}_x\,(t) = U_x\,(t - \Delta t) + \Delta t \dot{X}\,(t - \Delta t)\,. \tag{2.3.7}$$

Here Δt denotes the time step. Thus, in case of sticking the rate of tangential deflection $\dot{U}_x$ corresponds to the velocity of the mass $\dot{X}$. Finally, the case distinction reads:

$$\begin{aligned}
k_x|\tilde{U}_x\,(t)\,| \leq \mu k_z U_z\,(t) \quad &\Rightarrow \text{sticking} \quad &&\Rightarrow F_R\,(t) = -k_x U_x\,(t) \; , \\
&&&\Rightarrow U_x\,(t) = \tilde{U}_x\,(t) \; , \\
k_x|\tilde{U}_x\,(t)\,| > \mu k_z U_z\,(t) \quad &\Rightarrow \text{slipping} \quad &&\Rightarrow F_R\,(t) = -\mu \,\text{sign}\left(\tilde{U}_x\,(t)\right) k_z U_z\,(t) \; , \\
&&&\Rightarrow U_x\,(t) = \mu \,\text{sign}\left(\tilde{U}_x\,(t)\right) \tfrac{k_z}{k_x} U_z\,(t) \; .
\end{aligned} \tag{2.3.8}$$

This algorithm ensures continuity of the so called state vector of the system without numerical instabilities and enables pre-sliding, as the rigid body can move tangentially even for sticking contacts. In a slightly modified form, this friction model is used for the analysis of systems with sliding friction in section 4. The modifications enable to consider the cases of completely released contacts, a spatial variation of stick and slip and negative spring deflections in the tangential direction. A detailed description of the model used in the analysis is given in section 4.1. In addition, the contact model is described in detail in appendix B.4.

Chapter 3

Shakedown and Ratcheting in Incomplete Contacts

Oscillating micro-slip can cause failure of frictional contacts in nominally static systems, i.e. systems that are intended to stay in a stable equilibrium without macroscopic slip. One has to distinguish three cases. Firstly, the system can shakedown what means that the slip ceases after the first few periods. Secondly, ratcheting can occur, where the micro-slip accumulates and leads to a continuing body motion. Thirdly, reversing slip might occur, what describes the situation in which no net tangential motion occurs. In the following chapter a model for a nominally static system is introduced, which consists of an incomplete contact, meaning that the contact area changes during oscillation. The exact shakedown limits are derived. These are the prerequisites that must be fulfilled in order for the system to shakedown. In addition, the supercritical case of ratcheting is examined. Finally, some variations of the initial system are considered.

3.1 Oscillating Rolling Contact

In order to give a generic model for a force locked connection with an incomplete contact, the so called oscillating rolling contact is introduced. Starting point is the tangentially loaded contact between a rigid sphere and an elastic substrate as described in section 2.1.1 and section 2.1.2. A good description for this system can also be found for example in [55] or [56]. As introduced before, the elastic modules E^* and G^* of the substrate, i.e. of the half-space, as well as the radius of the sphere R are effective quantities of a contact of two elastic spheres. The system is assumed to be uncoupled, meaning that variations in the normal force will not induce any tangential displacement and vice versa, i.e. Dundurs' constant $\beta = 0$ applies. Dry friction of the Coulomb type with constant coefficient μ between sphere and substrate is assumed. The sphere is pressed on the substrate by the normal force F_N and is additionally loaded with a tangential force F_T. The normal force leads to the indentation depth d, which is defined as the

vertical displacement of the rigid sphere:

$$d = \left(\frac{3F_N}{4E^* R^{\frac{1}{2}}} \right)^{2/3} . \tag{3.1.1}$$

The area of contact is delimited by the contact radius $a = \sqrt{Rd}$. A tangential loading F_T, insufficient to cause complete sliding, will lead to a slight rigid body displacement of the substrate in the direction of the force:

$$U_{stat} = \mu \frac{E^*}{G^*} d \left(1 - \left(1 - \frac{F_T}{\mu F_N} \right)^{2/3} \right) . \tag{3.1.2}$$

This static displacement refers to the relative shift of points that are sufficiently far away from the contact area, i.e. it equals the constant surface displacement as in (2.1.18). As shown in section 2.1.2 slipping will initially only occur at the boundary region of the contact area, whereas the centre region remains in a state of stick and is delimited by the stick-radius c as in (2.1.17):

$$c = a \left(1 - \frac{F_T}{\mu F_N} \right)^{1/3} . \tag{3.1.3}$$

In the next step, this static tangential contact is superposed by a slight oscillatory rolling of the sphere with amplitude W, being the lateral movement of the centre of the sphere, as depicted in Fig. 3.1 (a). The system is assumed to be quasi-static, meaning that a constant μ is assumed and inertia effects are neglected, as described section 2.3.1. This is valid as long as the excitation $\dot{W}$ is slower than the propagation speed of elastic waves c_s within the bodies, i.e. $\dot{W} \ll c_s$.

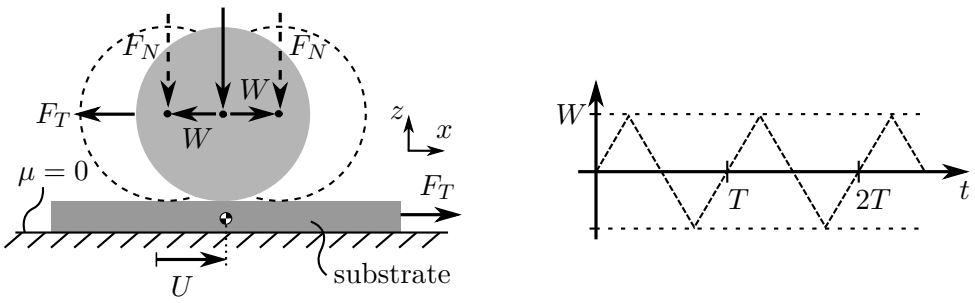

(a) oscillating rolling contact (b) time response of the rolling

Fig. 3.1: (a) oscillating rolling contact between rigid sphere and elastic substrate. Movement of the centre of the sphere is denoted by W and displacement of the substrate is denoted by U. (b) time response of the rolling W with oscillation period T

The overall macroscopic normal and tangential forces will both be kept constant in magnitude and the rolling will not induce any additional forces or moments. However, the rolling varies the contact area and leads to a periodic change of the pressure distribution.

As depicted in Fig. 3.2 the actual trailing edge is released and the corresponding friction bound $\tau_{max} = \mu p$ is reduced. According to this, the problem setting is equivalent to a frictional contact, which is exposed to an oscillatory back and forth movement of the normal force. This corresponds to a rocking motion of the contacting bodies. The system is thus the three-dimensional Hertzian counterpart of the rocking and walking punch [27, 28, 29] and represents a general model of force-locked connections where the contact area changes under the influence of vibrations.

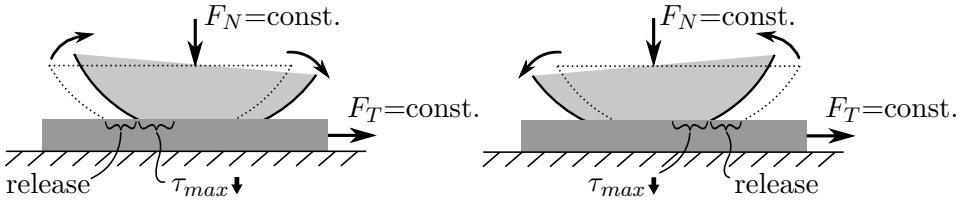

Fig. 3.2: oscillating rolling of the sphere releases the actual trailing edge and alternately reduces the friction bound τ_{max}

3.1.1 Influence of the Oscillating Rolling

In order to determine the influence of the oscillating rolling, the displacement of the substrate U is examined. The essential factors of influence are the tangential force F_T and the rolling amplitude W. All three variables are normalized as:

$$u = \frac{U}{U_{max}}, \quad f_T = \frac{F_T}{F_{T,max}}, \quad w = \frac{W}{a} \; . \tag{3.1.4}$$

Here $F_{T,max}$ equals the maximal holding force of equation (1.0.1) and U_{max} describes the static displacement in equation (3.1.2) for $F_T = F_{T,max}$:

$$U_{max} = \mu \frac{E^*}{G^*} d \; . \tag{3.1.5}$$

Only tangential forces below the maximum holding force and oscillation amplitudes smaller than the contact radius are considered:

$$f_T \leq 1 \quad \text{and} \quad w \leq 1 \; . \tag{3.1.6}$$

Consequently, without oscillatory rolling, no complete sliding will occur and the centre of the sphere will not be moved beyond the initial area of contact at any time. The latter means that there will always remain an area in the centre of the contact that is never released. Thus, taken by itself, neither of the two factors leads to a failure of the contact.
Figure 3.3 and Fig. 3.4 give the displacement u over rolling periods for $f_T = 0.09$ and $f_T = 0.72$ and different amplitudes w. These time responses are the product of the CONTACT simulation that is described in appendix B.2. They agree well with the experimental ones, that are shown in section 5.1.4. Both, simulation and experiment

show that the oscillatory rolling increases the displacement of the substrate with respect to the static value u_{stat}. For f_T and w being sufficiently small, the displacement stops and the system reaches a new equilibrium as shown in Fig. 3.3. This effect is characterized as a frictional shakedown and is explained in more detail in section 3.2. Otherwise, if f_T and w exceed certain limits, the displacement continues and so called ratcheting occurs. This case is shown in Fig. 3.4 and also in 3.3 for $w = 0.74$ and is discussed in section 3.3. Comparison of both cases shows that reaching the shakedown equilibrium requires more cycles than reaching a steady state ratcheting state.

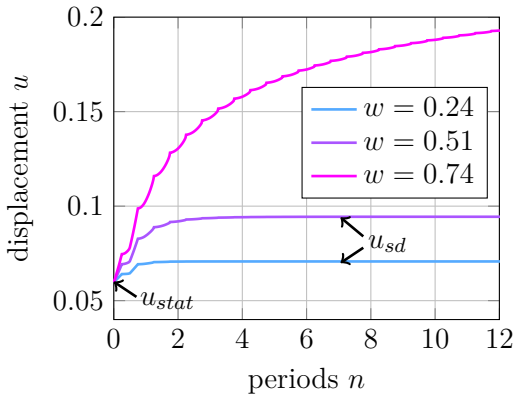

Fig. 3.3: displacement of the substrate u for $f_T = 0.09$ and different oscillation amplitudes w. Shakedown: displacement stops and system reaches a new equilibrium

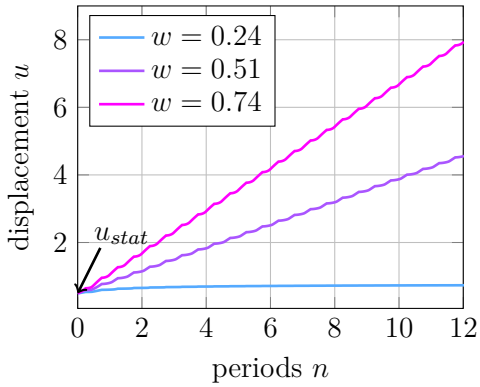

Fig. 3.4: displacement of the substrate u for $f_T = 0.72$ and different oscillation amplitudes w. Ratcheting: displacement continues with the rolling

3.1.2 MDR Model of the Oscillating Rolling Contact

In order to describe the introduced system, one can theoretically use the classical approach of Cattaneo [59] and Mindlin [60], as in described in section 2.1.2. For this purpose both the contact configuration, i.e. the distribution of stick and slip, as well as the distribution of stress must be known. Then the potential functions of Boussinesq and Cerruti [56] determine the tangential displacement of the substrate. It is at least doubtful whether this can be achieved for the given system, with its changing contact area and stress field.
The results of section 2.2.2 prove the usefulness of the MDR in the modelling of rolling contact problems. Therefore, the MDR is the method of choice for the description of the oscillating rolling contact. Again the profile of the sphere is transformed in accordance to the second step of the MDR, see equation (2.2.2):

$$R_{1D} = \frac{1}{2}R\,. \tag{3.1.7}$$

And the elastic substrate is replaced by an elastic foundation of independent, linear springs with normal and tangential stiffness Δk_z and Δk_x as stated in the first step of

the MDR, see equation (2.2.1):

$$\Delta k_z = E^* \Delta x \quad \text{and} \quad \Delta k_x = G^* \Delta x \; . \tag{3.1.8}$$

Both the initial model and the MDR model are shown in Fig. 3.5. One major advantage of the MDR is that due to the independence of the springs, the corresponding deflections of the springs can be directly determined by kinematic considerations. Consequently, the instantaneous displacement in the z-direction at the reversal points of the rolling yields:

$$U_z\left(x\right) = d - \frac{\left(x \mp W\right)^2}{2R_{1D}} = d - \frac{\left(x \mp W\right)^2}{R} \; , \tag{3.1.9}$$

where x gives the position of one particular spring. Using this relation one can derive the analytical description of the system. In addition, one can perform a quasi-static incremental simulation as described in more detail in appendix B.1.

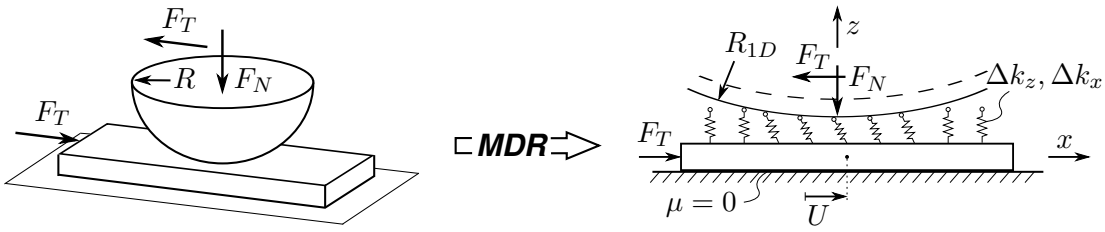

(a) three-dimensional contact (b) equivalent MDR model

Fig. 3.5: (a) three-dimensional tangential contact. (b) equivalent one-dimensional MDR model with mapped radius R_{1D}

3.2 Shakedown of the Oscillating Rolling Contact

The characteristic response in case of shakedown, which is shown in Fig. 3.3, can be explained as follows. At first, the system is in static equilibrium due to the constant macroscopic forces. As $f_T < 1$ the displacement of the substrate corresponds to the static value $u = u_{stat}$ of equation (3.1.2). The back and forth rolling of the sphere then alters the pressure distribution as depicted in Fig. 3.6. When the sphere starts to roll forward, the pressure at the trailing edge drops. As this reduces the friction bound $\tau_{max} = \mu p$ slipping occurs and the traction decreases at the trailing edge. At the same time, at the leading edge, the pressure increases but the traction initially remains constant. This results in an imbalance of force in the tangential direction. The same effect occurs, when the sphere rolls backwards. Thus, at first, this reduces the stick area and increases the rigid body displacement between sphere and substrate u within every back and forth movement of the sphere, as shown in Fig. 3.3. However, for sufficiently small f_T and w a saturation level is reached after a certain number of periods and the displacement stops. The residual force within the contact is sufficiently strong to prevent any further slip

and the system reaches a new equilibrium, i.e. the shakedown state. The displacement then corresponds to the constant, time independent shakedown displacement $u = u_{sd}$ [25].

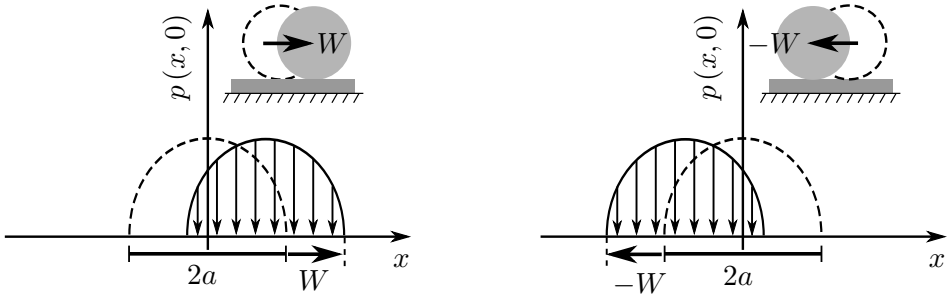

Fig. 3.6: alternating contact area and periodic displacement of the pressure distribution $p\,(x, y = 0)$ as a consequence of the rolling motion with amplitude W

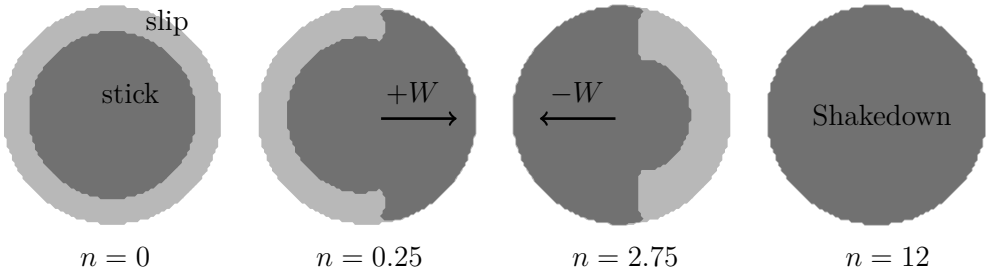

Fig. 3.7: distribution of stick (black) and slip (grey) area in case of shakedown after various numbers of rolling periods n for $w = 0.24$ and $f_T = 0.56$ (CONTACT Simulation). Slipping occurs on the actual trailing edge while the actual leading edge sticks. After several periods the system reaches a new equilibrium

Figure 3.7 depicts the time evolution of the contact area. In the beginning the contact area is divided into the stick and slip area[1]. Due to the rolling, slipping[2] occurs on the actual trailing edge while the actual leading edge sticks. In the centre of the contact area remains a region that permanently sticks. After several periods a shakedown occurs. Even if the rolling is continued, the whole contact area remains in a state of stick, respectively in a state of *no-slip* in case of the regions that are released periodically.
Another way to enlighten the transient process towards the shakedown state is to examine the frictional dissipation in one time step W_{fric}. A frictional shakedown is then and only then reached if W_{fric} vanishes. Hence, so called trailing edge slip may not occur, as this would refer to the case of reversing slip. The frictional dissipation is defined as the integral of the traction $\tau\,(x, y)$ times the local slip displacement $s\,(x, y)$ in one time step

[1]This means that the friction bound $\tau_{max} = \mu p$ is reached.
[2]This refers to a relative motion between particles.

over the slip area $\mathcal{A}_{slip}$ [87]:

$$W_{fric} = \int_{\mathcal{A}_{slip}} \tau\,(x,y)\,s\,(x,y)\mathrm{d}A\ . \tag{3.2.1}$$

The CONTACT model with world fixed (space-fixed) approach and 55 x 45 quadratic discretization elements with a grid-size of $\Delta x, \Delta y = 0.22$ mm and the parameters of the experimental setting as described in 5.1.1 is used to compute W_{fric}. The dissipation of one cycle of an oscillating tangential loading with amplitude F_T [56]:

$$W_0 = \frac{18\mu^2 F_N^2}{G^* 5a}\left(1-\left(1-\frac{F_T}{\mu F_N}\right)^{5/3} - \frac{5}{6}\frac{F_T}{\mu F_N}\left(1-\left(\frac{F_T}{\mu F_N}\right)^{2/3}\right)\right)\ . \tag{3.2.2}$$

is used for normalization. The results consistently show, that the frictional dissipation decreases rapidly after the first few periods, as depicted in Fig. 3.8.

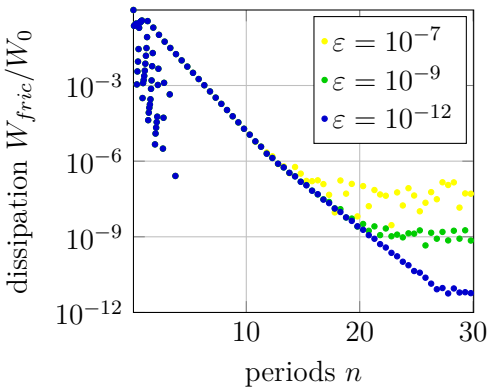

Fig. 3.8: normalized dissipation per time step W_{fric}/W_0 for different relative accuracies ε in case of shakedown

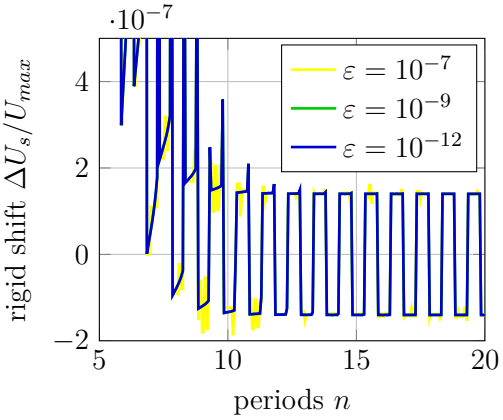

Fig. 3.9: normalized rigid body shift per time step U_s/U_{max} for different relative accuracies ε in case of shakedown

Afterwards for $n > 5$, dissipation and thus trailing edge slip only occurs exactly in the reversal points of the rolling motion. The dissipation then decreases constantly with each half period and finally reaches a level, that depends on the requested relative accuracy of the output variables ε. The normalized dissipation is in the range of $10^{-7} - 10^{-13}$ at the end of the process[3]. The corresponding rigid body shift per time step ΔU_s is given in Fig. 3.9 and shows that the dissipation in the steady state is caused by a numerical effect. There occurs a characteristic back and forth motion in the region of constant dissipation, which lacks any physical background. A constant tangential force, as it is the case here, cannot produce a reciprocating motion in the tangential direction. Besides, for elastically similar materials ($\beta \approx 0$), slip always occurs in the same direction, that

[3]For the parameters used in the simulation this corresponds to $2 \cdot 10^{-14}$ J, i.e. the rest mass-energy of elementary particles.

is given by the tangential load [29]. Thus reversing slip cannot occur as $f_T = const.$. Additionally, the amplitude of the shift is quite small again[4]. One can conclude that both, the characteristic motion and the according dissipation, are most likely caused by the iteration process. It is based on a Newton-Raphson procedure [88], which does not improve the solution any more, when the requested relative accuracy is reached. This corresponds exactly to the system behaviour in the steady state as shown in Fig. 3.8 and Fig. 3.9 for $n > 10$. Taking into account the arguments above, the residual dissipation and rigid body shift can be neglected. Consequently, neither slipping nor dissipation will occur when the new equilibrium has been reached. One can conclude that the system response is a true frictional shakedown. Reversing slip will not occur as the direction of the tangential force does not change during the oscillation [29]. Figure 3.9 shows that the new equilibrium is reached after $n \approx 10$ cycles. After this, the only displacement is the non-physical back and forth motion.

3.2.1 Contact Configuration after Shakedown

In order to analyse the contact configuration in the new equilibrium, the CONTACT model with world fixed approach, see appendix B.2, and 108 x 89 quadratic discretization elements with a side length of $\Delta x, \Delta y = 0.11$ mm and the parameters of the experimental setting as described in section 5.1.1 in Tab. 5.1.1 is used. Figure 3.10 depicts the normalized traction $\tau(x,y)/\mu p_0$ after shakedown, where p_0 denotes the static maximum pressure at $(x,y) = (0,0)$ [55]:

$$p_0 = \frac{2}{\pi} E^* \left(\frac{d}{R}\right)^{1/2} . \tag{3.2.3}$$

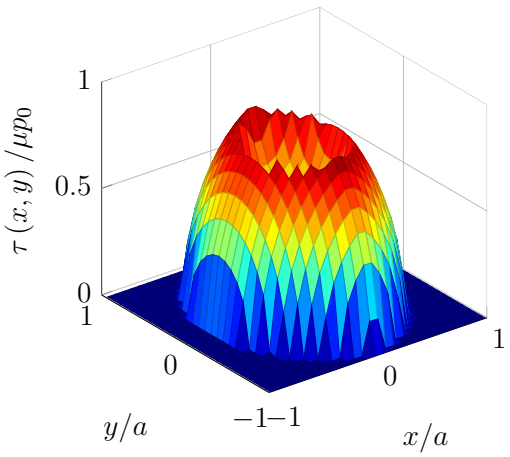

Fig. 3.10: traction $\tau(x,y)/\mu p_0$ after shakedown for $w = 0.24$ and $f_T = 0.56$ (CONTACT model)

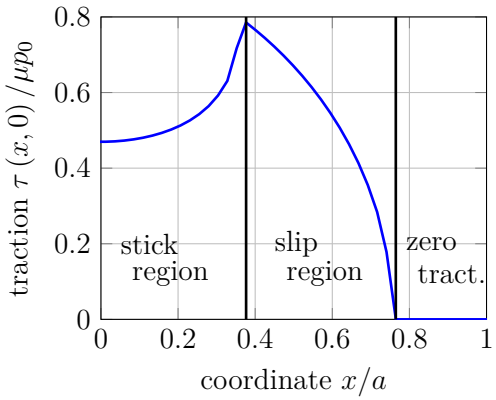

Fig. 3.11: traction $\tau(x, y = 0)/\mu p_0$ after shakedown at the centre line aligned parallel to the rolling for $w = 0.24$ and $f_T = 0.56$ (CONTACT model)

[4]This corresponds to 5 nm for the experimental parameters.

It shows that in the new equilibrium, there occur three characteristic contact regions. These are illustrated in Fig. 3.11 where the normalized traction is shown along the centre line aligned parallel to the rolling, i.e. $\tau(x, y = 0)$. In the centre occurs the *stick region*, where the displacement of particles u_x must match the shakedown displacement u_{sd} in order to meet the sticking condition. Adjacent thereto occurs the *slip region*, where the tangential stress equals the traction bound that appears at the reversal point of the rolling. Finally, at the outside of the contact, occurs the *zero traction* region. Here, the traction vanishes as the sphere is periodically released and no trailing edge slip occurs in shakedown state. The total contact after shakedown is configured as follows:

$$\begin{aligned} \text{stick-region:} \quad & U_x = \text{const.} \,, \\ \text{slip-region:} \quad & \tau = \mu p \,, \\ \text{zero-traction:} \quad & \tau = 0 \,. \end{aligned} \tag{3.2.4}$$

The according normalized tangential displacement of particles in the contact region $u_x(x, y) = U_x(x, y)/U_{max}$ is depicted in Fig. 3.12. It shows that the stick region in the centre is slightly spindle shaped, see also Fig. 3.15. Figure 3.13 gives the centreline-displacement of particles $u_x(x, y = 0)$. In the stick region the displacement u_x corresponds to the constant shakedown displacement u_{sd}.

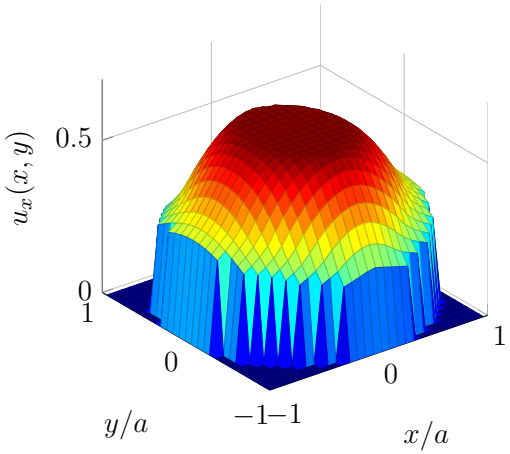

Fig. 3.12: tangential displacement $u_x(x, y)$ after shakedown for $w = 0.24$ and $f_T = 0.56$ (CONTACT model)

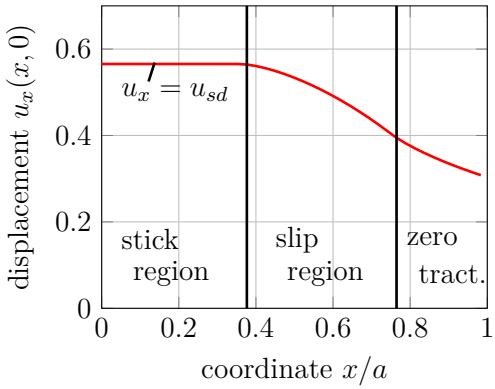

Fig. 3.13: tangential displacement $u_x(x, y = 0)$ after shakedown at the centre line aligned parallel to the rolling for $w = 0.24$ and $f_T = 0.56$ (CONTACT model)

The displacement of particles $u_x(x, y)$ for a given traction $\tau(x, y)$ and contact area is determined by the potential functions of Boussinesq and Cerruti [56]. However, even if the exact distribution of $\tau(x, y)$ is identified, it remains vague whether a closed solution of the integral of this classical approach exists. Instead, the MDR model as introduced in section 3.1.2 is used, where the displacements can easily be identified from kinematic relations. Figure 3.14 shows $u_x(x)$ for the MDR model. The blue line symbolizes the static displacement before shakedown and the red line the displacement after shakedown.

As for the initial three dimensional case, there remain three contact regions. The stick region in the centre is delimited by the stick radius after shakedown c_{sd}. Here u_x matches the shakedown displacement u_{sd}, which is increased in comparison to the static value u_{stat}. Adjacent to the stick region occurs the slip region which is delimited by the slip radius b. In this region, the tangential spring forces match the lowest friction bound of the process, which occurs exactly at the reversal points of the rolling. Finally, at the outside of the contact area occurs a region in which the displacement and hence the tangential force is zero due to the alternating release of the springs. In order to determine the contact configuration, it is briefly returned to the dimensionful notation. Here, the normal and tangential spring forces f_z and f_x are given as:

$$f_z(x) = \Delta k_z U_z(x) \quad \text{and} \quad f_x(x) = \Delta k_x U_x(x) \ . \tag{3.2.5}$$

The minimal normal displacement is reached in the reversal point of the rolling:

$$U_z(x) = d - \frac{(x \mp W)^2}{R} \text{ for } -a \pm W \leq x < a \pm W \ . \tag{3.2.6}$$

Thus, together with the friction bound $f_x(x) = \mu f_z(x)$ and equation (3.2.5) the tangential displacement in the slip region yields:

$$U_x(x) = \mu \frac{E^*}{G^*} U_z(x) = \mu \frac{E^*}{G^*} \left(d - \frac{(x+W)^2}{R} \right) \text{ for } c_{sd} \leq |x| < b \ . \tag{3.2.7}$$

At position $x = c_{sd}$ this must exactly match the shakedown displacement what determines the missing stick radius:

$$U_{sd} = U_x(x = c_{sd}) \ , \tag{3.2.8}$$

$$U_{sd} = \mu \frac{E^*}{G^*} \left(d - \frac{(c_{sd}+W)^2}{R} \right) \ , \tag{3.2.9}$$

$$\Leftrightarrow c_{sd} = \sqrt{\left(d - \frac{G^*}{\mu E^*} U_{sd} \right) R} - W \ . \tag{3.2.10}$$

The slip radius directly depends on the rolling amplitude and is given as:

$$b = a - W \ . \tag{3.2.11}$$

In summary the contact configuration after shakedown for the MDR system reads:

$$\begin{aligned} \text{stick-region:} \quad & 0 \leq |x| \leq c_{sd} && \Rightarrow U_x(x) = U_{sd} \ , \\ \text{slip-region:} \quad & c_{sd} < |x| \leq b && \Rightarrow U_x(x) = \mu \tfrac{E^*}{G^*} \left(d - \tfrac{(x+W)^2}{R} \right) \ , \\ \text{zero-force:} \quad & b < |x| \leq a && \Rightarrow U_x(x) = 0 \ . \end{aligned} \tag{3.2.12}$$

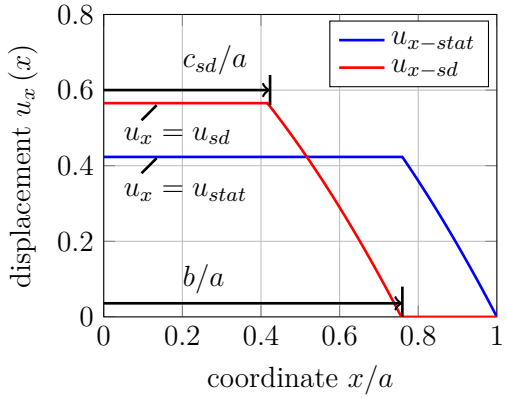

Fig. 3.14: displacement $u_x(x)$ before and after shakedown for $w = 0.24$ and $f_T = 0.56$ (MDR model)

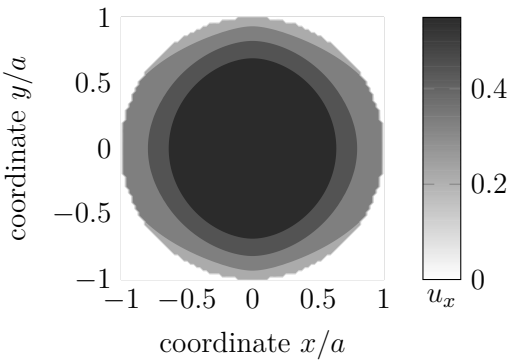

Fig. 3.15: displacement $u_x(x, y)$ after shakedown for $w = 0.24$ and $f_T = 0.56$ (CONTACT model)

With the complete contact configuration being known, it is possible to determine the equilibrium condition. After shakedown, the external tangential force F_T must match the overall tangential force of the springs:

$$F_T = \int_{\mathcal{F}} \mathrm{d}F_x = \int_{\mathcal{L}_c} G^* U_x(x)\mathrm{d}x \,, \tag{3.2.13}$$

where $\mathcal{L}_c$ denotes the contact length. With the symmetric contact configuration this yields the following integral:

$$F_T = 2\int_0^{c_{sd}} G^* U_{sd}\mathrm{d}x + 2\int_{c_{sd}}^{b} \mu E^* \left(d - \frac{(x+W)^2}{R}\right)\mathrm{d}x \,. \tag{3.2.14}$$

Finally, inserting equations (3.2.10) and (3.2.11) into (3.2.14) gives the equilibrium condition in normalized form:

$$f_T = 1 - \frac{3}{2} w u_{sd} - (1 - u_{sd})^{3/2} \,. \tag{3.2.15}$$

Equation (3.2.15) specifies the relation between tangential load f_T, oscillation amplitude w and shakedown displacement u_{sd}. Thus, on the one hand it enables to determine u_{sd} for a given combination of f_T and w using numerical solving procedures. On the other hand, it is possible to derive the shakedown limits, i.e. the maximal values for f_T and w for which a safe shakedown occurs. Both is shown in section 3.2.2.
However, the equilibrium condition (3.2.15) is the direct result of the MDR, which is based on the assumption of rotational symmetry of the contact region [67]. Figure 3.15 gives the tangential displacement in the contact region computed with the three-dimensional simulation. The contour lines show that the distribution of tangential displacement is slightly elliptic or spindle shaped. This can be seen especially at the stick region of constant displacement in the centre. Consequently, a small deviation in

the relation between loading and oscillation amplitude of equation (3.2.15) is expected. Considering this, the mapping parameter κ is introduced, such that:

$$f_T = 1 - \kappa w u_{sd} - (1 - u_{sd})^{3/2} . \tag{3.2.16}$$

3.2.2 Shakedown Limits

Expression (3.2.16) enables the prediction of the shakedown displacement u_{sd} for a given combination of f_T and w below the shakedown limits. The unknown mapping parameter κ is gained via comparison with the results of the experiments, where the goodness of the fitting procedure is given in appendix A.1.3 in Tab. A.1.1. The fitting indicates $\kappa = 1$. Finally, this yields the following expression for the relation of shakedown displacement, tangential force and oscillation amplitude:

$$f_T = 1 - w u_{sd} - (1 - u_{sd})^{3/2} . \tag{3.2.17}$$

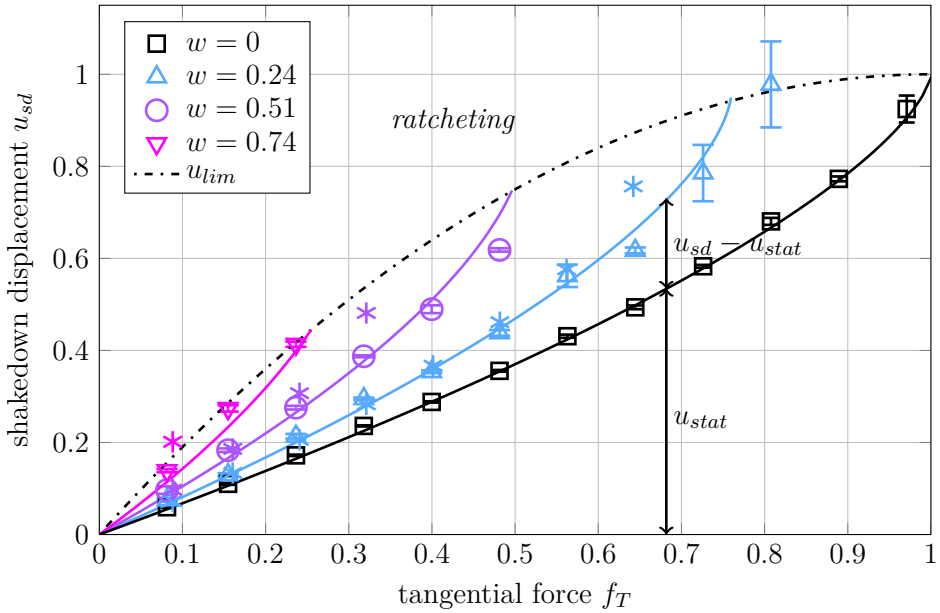

Fig. 3.16: shakedown displacement u_{sd} as a function of the tangential force f_T for different amplitudes w determined with equation (3.2.17). The oscillating rolling increases the displacement with respect to the static value u_{stat}

Figure 3.16 illustrates u_{sd} as a function of f_T for different w. The solid lines show the analytical results of (3.2.17), whereas the experimental results are indicated by the errorbars and marks. The asterisks depict the results for the three-dimensional CONTACT simulation, where values for tangential forces close to the shakedown limit are not given, because the iterative solution procedure of CONTACT lacks robustness in this case [88]. As mentioned before, it shows that u_{sd} is increased in comparison with the static value

u_{stat}. It is also known that in the case that the oscillating rolling stops to soon, the final displacement might differ from this theoretical shakedown value [25]. In the experiments, the shakedown state is already reached after $n \approx 10$ rolling periods. This corresponds to the simulation results shown in the beginning of section 3.2. The dotted line in Fig. 3.16 indicates the maximal displacement for different amplitudes that is achieved, before the oscillation leads to a complete failure of the contact. In this case, the stick radius c_{sd} is zero, which in combination with equations (3.2.10) and (3.2.17) gives the maximal tangential force:

$$f_{T,lim} = 1 - w_{lim} \ , \tag{3.2.18}$$

and the maximal displacement:

$$u_{lim} = 2f_{T,lim} - f_{T,lim}^2 \ . \tag{3.2.19}$$

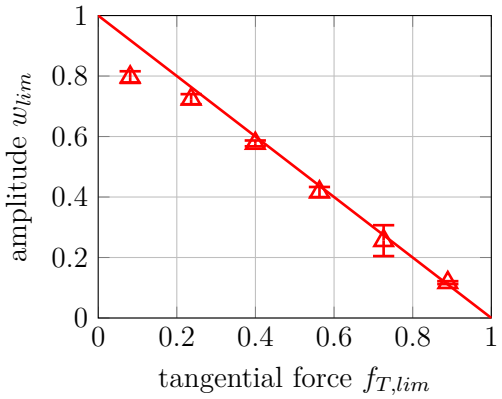

Fig. 3.17: maximal amplitude w_{lim} as a function of the tangential force $f_{T,lim}$ determined with equation (3.2.18)

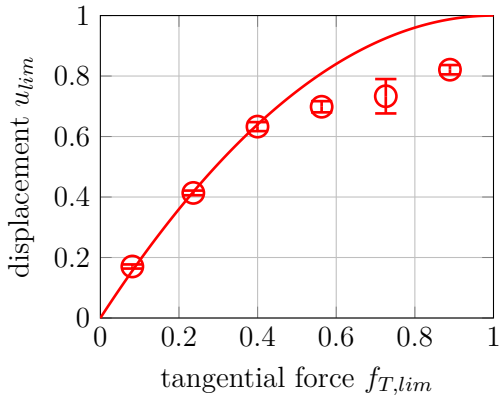

Fig. 3.18: maximal displacement u_{lim} as a function of the tangential force $f_{T,lim}$ determined with equation (3.2.19)

Figure 3.17 and Fig. 3.18 give the analytical (solid lines) and experimental (error-bars and marks) results for the shakedown limits. For medium tangential forces, both w_{lim} and u_{lim} show strong agreement with the theory. Fig. 3.17 gives $w_{lim} = 1 - f_{T,lim}$ since in the experiments, the maximal amplitude is identified by increasing it stepwise while f_T is kept constant. The exact experimental procedure for the determination of the shakedown limits is described in section 5.1.4.
These maximal values correspond to the analytical shakedown limits for the oscillating rolling contact. Thus, for a given oscillation amplitude w, the maximum tangential force $f_{T,lim}$ to achieve a safe shakedown can be identified and vice versa. Additionally, since $f_{T,lim} \leq 1$, it turns out that in case of the oscillatory elastic rolling contact, shakedown is accompanied with a significant reduction of the tangential loading capacity. This effect must be considered in the design and construction of frictional contact systems under the influence of vibrations of the type that is being regarded here.

3.3 Ratcheting of the Oscillating Rolling Contact

In case that f_T or w exceed the shakedown limit stated in equation (3.2.18), i.e. $f_T > f_{T,lim}$ or $w > w_{lim}$, the contact fails and frictional ratcheting occurs. At first the system responses as in the shakedown case. The rolling causes alternating slipping processes at the actual trailing edge and the initial sticking area in the centre decreases. In turn this increases the rigid body displacement within every period. As shown in Fig. 3.19 the initial sticking area vanishes completely after only a few rolling periods. Thus, the system does not reach the shakedown equilibrium. Instead, one side of the contact alternately sticks, while the other slips in dependence on the actual rolling direction. This leads to an accumulated rigid body displacement of the substrate also referred to as ratcheting or walking [27, 28, 29] as shown in Fig. 3.4.

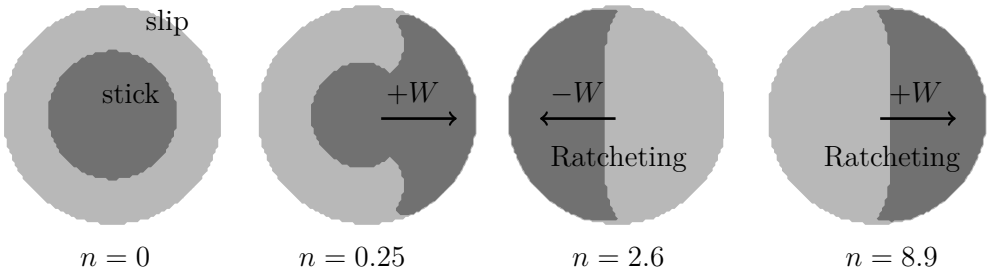

Fig. 3.19: distribution of stick (black) and slip (grey) area in case of ratcheting after various numbers of rolling periods n for $w = 0.24$ and $f_T = 0.8$ (CONTACT Simulation). Slipping occurs on the actual trailing edge while the actual leading edge sticks

The displacement per period, respectively the incremental displacement Δu is an increasing function of f_T and w, as depicted in Fig. 3.21. Here marks and error-bars depict experimental results. Solid lines give an approximation function which is gained on basis of the MDR model. For this purpose at first a parameter study is conducted using the incremental MDR-simulation as described in appendix B.1. This shows that Δu is proportional to the supercritical portion of the oscillation amplitude:

$$\Delta u = \eta \, (w - w_{lim}) \ . \tag{3.3.1}$$

The constant of proportionality η is a function of u_{stat} and is displayed in Fig. 3.20. The blue line gives the numerical results on basis of the MDR simulation. The red line gives the approximation function:

$$\eta_{fit} = 4.77\sqrt{u_{stat}} \ , \tag{3.3.2}$$

which is the outcome of a linear regression analysis with u_{stat} as the regressor. For static displacements in the region of $0.2 \leq u_{stat} \leq 0.8$ this expression differs $\pm 5\%$ from the results of the MDR simulation. The resulting function is then adapted to the experimental results what yields $\eta_{exp} \approx \sqrt{2u_{stat}}$ and thus:

$$\Delta u = \sqrt{2u_{stat}} \, (w - w_{lim}) \ . \tag{3.3.3}$$

The goodness of the fitting is given in appendix A.1.3 in Tab. A.1.1. The small deviation between η_{fit} and η_{exp} can again be explained with the violated rotational symmetry[5], which is one of the basic assumptions of MDR. Finally, for consistency reasons, equation (3.1.2) is inserted what gives the function that is depicted in Fig. 3.21:

$$\Delta u = \sqrt{2\left(1-(1-f_T)^{2/3}\right)}\,(w - w_{lim}) \ . \tag{3.3.4}$$

It must be noted that w_{lim} also depends on f_T, as stated in equation (3.2.18). The results show qualitatively good agreement with those for the walking of a rocking punch, as examined by Mugadu et al. [27].

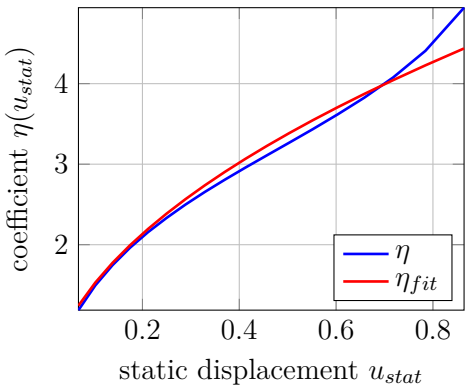

Fig. 3.20: coefficient η as a function of the static displacement. Blue line gives results of MDR simulation and red line gives approximation function (3.3.2)

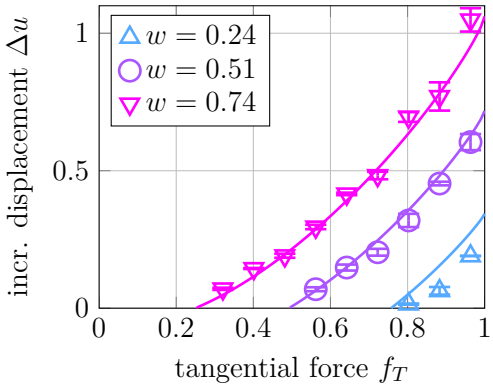

Fig. 3.21: incremental displacement Δu as a function of the tangential force f_T for different oscillation amplitudes w in case of ratcheting. Solid lines give approximation function (3.3.4)

Once the oscillating rolling stops, the incremental displacement stops as well. Thus, the ratcheting effect must not only have a negative impact, but can also be used for the generation and control of small displacements in case that an increase of the tangential loading is impossible or if high accuracy is needed as in micro-electromechanical systems (MEMS). Using equation (3.3.4) one can calculate this supercritical system response.

[5]In fact the contact region isn't even axial symmetric for ratcheting of the oscillating sphere.

3.4 Influence of the Alignment of Load and Oscillation

In addition to the system introduced in section 3.1, also the case of oscillation and tangential loading being perpendicular to each other is examined. This setting is shown in Fig. 3.22 (b) where $W_\perp$ describes the rolling amplitude of the centre of the sphere in the y-direction.

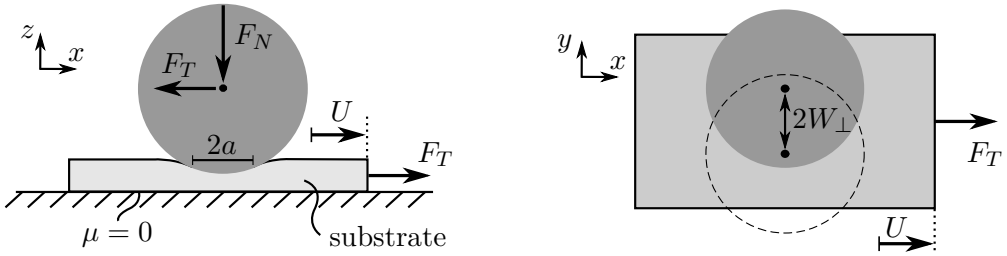

(a) static tangential contact

(b) perpendicular rolling

Fig. 3.22: (a) static tangential contact and (b) oscillating, elastic rolling contact with the lateral motion of the sphere $W_\perp$ being perpendicular to the tangential loading F_T

The normalization of the parallel setting given in equation (3.1.4) is used for the perpendicular setting. Likewise, tangential forces below the maximum holding force and oscillation amplitudes smaller than the contact radius are assumed. Only numerical results of the CONTACT simulation are reported here. For the simulation of a both cases a world fixed approach with 61 x 50 quadratic discretization elements with side length $\Delta x, \Delta y = 0.2$ mm and the parameters of the experimental setting as described in section 5.1.2 in Tab. 5.1.2 is used. The numerical model is described in appendix B.2.

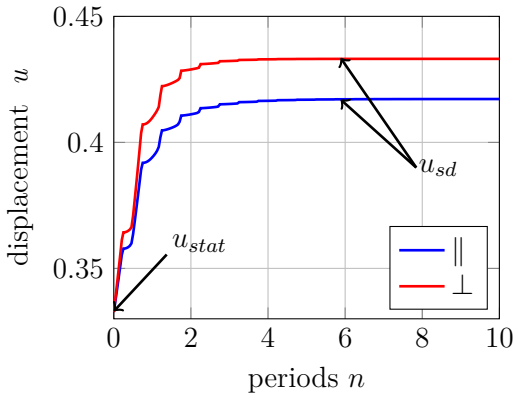

Fig. 3.23: displacement of the substrate u for $w \parallel f_T$ and $w \perp f_T$ with $w = 0.23$ and $f_T = 0.46$. Displacement stops and shakedown occurs

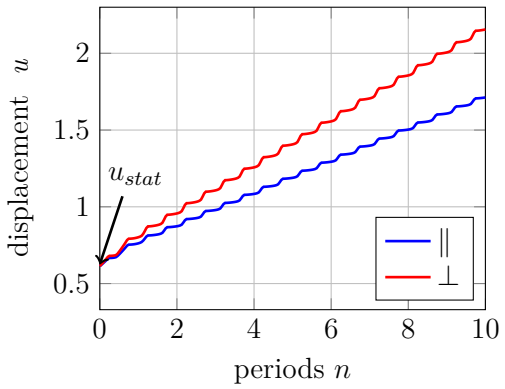

Fig. 3.24: displacement of the substrate u for $w \parallel f_T$ and $w \perp f_T$ with $w = 0.23$ and $f_T = 0.77$. Displacement continues and ratcheting occurs

The system response as a result to the oscillation is the same in both cases, parallel and

perpendicular. Again, it shows that the oscillatory rolling initially leads to an increase of the rigid body displacement with respect to the static value, as depicted in Fig. 3.23 and Fig. 3.24. In case that f_T and w fall below the shakedown limits, the displacement stops after a certain number of periods and a shakedown occurs as in Fig. 3.23. The system reaches a new equilibrium and the displacement refers to the constant, time independent shakedown displacement $u = u_{sd}$ [25] as described in section 3.2. Otherwise, if f_T and w exceed the shakedown limits, the contact fails and the displacement continues with the oscillation as in Fig. 3.24. An accumulated displacement described as ratcheting occurs [27] as described in section 3.3.

3.4.1 Contact Configuration after Shakedown

Whether the alignment is parallel or perpendicular, the system response to the rolling is the same. Alternating slip processes occur at the actual trailing edge that increase the rigid body displacement. Finally, the system reaches a new equilibrium where three characteristic contact regions occur as depicted in Fig. 3.25. Here the traction τ along the centre line aligned parallel to the rolling is given for both settings, i.e. $\tau\,(x, y = 0)$ for $w \parallel f_T$ respectively $\tau\,(x = 0, y)$ for $w \perp f_T$. The parallel centre lines are also symbolized by the dashed lines in Fig. 3.29.

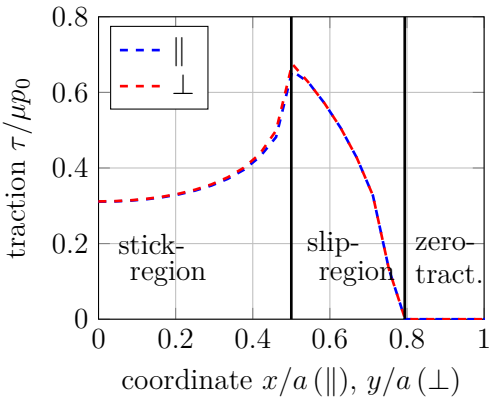

Fig. 3.25: traction $\tau/\mu p_0$ after shakedown along the centre line aligned parallel to the rolling for $w \parallel f_T$ and $w \perp f_T$ with $w = 0.23$ and $f_T = 0.46$ (CONTACT model)

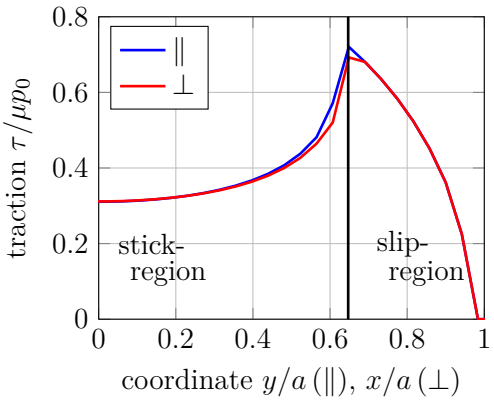

Fig. 3.26: traction $\tau/\mu p_0$ after shakedown along the centre line aligned perpendicular to the rolling for $w \parallel f_T$ and $w \perp f_T$ with $w = 0.23$ and $f_T = 0.46$ (CONTACT model)

It shows that the contact configuration is very much the same in both cases the only difference being the alignment, i.e. x for $w \parallel f_T$ and y for $w \perp f_T$:

$$\begin{aligned} \text{stick-region:} \quad & U_x = \text{const.}\ , \\ \text{slip-region:} \quad & \tau = \mu p\ , \\ \text{zero-traction:} \quad & \tau = 0\ . \end{aligned} \tag{3.4.1}$$

Fig. 3.26 gives the traction aligned perpendicular to the rolling direction. The perpendicular centre lines are symbolized by the solid lines in Fig. 3.29. In both cases the zero-traction region almost vanishes along the perpendicular line. However, the traction distribution slightly differs for both cases. Along the parallel centre line shown in Fig. 3.25, it is higher for the perpendicular setting. And vice versa, along the perpendicular centre line, which is depicted in Fig. 3.26, it is higher for the parallel case. The difference of the displacement of particles is more obvious, as illustrated in Fig. 3.27 and Fig. 3.28, which show u_x along the centre lines. In accordance with the observations of section 3.4, u_x in the stick region is higher for $f_T \perp w$. However, along the parallel centre line, u_x in the slip- and zero traction-regions is higher for $w \parallel f_T$. This is expected, since the overall tangential force is the same in both cases and a higher displacement in the centre is equalized by a lower displacement in the outer region. The difference in the traction and displacement distribution is caused by the evolution of the contact during the shakedown process. As a result, the direction of the oscillation influences the final shakedown displacement.

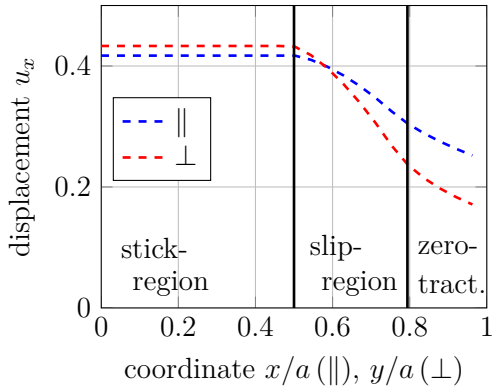

Fig. 3.27: tangential displacement u_x after shakedown along the centre line aligned parallel to the rolling for $w \parallel f_T$ and $w \perp f_T$ with $w = 0.23$ and $f_T = 0.46$ (CONTACT model)

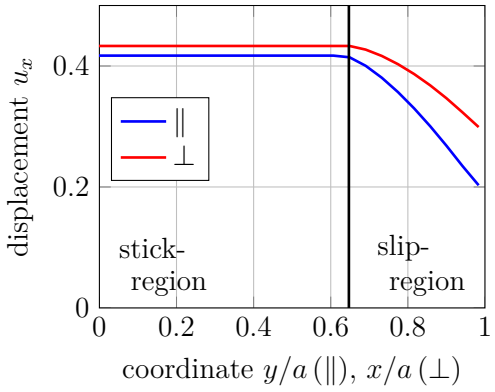

Fig. 3.28: tangential displacement u_x after shakedown along the centre line aligned perpendicular to the rolling for $w \parallel f_T$ and $w \perp f_T$ with $w = 0.23$ and $f_T = 0.46$ (CONTACT model)

3.4.2 Shakedown Limits for the Perpendicular Case

As in the parallel case, using the MDR the perpendicular rolling contact is mapped to a one-dimensional elastic foundation and a rigid indenter with stretched radius. The influence of the oscillating rolling on the vertical displacement of springs in contact U_z can again be directly deduced from kinematic relations. In the reversal points of the rolling for both settings applies:

$$U_z(s) = d - \frac{(s \mp W)^2}{R} \quad \text{for} \quad -a \pm W \leq s \leq a \pm W \; . \tag{3.4.2}$$

Here, the coordinate s points in the x-direction for $w \parallel f_T$ and in the y-direction for $w \perp f_T$, as shown in Fig. 3.29. The influence of the rolling on the normal contact is thus identical in both cases[6]. However, since the MDR requires rotational symmetry and decoupled systems, the tangential displacements and the contact region must be the same for both settings[7]. Consequently, the equilibrium condition is the same for both settings:

$$f_T = 1 - \frac{3}{2} w u_{sd} - (1 - u_{sd})^{3/2} \ . \tag{3.4.3}$$

However, a different relation between loading and oscillation amplitude, i.e. a different mapping parameter κ, is expected:

$$w \parallel f_T \Rightarrow f_T = 1 - \kappa_{\parallel} w u_{sd} - (1 - u_{sd})^{3/2} \ , \tag{3.4.4}$$

$$w \perp f_T \Rightarrow f_T = 1 - \kappa_{\perp} w u_{sd} - (1 - u_{sd})^{3/2} \ . \tag{3.4.5}$$

Comparison with the simulation and the experiments yields the different mapping parameters for the two cases:

$$\kappa_{\parallel} = 1 \quad \text{and} \quad \kappa_{\perp} = 1.1 \ . \tag{3.4.6}$$

what gives:

$$w \parallel f_T \Rightarrow f_T = 1 - w u_{sd} - (1 - u_{sd})^{3/2} \ , \tag{3.4.7}$$

$$w \perp f_T \Rightarrow f_T = 1 - 1.1 w u_{sd} - (1 - u_{sd})^{3/2} \ . \tag{3.4.8}$$

Again, the goodness of the fitting is shown in the appendix A.1.3 in Tab. A.1.1.

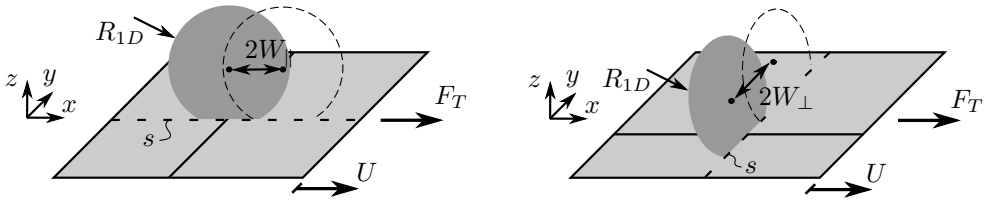

Fig. 3.29: equivalent one-dimensional MDR model. The control variable s is aligned in the x-direction for the parallel case (left) and aligned in the y-direction for the perpendicular case (right)

Fig. 3.30 shows the shakedown displacement u_{sd} as a function of the tangential force f_T for different amplitudes w. Dashed lines are computed with equation (3.4.7) and solid lines are computed with equation (3.4.8). The error-bars and marks show experimental results for $w \perp f_T$. Experimental results for $w \parallel f_T$ are given in section 3.2. The

[6]The reason for the change of vertical displacement, i.e. parallel or perpendicular rolling, does not make a difference for one specific spring.

[7]At least within in the MDR model.

corresponding CONTACT simulation results are indicated by the asterisks. As for the parallel case, values close to the shakedown limit are not given because CONTACT lacks accuracy close to the traction bound [88]. Comparison of the theoretical, experimental and numerical results shows that the shakedown displacement u_{sd} is slightly higher for a perpendicular setting of tangential load and rolling direction.

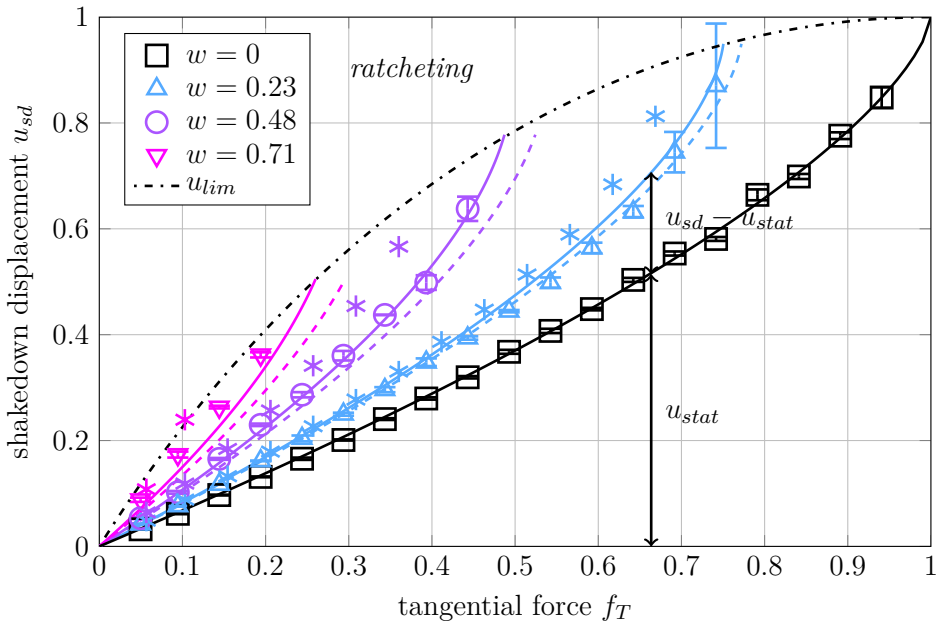

Fig. 3.30: shakedown displacement u_{sd} as a function of f_T for different w. Solid lines give (3.4.8) and dashed lines give (3.4.7). The oscillating rolling increases the displacement in comparison to the static value u_{stat}. Perpendicular alignment $w \perp f_T$ leads to higher u_{sd} than parallel alignment $w \parallel f_T$

The dash-dot line gives the maximal displacement u_{lim} as a function of f_T, that is achieved before complete sliding occurs and the contact fails. With the vanishing stick radius condition $c_{sd} = 0$ and equation (3.2.10) one gets the same expression for the two cases:

$$w \parallel f_T \Rightarrow u_{lim} = 1 - w_{T,lim}^2 \,, \tag{3.4.9}$$

$$w \perp f_T \Rightarrow u_{lim} = 1 - w_{T,lim}^2 \,. \tag{3.4.10}$$

However, the relations between maximal tangential load and amplitude differ slightly. With u_{lim} and equation (3.4.7) and equation (3.4.8), the maximal tangential forces read:

$$w \parallel f_T \Rightarrow f_T = f_{T,lim} = 1 - w_{lim} \,, \tag{3.4.11}$$

$$w \perp f_T \Rightarrow f_T = f_{T,lim} = 1 - 1.1 w_{lim} + 0.1 w_{lim}^3 \,. \tag{3.4.12}$$

The shakedown limits are depicted in Fig. 3.31. Experimentally, the maxima are identified by a stepwise increase of the amplitude, while the tangential force is kept constant,

see also section 5.1.4. The first amplitude for which the contact fails is identified as the shakedown limit. Thus, Fig. 3.31 shows w_{lim} as a function of $f_{T,lim}$. Again, experimental results are illustrated with triangles and error-bars and are only given for $w \perp f_T$. Experimental results for $w \parallel f_T$ are given in section 3.2. The theoretical values are represented by the blue line for $w \parallel f_T$ and by the red line for $w \perp f_T$. It shows that w_{lim} is slightly lower for $w \perp f_T$. However, the difference is in the range of the relative deviation. Additionally, Fig. 3.32 shows the maximum shakedown displacement u_{lim} as a function of $f_{T,lim}$. Experimental values are again only given for $w \perp f_T$, see section 3.2 for results of the parallel case. The experiment shows relatively good agreement with the theory, which is indicated by the red line for $w \perp f_T$ respectively the blue line for $w \parallel f_T$.

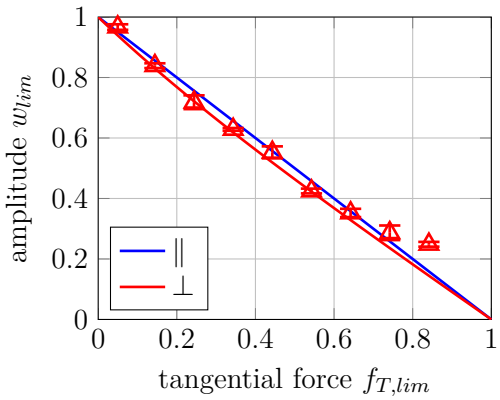

Fig. 3.31: maximal amplitude w_{lim} as a function of the maximal tangential force $f_{T,lim}$ for $w \parallel f_T$ and $w \perp f_T$. Triangles give the experimental results for $w \perp f_T$, solid lines gives the theoretical values of (3.4.11) and (3.4.12)

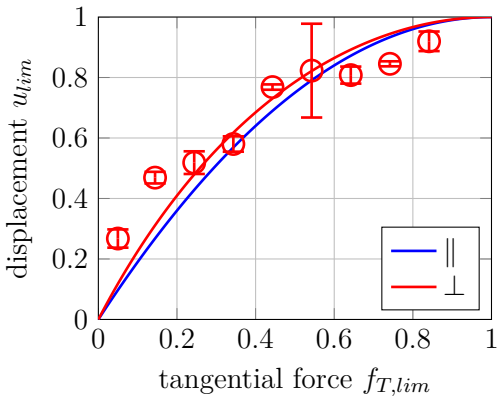

Fig. 3.32: maximal displacement u_{lim} as a function of the maximal tangential force $f_{T,lim}$ for $w \parallel f_T$ and $w \perp f_T$. Circles give the experimental results for $w \perp f_T$, solid lines gives the theoretical values of (3.4.9) and (3.4.10)

With the shakedown limits defined in equations (3.4.11) and (3.4.12), one can compute the maximal tangential force to achieve a safe shakedown for a given rolling amplitude and vice versa. In addition, one can determine the corresponding maximal displacement. The results show that shakedown is accompanied with a significant reduction of the loading capacity, as $f_{T,lim} \leq 1$ applies in both cases. Additionally, for the same amplitude, the parallel setting could theoretically bear slightly higher tangential load, but the difference is only minor. Thus, in force-locked connections with oscillations of this type, it might be more convenient if tangential loading and oscillation are aligned parallel.

3.4.3 Ratcheting for the Perpendicular Case

Once the shakedown limits are exceeded, the alternating slipping processes at the trailing edge will be continued with the rolling. In turn, the system does not reach a new

equilibrium and the contact fails. As shown in section 3.3, ratcheting occurs, where one side of the contact slips, while the other sticks. This accumulated slip leads to a rigid body motion [27]. Both, experiments and simulations show that the incremental slip Δu, i.e. the displacement per period, is an increasing function of f_T and w. As the difference for the two settings, parallel and perpendicular, is only minor, the same approximation function as in section 3.3 is used. The incremental displacement Δu for $w > w_{lim}$ is given as:

$$\Delta u = \eta \left(w - w_{\mathrm{lim}} \right) \ . \tag{3.4.13}$$

Again, it should be emphasized that w_{lim} also depends on f_T. The constant of proportionality η is a function of f_T, as shown in section 3.3. Adaption to the experimental results finally gives:

$$w \parallel f_T \Rightarrow \Delta u = \sqrt{2\left(1-(1-f_T)^{2/3}\right)}\left(w - w_{\mathrm{lim}} \right) \ , \tag{3.4.14}$$

$$w \perp f_T \Rightarrow \Delta u = \sqrt{5\left(1-(1-f_T)^{2/3}\right)}\left(w - w_{\mathrm{lim}} \right) \ , \tag{3.4.15}$$

where the goodness of the fits is shown in appendix A.1.3 in Tab. A.1.1. It turns out that the incremental displacement Δu is significantly higher for the perpendicular setting as could be seen in Fig. 3.33. Here, experimental results are symbolized by marks and error-bars and are only given for $w \perp f_T$. Dotted lines give equation (3.4.14) and the solid lines give equation (3.4.15). The ratcheting effect can be used for the generation of small displacement in case that an increase of the tangential loading is not possible or high accuracy is needed as in MEMS devices. The perpendicular setting is more convenient as for the same rolling amplitude and tangential force it generates a higher displacement.

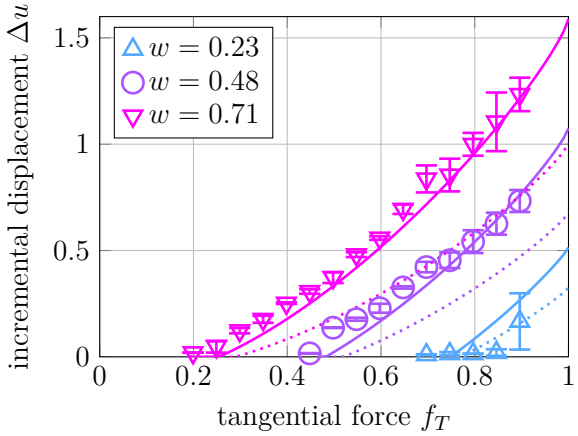

Fig. 3.33: incremental displacement Δu as a function of the tangential force f_T for different oscillation amplitudes w in case of ratcheting for $w \parallel f_T$ and $w \perp f_T$. Marks and error-bars give experimental results for $w \perp f_T$. Dotted lines give the theoretical values of (3.4.14) and solid lines those of (3.4.15)

3.5 Oscillating Cylindrical Rolling Contact

One important extension of the oscillating rolling contact are cylindrical systems, since such are often used in technical applications. Consider a tangentially loaded contact of a rigid cylindrical body of length L and an elastic substrate, as sketched in Fig. 3.34 (a). As before, the radius of the cylinder R and the elastic moduli E^* and G^* of the substrate, i.e. of the half-space, are effective quantities of two contacting bodies. Again, dry friction with constant μ, uncoupling displacements and a constant load regime F_N and F_T are assumed. According to the Hertz theory [52] a pressure distribution[8] is considered that is elliptic in the x, z-plane and constant in the y-direction:

$$p(x) = p_0 \left(1 - \left(\frac{x}{a}\right)^2\right)^{1/2} \quad \text{for} - a \leq x \leq a \; . \tag{3.5.1}$$

Here p_0 denotes the maximum pressure in the centre and a is the half width of the contact:

$$p_0 = \frac{2F_N}{\pi a L} \quad \text{and} \quad a = \sqrt{\frac{4RF_N}{\pi E^* L}} \; . \tag{3.5.2}$$

With $p(x)$ as in equation (3.5.1) the indentation depth of the cylinder d reads [89, 90]:

$$d = \frac{2F_N}{\pi E^* L} \left(\frac{1}{2}\left(1 + \ln(4)\right) + \ln\left(\frac{L}{a}\right)\right) \; . \tag{3.5.3}$$

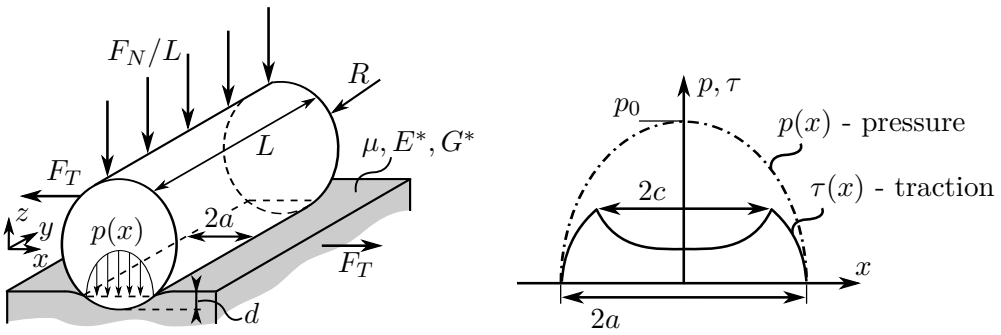

(a) cylindrical contact (b) pressure and traction

Fig. 3.34: (a) tangentially loaded contact of a rigid cylinder with radius R and length L and elastic half-space. (b) tangential contact with pressure $p(x)$ and traction distribution $\tau(x)$. Incipient sliding: contact width $2a$ and stick region with width $2c$ in the centre

The tangential problem was derived independently by Cattaneo [59] and Mindlin [60]. A good description of their procedure is given in [55] or [56]. Just as in the spherical case,

[8] In fact, the shape of the cylinder must rather slightly resemble to a barrel in order to achieve such a pressure distribution in a real system [89]. However, such a profile is very difficult to manufacture and correct only at the design load [52].

which is briefly described in section 2.1.1 and section 2.1.2, a tangential force insufficient to cause complete sliding, i.e. $F_T \leq F_{T,max} = \mu F_N$, will lead to slipping only at the boundary region of the contact area. The centre region $-c \leq x \leq c$ remains in a state of stick, where the half stick width reads:

$$c = a\left(1 - \frac{F_T}{\mu F_N}\right)^{1/2} . \tag{3.5.4}$$

To maintain this condition known as incipient sliding, the traction in the contact $\tau(x)$ must be a superposition of two elliptical traction distributions of the Hertzian type as in equation (3.5.1). In the complete contact region $-a \leq x \leq a$ applies the traction:

$$\tau_1(x) = \mu p_0 \left(1 - \left(\frac{x}{a}\right)^2\right)^{1/2} , \tag{3.5.5}$$

while in the sticking region $-c \leq x \leq c$ a second term is added:

$$\tau_2(x) = -\tau_0 \left(1 - \left(\frac{x}{c}\right)^2\right)^{1/2} . \tag{3.5.6}$$

The so called correctional term τ_0 reads:

$$\tau_0 = \mu p_0 \frac{c}{a} \tag{3.5.7}$$

and is given by the condition that the tangential displacement of particles must be constant in the sticking region. Finally the traction in the static case is distributed as sketched in Fig. 3.34 (b):

$$\begin{array}{lll} \tau(x) = \tau_1(x) + \tau_2(x) & \text{for} & 0 \leq |x| \leq c \ , \\ \tau(x) = \tau_1(x) & \text{for} & c < |x| \leq a \ . \end{array} \tag{3.5.8}$$

However, no exact solution is known for the tangential displacement of the substrate U_{stat}, one exception being elliptical contacts, where the displacements are expressed in terms of elliptical integrals [64, 91]. Even if the stress distribution is constant in the y-direction, the problem cannot be treated as being two-dimensional due to the following reason. In case of a two dimensional load, the displacement is decreasing logarithmically with r being the distance from the loaded surface [56]:

$$U_x \propto -k \ln\left(\frac{r}{r_0}\right) , \tag{3.5.9}$$

where k is the constant of proportionality. The constant r_0 is given by the condition that the displacement vanishes far away from the contact. Thus, the displacement in the centre of the contact depends on the choice r_0 and approaches infinity[9] for $r_0 \to \infty$. It is

[9] Prescott has likened the situation to a load applied to an infinitely long rod fixed at one end. The extension of such a rod caused by the application of any load would be infinite [90].

therefore necessary to treat the problem as fully three dimensional, even if the stress is constant in the y-direction. Again, the tangential displacement for a given traction $\tau(x)$ and contact area is in principle determined by the potential functions of Boussinesq and Cerruti [56]:

$$U_{stat} = U_x(0,0,0) = \frac{1}{\pi G}\int_{-\frac{L}{2}}^{\frac{L}{2}}\int_{0}^{c}\left(\frac{1-\nu}{s}+\frac{\nu\xi^2}{s^3}\right)(\tau_1(\xi,\eta)+\tau_2(\xi,\eta))\,\mathrm{d}\xi\mathrm{d}\eta$$
$$+\frac{1}{\pi G}\int_{-\frac{L}{2}}^{\frac{L}{2}}\int_{c}^{a}\left(\frac{1-\nu}{s}+\frac{\nu\xi^2}{s^3}\right)\tau_1(\xi,\eta)\,\mathrm{d}\xi\mathrm{d}\eta\,. \tag{3.5.10}$$

with G and ν as equation (2.1.12) and s as in equation (2.1.5). Using equation (3.5.2) and (3.5.4) and the traction as in equations (3.5.5)-(3.5.8) one can conduct a numerical integration[10] of equation (3.5.10). Finally, curve fitting gives an approximation for the tangential displacement:

$$U_{stat} = U_0\left(1-\left(1-\frac{F_T}{\mu F_N}\right)\right)^{0.92}. \tag{3.5.11}$$

Here, U_0 denotes the maximum displacement for $F_T = \mu F_N$, which is also an approximation based on the indentation depth of equation (3.5.3):

$$U_0 = \mu\frac{2F_N}{\pi E^* L}\left(\frac{1}{2}(1+\ln(4))+\ln\left(1.8\frac{E^*}{G^*}\frac{L}{a}\right)\right). \tag{3.5.12}$$

Again, the goodness of the fits is given in appendix A.1.3 in Tab. A.1.1.

3.5.1 Influence of the Oscillating Rolling

As for the spherical case, the static tangential contact is superposed by a slight oscillatory rolling of the cylinder. Again, the amplitude W denotes the lateral movement of the centre of the cylinder, as depicted in Fig. 3.35. Likewise, the overall macroscopic normal and tangential forces are kept constant in magnitude and the rolling corresponds to a rocking of the contacting bodies. The parameters of influence and the displacement are normalized as:

$$f_T = \frac{F_T}{\mu F_N}, \quad w = \frac{W}{a}, \quad u = \frac{U}{U_0}\,, \tag{3.5.13}$$

where a refers to equation (3.5.2) and U_0 is the maximal static displacement as stated in equation (3.5.12). Again, tangential forces below the maximum holding force and oscillation amplitudes smaller than the half contact width are assumed:

$$f_T \leq 1 \quad \text{and} \quad w \leq 1\,. \tag{3.5.14}$$

[10] Even as both, integration limits and integrand, are known and several advanced symbolic mathematical software was used, it was unfortunately not possible to find a closed form solution.

Thus, taken by itself, neither of the two factors leads to a failure of the contact, exactly as in the spherical case.

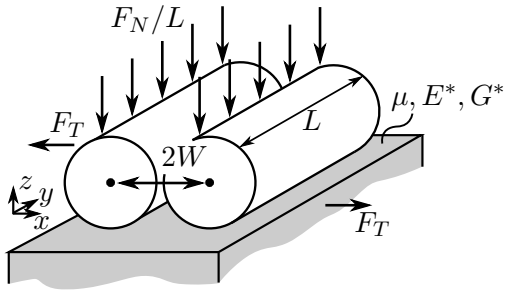

Fig. 3.35: oscillating rolling contact of a rigid cylinder and an elastic half-space. The centre of the cylinder rolls with amplitude W and the macroscopic forces are constant. This corresponds to a rocking of the of the upper body

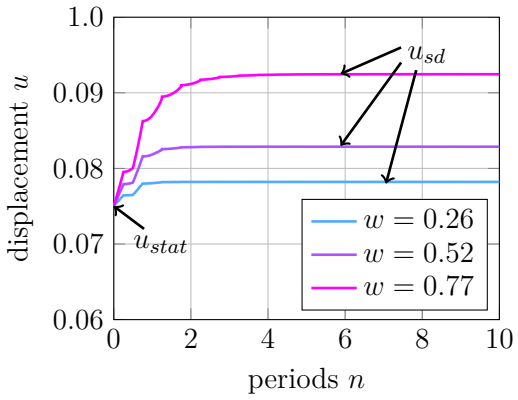

Fig. 3.36: displacement u for different oscillation amplitudes w and $f_T = 0.08$. Shakedown: displacement stops and system reaches a new equilibrium

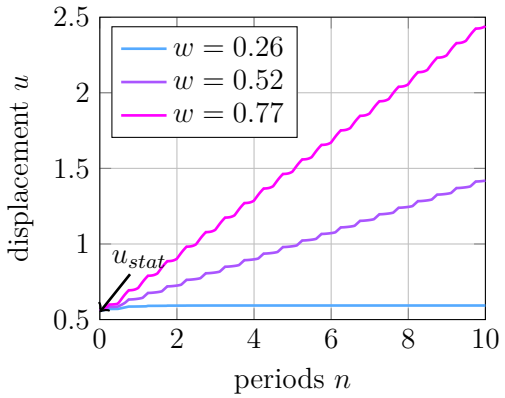

Fig. 3.37: displacement u for different oscillation amplitudes w and $f_T = 0.58$. Ratcheting: displacement continues

Figures 3.36 and 3.37 give the displacement of the substrate u for different amplitudes w. It is computed using the CONTACT model, see also appendix B.2. The parameters of the experimental rig as in section 5.1.3 in Tab. 5.1.3 are used. The displacement corresponds to the rigid body displacement between remote points within the cylinder and the substrate as the sum of the elastic displacement and the accumulated shift per time step. As one expects, the system response is equivalent to the oscillating contact with spherical rolling body. In combination with the constant macroscopic load, the rolling leads to an increased rigid body displacement in relation to the static value. Figure 3.36 shows that the displacement stops after a few periods and the contact holds, even if the rolling continues. The system reaches a new equilibrium and the according displacement corresponds to the constant time independent shakedown displacement u_{sd}

[25]. For this effect to occur, f_T and w must fall below the shakedown limits, otherwise the contact fails. As for the sphere, the accumulated shift per time step leads to a continuing displacement, as depicted in 3.37. This is referred to as frictional ratcheting or walking [27, 28, 29].

3.5.2 Contact Configuration after Shakedown

The system starts in equilibrium and the entire contact sticks. When the cylinder starts rolling, the pressure drops at the actual trailing edge and increases at the leading edge. In the reversal points the pressure is distributed as in Fig. 3.38 (a):

$$p\left(x\right) = p_0 \left(1 - \left(\frac{x \mp W}{a}\right)^2\right)^{1/2} \quad \text{for } -a \pm W \leq x \leq a \pm W \ . \tag{3.5.15}$$

This causes slipping at the trailing edge, while at the leading edge the traction initially remains constant. The resulting imbalance in the tangential direction increases the rigid body displacement between cylinder and substrate u within every back and forth movement. For sufficiently small f_T and w, shakedown occurs and a saturation level is reached after a certain number of periods, as shown in Fig. 3.36.

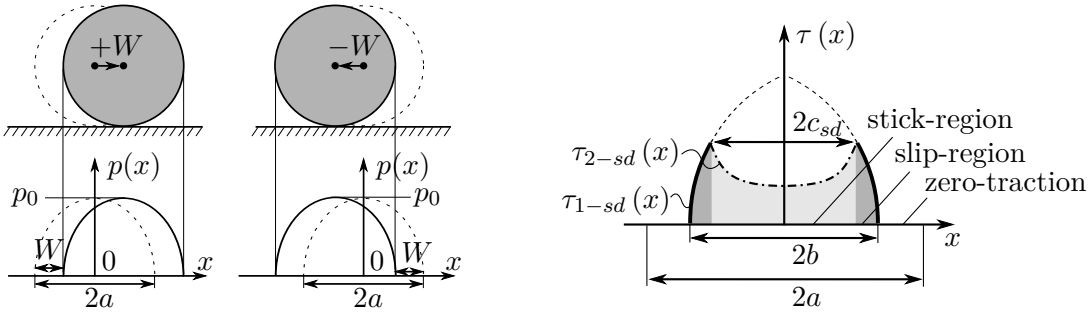

(a) pressure distribution (b) traction distribution

Fig. 3.38: (a) pressure distribution $p\left(x\right)$ and contact region in the reversal points, caused by the oscillatory rolling. (b) traction distribution $\tau\left(x\right)$ and contact regions (stick-region, slip-region, zero-traction) after shakedown

In the new equilibrium, there remain three characteristic contact widths, as depicted in Fig. 3.38 (b). Firstly, in the centre region, the displacement must be constant because of the sticking condition (stick region). Secondly, adjacent thereto occurs a region, where the tangential stress equals the traction bound (slip region). Thirdly, at the outside of the contact, the cylinder is periodically released and the tangential traction is zero (zero traction). In summary this gives:

$$\begin{aligned} \text{stick-region:} \quad & 0 \leq |x| \leq c_{sd} \quad \Rightarrow U_x = \text{const.} \ , \\ \text{slip-region:} \quad & c_{sd} < |x| \leq b \quad \Rightarrow \tau = \mu p \ , \\ \text{zero-traction:} \quad & b < |x| \leq a \quad \Rightarrow \tau = 0 \ . \end{aligned} \tag{3.5.16}$$

Here c_{sd} denotes the half stick width and for b applies $b = a - W$. In order to deduce the traction distribution, the slip region is considered firstly. In this region the traction $\tau(x)$ must equal the friction coefficient times the minimal pressure distribution, that appears at the reversal points of the oscillation, as stated in equation (3.5.15):

$$\tau_{1-sd}(x) = \mu p_0 \left(1 - \left(\frac{x+W}{a}\right)^2\right)^{1/2} \quad \text{for } c_{sd} < |x| \leq b \,. \tag{3.5.17}$$

In contrast to the static case, the traction in the centre region will be from a different type as this region is neither released nor slipping at any time. However, one can proceed in the Cattaneo [59] and Mindlin [60] manner and can propose that the traction in the stick region is again a superposition of two Hertzian distributions:

$$\tau_{2-sd}(x) = \tau_{21}\left(1 - \left(\frac{x}{b}\right)^2\right)^{1/2} - \tau_{22}\left(1 - \left(\frac{x}{c_{sd}}\right)^2\right)^{1/2} \quad \text{for } 0 \leq |x| \leq c_{sd} \,. \tag{3.5.18}$$

Each of these tractions causes a parabolic tangential displacement [92] of particles in the centre region. The total displacement is a superposition of the individual displacements:

$$U_x(x) = C_1 - \frac{\tau_{21}}{bE^*}x^2 + C_2 + \frac{\tau_{22}}{c_{sd}E^*}x^2 \tag{3.5.19}$$

that must be constant in the stick region in accordance to the no slip condition. Figure 3.39 gives the displacement U_x in the entire contact. It is computed using the CONTACT model. The sticking condition yields:

$$\varepsilon_{xx}(x) = \frac{\partial U_x}{\partial x} = 0 \Rightarrow \tau_{22} = \tau_{21}\frac{c_{sd}}{b} \,. \tag{3.5.20}$$

Further, the traction must be continuous at the edge of the sticking region $x = c_{sd}$. With equations (3.5.17), (3.5.18) and (3.5.20) this gives

$$\tau_{1-sd}(x = c_{sd}) = \tau_{2-sd}(x = c_{sd}) \Rightarrow \tau_{21} = \frac{\mu p_0 \left(1 - \left(\frac{c_{sd}+W}{a}\right)^2\right)^{1/2}}{\left(1 - \left(\frac{c_{sd}}{b}\right)^2\right)^{1/2}} \,. \tag{3.5.21}$$

Finally, the complete traction $\tau(x)$ after shakedown is distributed as in Fig. 3.38 (b):

$$\begin{aligned} \text{stick-region:} \quad & 0 \leq x \leq c_{sd} && \Rightarrow \tau(x) = \tau_{2-sd}(x) \,, \\ \text{slip-region:} \quad & c_{sd} < x \leq b && \Rightarrow \tau(x) = \tau_{1-sd}(x) \,, \\ \text{zero-traction:} \quad & b < x \leq a && \Rightarrow \tau(x) = 0 \,. \end{aligned} \tag{3.5.22}$$

It must be noted that c_{sd} is still unknown. After shakedown, the integral of the traction over the contact width $\mathcal{L}_c = 2a$ must match the tangential loading per length:

$$\frac{F_T}{L} = \int_{\mathcal{L}_c} \tau(x)\mathrm{d}x = 2\int_0^{c_{sd}} \tau_{2-sd}(x)\mathrm{d}x + 2\int_{c_{sd}}^{b} \tau_{1-sd}(x)\mathrm{d}x \,. \tag{3.5.23}$$

With equations (3.5.17), (3.5.18), (3.5.20) and (3.5.21) this gives:

$$f_T = \frac{2}{\pi}\arccos\left(\frac{c_{sd}}{a}+w\right) + \frac{2}{\pi}\left(1-\left(\frac{c_{sd}}{a}+w\right)^2\right)^{1/2}\left(\frac{b}{a}\frac{\arcsin\left(\frac{c_{sd}}{b}\right)-\left(\frac{c_{sd}}{b}\right)^2\frac{\pi}{2}}{\left(1-\left(\frac{c_{sd}}{b}\right)^2\right)^{1/2}}-w\right) . \tag{3.5.24}$$

Using numerical solving procedures this transcendent equation gives the unknown stick radius c_{sd} for different f_T and w. The results are depicted in Fig. 3.40. For a mutual verification c_{sd} is also computed using the CONTACT model. Lines depict the results using equation (3.5.24) and marks depict the results gained via simulation. Both solutions show strong agreement. As one expects, the half stick-width decreases if f_T and w are increased.

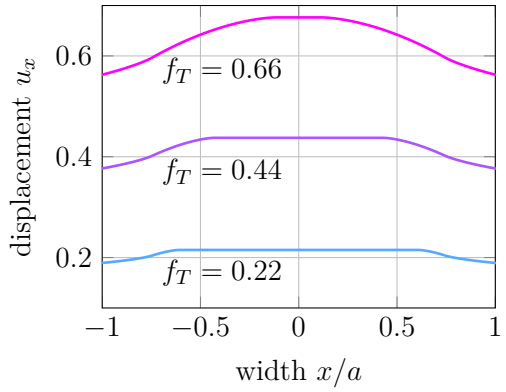

Fig. 3.39: tangential displacement of particles u_x for different f_T and $w = 0.26$ computed with CONTACT model. Displacement is constant in the centre

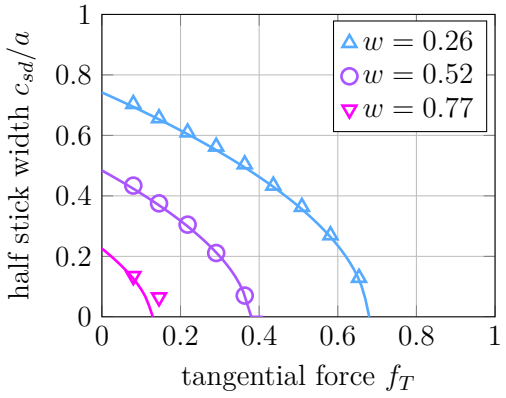

Fig. 3.40: half stick width c_{sd} after shakedown as a function of f_T for different w computed with (3.5.24) (solid lines) and CONTACT model (marks)

With these results, it is now possible to compute the missing traction constants τ_{21} and τ_{22} and thus $\tau(x)$. Again, the simulation is used for a mutual verification. The traction distribution for different f_T is shown in Fig. 3.41. Here, the dashed lines show the CONTACT solution, whereas the analytical expression is denoted by the solid lines and just given for one half of the symmetrical contact. Both solutions show strong agreement. As one can see, the stick region decreases and the maximal traction increases with f_T. Since w is not changed, the slip radius b is constant for all forces considered. Figure 3.42 depicts the traction for different amplitudes w. Higher amplitudes decrease the stick region and increase the periodically released area, i.e. the zero traction region. Additionally, the magnitude of the remaining traction is amplified. This is because the remaining area with non-zero traction decreases at a constant tangential force. This illustrates the shakedown effect, where the residual force in the contact must be sufficiently strong to withstand the tangential load and to prevent any further sliding [25].

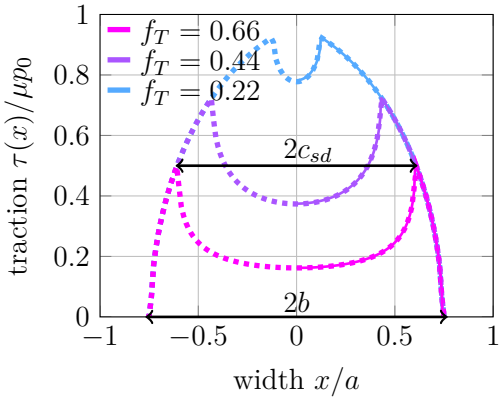

Fig. 3.41: normalized tangential traction distribution $\tau(x)$ after shakedown for $w = 0.26$ and different f_T

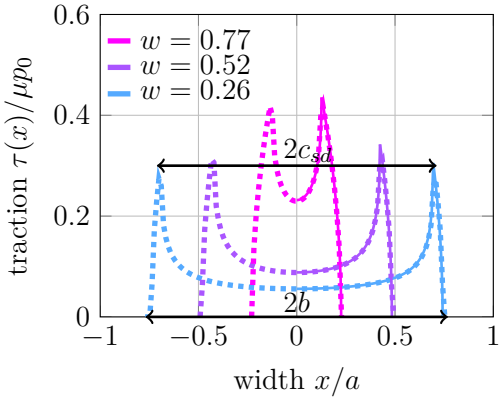

Fig. 3.42: normalized tangential traction distribution $\tau(x)$ after shakedown for $f_T = 0.08$ and different w

3.5.3 Shakedown of the Cylindrical Rolling Contact

With the traction after shakedown being known, it is possible to compute the according tangential displacement of the substrate u_{sd}. Again, the potential functions of Boussinesq and Cerruti for symmetric $\tau(x)$ [56] are used:

$$U_{sd} = U_x(0,0,0) = \frac{1}{\pi G}\int_{-\frac{L}{2}}^{\frac{L}{2}}\int_{0}^{c_{sd}}\left(\frac{1-\nu}{s}+\frac{\nu\xi^2}{s^3}\right)\tau_{2-sd}(\xi,\eta)\,\mathrm{d}\xi\mathrm{d}\eta$$
$$+\frac{1}{\pi G}\int_{-\frac{L}{2}}^{\frac{L}{2}}\int_{c_{sd}}^{b}\left(\frac{1-\nu}{s}+\frac{\nu\xi^2}{s^3}\right)\tau_{1-sd}(\xi,\eta)\,\mathrm{d}\xi\mathrm{d}\eta\,, \tag{3.5.25}$$

where G and ν and s are as in equation (2.1.12). However, since the exact solution for the half stick width c_{sd} remains unknown, it is not possible to give a closed-form solution for equation (3.5.25). Instead, equation (3.5.24) is used to compute c_{sd} for different f_T and w. Subsequently, the results are inserted into equation (3.5.25) and numerical integration procedures are used to get U_{sd}. Finally, curve fitting tools are used to compute an approximation for the normalized displacement as a function of f_T and w:

$$u_{sd} = 1-(1-f_T)^{0.92}+0.3f_Tw\,. \tag{3.5.26}$$

The goodness of the fit is given in appendix A.1.3 in Tab. A.1.1. The shakedown displacement for different f_T and w is given in Fig. 3.43. Solid lines give the results using equation (3.5.26) and asterisks give the CONTACT simulation results. Error-bars and marks indicate the experimental results. As for the sphere u_{sd} is increased in comparison

to the according static value u_{stat}. It shows that the bandwidth of the displacements is narrower than for the spherical contacts.

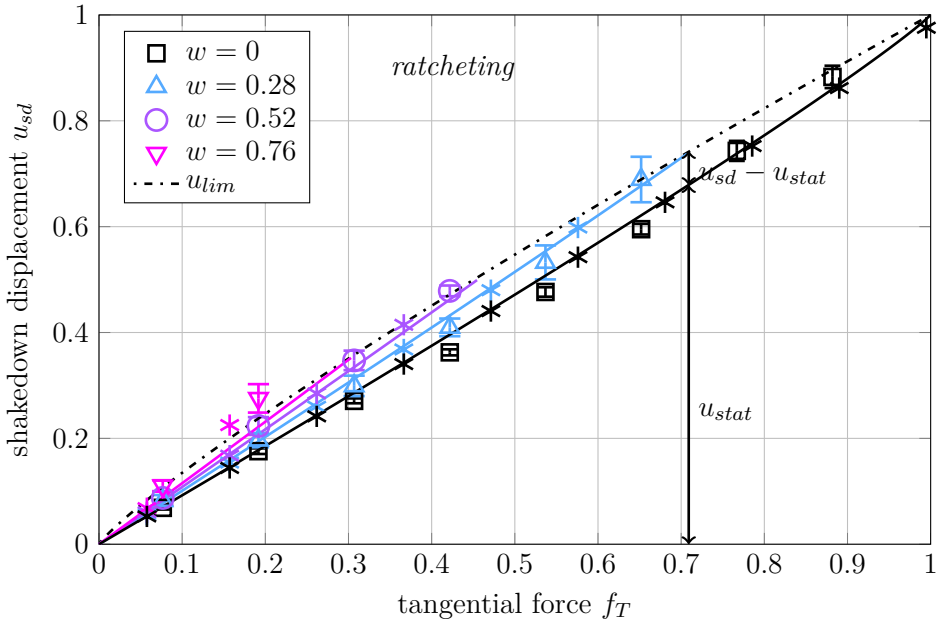

Fig. 3.43: shakedown displacement u_{sd} as a function of the tangential force f_T for different oscillation amplitudes w in case of a cylindrical roller. Solid lines give theoretical result (3.5.26). The oscillatory rolling increases the displacement by comparison with its static value u_{stat}

The dash-dot line shows the maximal displacement u_{lim} that is reached before complete sliding occurs and the contact fails. If so, the stick width c_{sd} goes to zero. In combination with equation (3.5.24) this gives the exact analytical relation between maximal tangential load $f_{T,lim}$ and maximal amplitude w_{lim}:

$$f_{T,\mathrm{lim}} = \frac{2}{\pi}\left(\arccos\left(w_{\mathrm{lim}}\right) - w_{\mathrm{lim}}\left(1-\left(w_{\mathrm{lim}}\right)^2\right)^{1/2}\right) \ . \tag{3.5.27}$$

Curve fitting again gives approximations for the inverse relation:

$$w_{\mathrm{lim}} = 1 - f_{T,\mathrm{lim}}^{0.73} \ , \tag{3.5.28}$$

as well as for the maximum displacement, see appendix A.1.3 and Tab. A.1.1:

$$u_{\mathrm{lim}} = f_{T,\mathrm{lim}}^{0.87} \ . \tag{3.5.29}$$

The equations (3.5.27) and (3.5.28) enable to specify the highest possible amplitude to maintain a safe shakedown for a given tangential force and vice versa. Again, the CONTACT model is used for verification. Starting points are rather small amplitudes that are increased stepwise until ratcheting occurs. Fig. 3.44 depicts the maximum amplitude

as a function of the tangential force. Equation (3.5.28) is symbolized by the solid line. Triangles give the simulation results, where upward pointing ones depict the last shakedown amplitude (sd) and downward pointing ones depict the first ratcheting amplitude (rt). Also experimentally, the maxima are identified by a stepwise increase of w, see section 5.1.4 for a description of the experimental procedures. The results are shown by asterisks (exp) and error-bars. The deviations between equation (3.5.28) and the experiments are relatively high. The good agreement with the numerical values indicates a faulty experiment. One explanation for this might be a deviation of the actual pressure distribution from the assumed cylindrical one, as discussed in section 5.1.5. Besides, the determination of the maximal amplitude is not straight forward but relatively artificial as described in section 5.1.4. Figure 3.45 shows the according maximum displacements. Formula (3.5.29) (solid line), simulation (triangles) and experiment (asterisks and error-bars) are in good agreement.

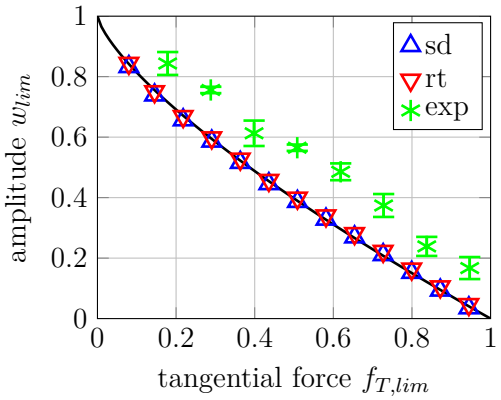

Fig. 3.44: maximal amplitude w_{lim} as a function of the tangential force $f_{T,lim}$. Solid lines give (3.5.28)

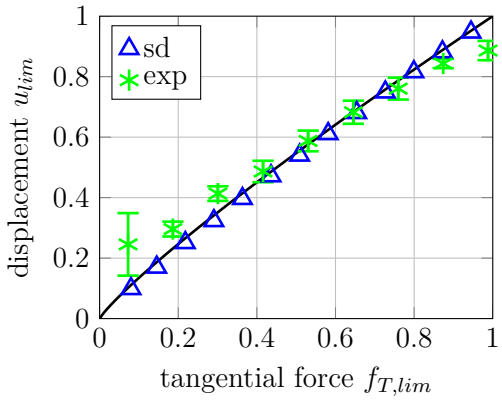

Fig. 3.45: maximal displacement u_{lim} as a function of the tangential force $f_{T,lim}$. Solid lines give (3.5.29)

3.5.4 Ratcheting of the Cylindrical Rolling Contact

As for the sphere, ratcheting occurs if the shakedown limits stated in equations (3.5.27) and (3.5.28) are exceeded. Slip occurs on the actual trailing edge of the contact that accumulates to a continuing rigid body motion. The incremental slip per period Δu for different f_T and w is given in Fig. 3.46. The solid lines show the approximation function:

$$\Delta u = 0.64 f_T \left(w - w_{\text{lim}}\right) \ , \tag{3.5.30}$$

which is computed using a linear regression wtih u_{stat} being the regressor, see details in appendix A.1.3 in Tab. A.1.1. For this purpose the CONTACT model is used to increase the number of data points. The obtained coefficient is then adjusted to the experimental data. Except for low amplitudes w experiment and equation (3.5.30) are in good agreement. It shows that Δu is lower for the cylindrical contact than for the spherical ones, where the incremental displacement is given in Fig. 3.33.

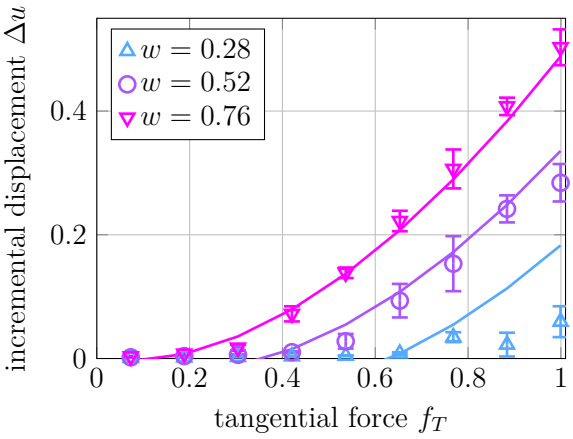

Fig. 3.46: incremental displacement Δu as a function of the tangential force f_T for different oscillation amplitudes w in case of ratcheting. Marks and error-bars give experimental results, solid lines gives the theoretical value of (3.5.30)

3.6 Summary

As generic models for force-locked connections under the influence of vibrations, oscillating rolling contacts between spherical and cylindrical rollers and a flat substrate have been introduced. Basic assumptions are a constant load regime F_T and F_N, dry friction of the Coulomb type with a constant μ and linear elastic material behaviour. Additionally, the systems are assumed to be quasi-static and from an uncoupled type, i.e. Dundur's constant $\beta = 0$, meaning that variations in the normal force will not induce any tangential displacement and vice versa.
It shows that slight oscillatory rolling of the roller varies the pressure distribution and the contact region within every cycle. In turn, this leads to partial slip and macroscopic rigid body displacement of the substrate. Depending on both, oscillation amplitude w and tangential loading $f_{T,lim}$, the displacement stops after a few periods or continues. The former case is referred to as shakedown and the latter as ratcheting. The exact shakedown limits for both, oscillation amplitude and tangential load for the three cases considered have been derived: spherical roller with parallel and perpendicular alignment of load and oscillation and cylindrical roller with parallel alignment. In all three cases it turns out that shakedown is accompanied with a significant reduction of the tangential load capacity, which is approximately:

$$f_{T,lim} \approx 1 - w_{lim} \; . \tag{3.6.1}$$

In addition, using the results one can predict the rigid body motion for the shakedown case and the incremental slip in case of ratcheting. The comparison of experiment and theory shows that the method of dimensionality reduction (MDR) has proven to be a suitable instrument for the modelling of oscillating rolling contacts.

Chapter 4

Dynamic Influences on Sliding Friction

System dynamics is a crucial factor for the macroscopic frictional resistance of dynamic systems [5, 9, 45]. In the following chapter an explanation for the underlying effects is proposed and a theoretical model is introduced that captures the basic mechanisms. A non-dimensional form of the governing equations of motion is derived and the non-dimensional parameters are identified. In the next step numerical simulation is used to determine the parameter range that enables to induce a significant reduction of the frictional resistance. Finally, the theoretical outcomes are compared with experimental results. Taken together, it shows that characteristic self-excited oscillations with vibrations in the normal direction can lead to an almost vanishing frictional resistance.

4.1 The Micro-Walking Machine

A potential basic system that captures important dynamic effects that enable a significant reduction of the apparent frictional resistance could be as follows. Assume an elastic specimen which is pressed on a rigid substrate by the macroscopic normal force F_N. In the tangential directional direction it is additionally loaded with the macroscopic tangential force F_T, such that it slides with a constant velocity v_0 like in Fig. 4.1 (a).

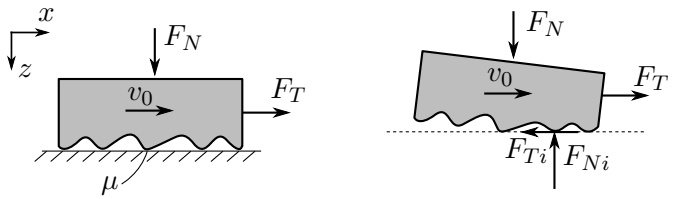

(a) elastic specimen (b) free body diagram

Fig. 4.1: basic model for the micro-walking effect. (a) elastic specimen moving on a rigid substrate with constant velocity v_0. (b) free body diagram in rotated position with contact forces of contact spot i

As in real contacts, specimen and substrate will not touch over the entire apparent contact surface but in several small contact zones [3]. Each contact zone will exhibit its own stress distribution in the normal and tangential direction which is represented by a normal and a tangential force F_{Ni} and F_{Ti} as depicted in Fig. 4.1 (b). Only the case of dry friction is considered and it is assumed that Coulomb's law with a constant coefficient $\mu_s = \mu_k = \mu$ applies in the contact spots. Thus, any distinction between static and kinetic friction and the variation of the latter with sliding speed are neglected, as discussed in section 2.3.3. The coefficient μ reflects all microscopic influences of the surface that depend on the material pairing. According to the local sticking condition a specific spot sticks, whenever:

$$|F_{Ti}| \leq \mu F_{Ni} \ . \tag{4.1.1}$$

Otherwise, the contact spot slips and is subjected to a local resistance force:

$$F_{Ri} = \mu F_{Ni} \ . \tag{4.1.2}$$

Due to the kinematic coupling between the normal and tangential translation and the rotation of the rigid body, the forces in the contact spots will vary in time. This effect significantly influences the apparent frictional resistance [10, 45] as will be explained in the following. Assuming that there are overall n similarly loaded contact spots in the system, one can define the theoretical average normal force acting in one contact spot:

$$\bar{F}_{Ni} = \frac{F_N}{n} \ . \tag{4.1.3}$$

Due to the elasticity of the specimen, the actual status of a specific contact spot, i.e. sticking or slipping, is independent from the actual status of the rigid body. Thus, the rigid body can move in the tangential direction while a single spot is sticking. In addition, the distance between the spots is assumed to be sufficiently large so that the spots are independent. The relative displacement between substrate and bulk body therefore only changes the elastic deformation in the vicinity of a sticking spot and a slipping spot simply moves along with the bulk body. Under these assumptions the system will be able to micro-walk on the substrate. In this case micro-walking describes a particular behaviour of the contact spots:

- a contact spot only slips whenever its actual normal force F_{Ni} falls below $\bar{F}_{Ni}$
- a contact spot sticks whenever its actual normal force F_{Ni} exceeds $\bar{F}_{Ni}$

As a result, the average resistance force of contact spots $\bar{F}_{Ri} = \langle F_{Ri} \rangle$, where $\langle . \rangle$ denotes the time average, falls below the expected value calculated with (4.1.2) and (4.1.3):

$$\bar{F}_{Ri} < \mu \bar{F}_{Ni} \ . \tag{4.1.4}$$

In consequence, the overall resistance force of the system, which is the sum over all of the n contact spots, will fall below the overall theoretical value as well:

$$F_R = \sum_{i=1}^{n} \bar{F}_{Ri} < \sum_{i=1}^{n} \mu \bar{F}_{Ni} = \mu F_N \ . \tag{4.1.5}$$

This leads to the definition of the effective coefficient of friction μ_e:

$$\mu_e = \frac{F_R}{\mu F_N} \leq 1 \ . \tag{4.1.6}$$

There is a strong analogy to the ratcheting case described in section 3.3, where one side of a single contact slips while the other sticks [27]. The micro-slip accumulates to a rigid body motion. Hence, ratcheting decreases the tangential load that is needed for gross sliding, i.e. decreases the effective static and kinetic friction.
An experimental analogy of the dynamic mechanism of friction reduction is given by the work of Tolstoi [39]. In this case, increasing sliding speed increases the normal oscillations of the sliding body. Due to the non-linearity between indentation and normal force, see section 2.1.1, the vibrations of the slider are highly asymmetric. Consequently, an increase of the normal oscillation amplitude decreases the mean value of indentation and the contact radius of the contact spots during sliding. As a result, the friction force decreases as well [93, 10]. The micro-walking machine extends this concept, as it also includes the spatial variation of normal and tangential forces and stick and slip zones.

4.1.1 Discrete Model

The simplest implementation of a system that captures the aforementioned effects is a plane specimen that has only two contact spots at the edges, as depicted in Fig. 4.2 (a). The specimen is unloaded in the normal direction except for the force of gravity mg of the bulk body. Here m denotes the mass of the specimen and g is the gravitational acceleration. The tangential force F_T is applied by a constantly moving base, that is connected via a spring with stiffness k_s. As the base moves with constant velocity v_0, the mean velocity of the specimen $\bar{v}$ exactly corresponds to v_0. This type of excitation models a nominally steady motion of the system. Thus, any vibrations that may occur are not directly caused by the excitation but rather by self-excited oscillations.
The separation of space scales principle as is introduced in section 2.3.1 is used for a further simplification. According to this, the space scales contributing to the elastic and kinetic energy of a mechanical system with friction can be separated in the following way [65]:

- The elastic energy is a *local* quantity which only depends on the conditions in the contact region
- The kinetic energy is a *non-local* quantity which can be assumed to equal to the kinetic energy of the rigid bulk as a whole

This enables a further simplification, such that there remains a rigid body with mass m, moment of inertia θ, height $2a$ and length $2b$ that consists of two elastic contact spots as shown in Fig. 4.2 (b). These spots are modelled as linear springs with normal stiffness k_z and tangential stiffness k_x as described in section 2.3.3. The stiffness can be approximated as [55]:

$$k_z = E^* D_c \quad \text{and} \quad k_x = G^* D_c \ . \tag{4.1.7}$$

Here E^* and G^* denote the effective elastic modules, that are a function of the shear modulus G and Poisson's ratio ν of the elastic specimen [55]:

$$E^* = \frac{2G}{1-\nu} \quad \text{and} \quad G^* = \frac{4G}{2-\nu} \,. \tag{4.1.8}$$

The contact diameter D_c depends on the instantaneous contact configuration and is estimated as shown in section 5.2.1. The deflections of the springs in the normal and tangential direction U_{zi} and U_{xi} depend on the actual state of motion of the rigid body, i.e. they are a function of x, z and φ. These deflections represent the elastic deformations of the specimen in the normal and tangential direction. This can be illustrated as follows. Considering Fig. 4.3 (a) it shows that the change of position of a point on the rigid body P to P' causes deformations that are concentrated in the vicinity of the contact spots in a volume with linear dimensions of the order of the contact width D_c [65]. As shown in Fig. 4.3 (b), in the theoretical model this effect is considered by the spring deflections. The system is also assumed to be decoupled as introduced in section 2.1.3. Thus, a change in U_z does not change U_x and vice versa[1]. Consequently, the contact forces acting on the rigid body are given as:

$$F_{N1/2} = k_z U_{z1/2} \quad \text{and} \quad F_{T1/2} = k_x U_{x1/2} \,, \tag{4.1.9}$$

where the subscript $(.)_{1/2}$ denotes the two contact spots as shown in Fig. 4.2 (b). Finally, in the simplified model, there remain only three degrees of freedom: X and Z, which describe the lateral and the vertical translation of the centre of gravity of the specimen, and Φ, which describes the rotation of the rigid body. In addition, there are two dependent variables for each contact spot: the spring deflections $U_{z1/2}$ and $U_{x1/2}$. Still, the moving base acts as the only external excitation, where h denotes its lever arm with respect to the centre of gravity. This configuration allows the lever arm to be larger than the height a, as examined in section 4.2.3.

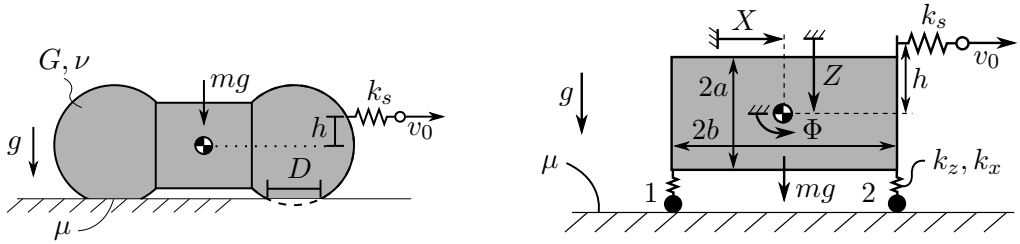

(a) specimen (b) simplified system

Fig. 4.2: (a) elastic specimen consisting of two spherical shaped edges pulled by a constantly moving base. (b) simplified rigid body model with three degrees of freedom and linear springs to model the contact spots

[1]Nevertheless, the deflections are coupled through the equations of motion of the system.

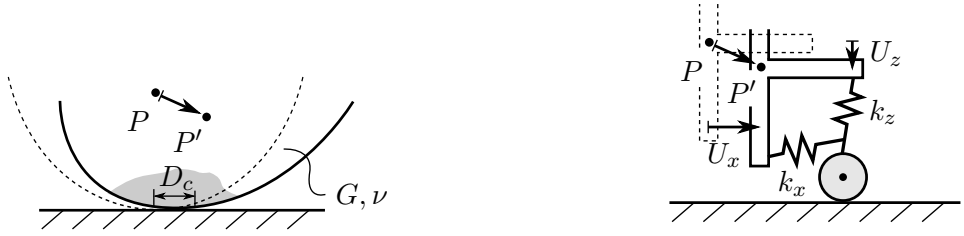

(a) contact spot (b) linear spring

Fig. 4.3: (a) elastic contact spot, where deformations are concentrated in a volume with linear dimensions of the order of the contact width D_c. (b) spring element with normal stiffness k_z and tangential stiffness k_x and corresponding deflections U_z and U_x. The dotted lines show the old positions of the rigid bodies

There is an analogy to the model proposed by Martins et al. which consists of a rigid block that exhibits the same degrees of freedom, i.e. translation and rotation [10]. In the normal direction the rigid block is as well only subjected to its own weight. And in the tangential direction it is restrained by a spring and a viscous damper (dash-pot) and subjected to a moving belt. Also the interface friction is modelled assuming Coulomb dry friction with contact stiffness in the normal and tangential direction. This enables to compare the results. However, their stress distribution in the contact surface is a directly determined function of the rigid body motion and does not enable parts of the contact to slip, while others stick as in the model introduced here. Thus, on the one hand the present model is an extension of the model proposed by Martins et al. which also takes into account the spatial variation of stick and slip zones. On the other hand, the non-linearity of the interface response [10] is neglected.
Again it should be emphasized that this work considers the known basic mechanisms that are responsible for the experimentally observed dependency of the frictional resistance on the system dynamics. These are essentially vibrations in the normal direction [39, 40, 93, 43] and coupling effects between normal, tangential and rotational degrees of freedom [10, 44, 45]. In the present model, a rotation of the body Φ, i.e. a pitching motion, leads to varying normal and tangential spring deflections $U_{z1/2}$ and $U_{x1/2}$ and therefore forces at both contacts. The other way round, this asymmetry acts as a twisting moment on the rotation. Thus, an appropriate synchronization of these motions will enable the system to walk in such a way as explained in the beginning of this chapter. The questions remain, under which conditions the excitation of the constantly moving base can cause self-excited oscillations of the rigid body and whether these oscillations will be synchronized in the proposed manner.

4.1.2 Parameters of Influence

The initial model is described by eleven dimensionful parameters. According to the so called Π-theorem [94] the number of parameters can be reduced introducing a non-dimensional representation of the governing equations. Therefore the displacements and

deflections are normalized with the geometrical constants a and b:

$$x = \frac{X}{b},\ z = \frac{Z}{b},\ \varphi = \frac{a}{b}\Phi,\ u_{z1/2} = \frac{U_{z1/2}}{b},\ u_{x1/2} = \frac{U_{x1/2}}{b}\ . \tag{4.1.10}$$

In addition, the characteristic period τ and the dimensionless time t are introduced:

$$\tau = \sqrt{\frac{m}{k_x}}\ \Rightarrow\ t = \frac{t_{dim}}{\tau}\ , \tag{4.1.11}$$

where t_{dim} denotes the dimensionful time. This yields the accelerations as:

$$\ddot{X} = \frac{\mathrm{d}^2 X}{\mathrm{d}t_{dim}^2} = b\frac{\mathrm{d}^2 x}{\mathrm{d}\left(t\tau\right)^2} = \frac{k_x b}{m}\frac{\mathrm{d}^2 x}{\mathrm{d}t^2} = \frac{k_x b}{m}x''\ , \tag{4.1.12}$$

$$\ddot{Z} = \frac{k_x b}{m}z''\ , \tag{4.1.13}$$

$$\ddot{\Phi} = \frac{k_x b}{ma}\varphi''\ , \tag{4.1.14}$$

where $(.)'$ denotes the derivation with respect to the non-dimensional time t. This procedure reduces the number of parameters from eleven to eight, the remaining ones being listed in Tab. 4.1.1. Considering the analogy to the model of Martins et al. [10] the parameter κ_1 corresponds to their stiffness parameter s_M that takes into account the ratio of the stiffness of the base spring and the normal contact stiffness. In addition parameter κ_3 is equivalent to their ratio of height and width h_M. Finally, the microscopic friction μ resembles to their more sophisticated friction parameter f_M. Despite the differences between the two models this enables to compare the overall trend of the influences of the parameters in the following sections.

Tab. 4.1.1: definitions and interpretation of the remaining parameters of the non-dimensional system

parameter	definition	physical interpretation
κ_1	$\frac{k_s}{k_x}$	ratio of macro and micro stiffness
κ_2	$\frac{k_z}{k_x}$	ratio of normal and tangential contact stiffness
κ_3	$\frac{a}{b}$	geometry ratio, slenderness of the rigid body
κ_4	$\frac{mg}{k_x b}$	ratio of normal force and contact stiffness times half width
κ_5	μ	microscopic friction
κ_6	$\frac{v_0}{b}\sqrt{\frac{m}{k_x}}$	velocity dependent non-dimensional parameter
κ_7	$\frac{\Theta}{mb^2}$	ratio of rotational inertia of the rigid body
κ_8	$\frac{h}{a}$	ratio of the lever arm of the excitation

4.1.3 Modelling and Simulation

Figure 4.4 depicts the free-body diagram of the micro-walking machine in a deflected position. In the non-dimensional form of the system, the deflections of the springs correspond to the contact forces:

$$f_{N1/2} = \kappa_2 u_{z1/2} \quad \text{and} \quad f_{T1/2} = u_{x1/2} \ , \tag{4.1.15}$$

where the subscript $(.)_{1/2}$ again denotes the two contact spots. Depending on the instantaneous motion, the contact spots might be in contact or be released from the substrate as shown Fig. 4.4. Here, the left contact (1) is fully released, what will lead to zero contact forces. In case that a spring is in contact, the spots can slip or stick, depending whether the instantaneous friction bound is exceeded or not. These many options are taken into account numerically using a case distinction of the equations of motion as shown in section 2.3.3. A detailed description of the procedures in pseudo-code-notation is also given in appendix B.4.

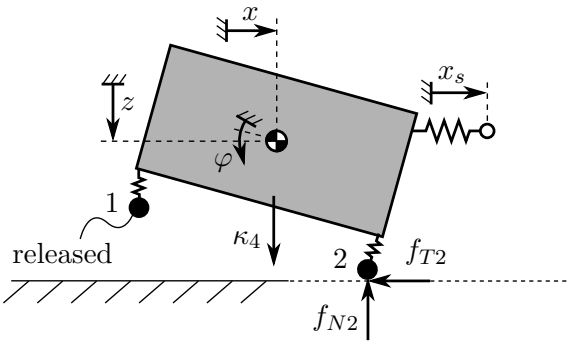

Fig. 4.4: free body diagram of the non-dimensional system, where x_s denotes the displacement of the base. Due to the rotation, the left contact is released from the substrate

Assuming small rotations, i.e. $\varphi \ll 1$, and the springs to be undeflected for $x, z, \varphi = 0$, Newton's second law [95] yields the equations of motion (EoM) for the system depicted in Fig. 4.4 as:

$$x_s' = \kappa_6 \ , \tag{4.1.16}$$

$$x'' = -u_{x1} - u_{x2} + \kappa_1 \left(x_s - x + \kappa_8 \varphi\right) \ , \tag{4.1.17}$$

$$z'' = -\kappa_2 u_{z1} - \kappa_2 u_{z2} + \kappa_4 \ , \tag{4.1.18}$$

$$\begin{aligned} \varphi'' = {} & \frac{1}{\kappa_7} \left(-\kappa_2 \kappa_3 u_{z1} \left(1 - \varphi\right) + \kappa_2 \kappa_3 u_{z2} \left(1 + \varphi\right) - u_{x1} \left(\kappa_3^2 + \varphi\right) - u_{x2} \left(\kappa_3^2 - \varphi\right)\right) \\ & - \frac{1}{\kappa_7} \left(\kappa_1 \left(\kappa_3^2 \kappa_8 + \varphi\right) \left(x_s - x + \kappa_8 \varphi\right)\right) \ . \end{aligned} \tag{4.1.19}$$

Equation (4.1.16) is the result of introducing a new variable $x_s = \kappa_6 \Delta t$, what removes the time dependency and enhances the computation [96]. The motion of the system is computed using a stepwise numerical integration scheme. The basic principle may be

explained with reference to the simple Euler method [97]. According to this, for a given derivative $\dot{y} = f(y,t)$ and the initial value $y(t)$ the solution in the next step $y(t+\Delta t)$ can be approximated as:

$$y(t+\Delta t) = y(t) + \Delta t f(y,t) \ , \tag{4.1.20}$$

where Δt denotes the time step. The so called Velocity-Verlet algorithm is used to determine the motion of the system from equations (4.1.16) - (4.1.19), where a detailed description of the scheme is given in Appendix B.3. The algorithm is widely used in molecular dynamics (MD) to compute the motion of molecules on basis of Newton's second law. In MD the forces acting on a molecule in time $t+\Delta t$ are given by a potential, i.e. they are a function of the position of the molecule at time $t+\Delta t$. In the same way the state of motion of the system x, z and φ in the time step $t+\Delta t$ is computed firstly. The normal and tangential spring deflections $u_{z1/2}$ and $u_{x1/2}$ at time $t+\Delta t$, i.e. the contact forces, are computed afterwards as described in Appendix B.4. These determine the velocities at time $t+\Delta t$ that in turn determine the state of motion in time-step $t+2\Delta t$ and so on.

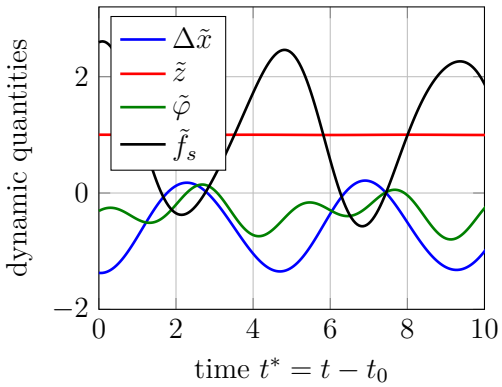

Fig. 4.5: steady state motion for parameter set A. All quantities are normalized as $\Delta\tilde{x} = (x - x_s)/\mu\kappa_4$, $\tilde{z} = z/z_{stat}$, $\tilde{\varphi} = \varphi/\mu\kappa_3\kappa_4$ and $\tilde{f}_s = f_s/\mu\kappa_4$

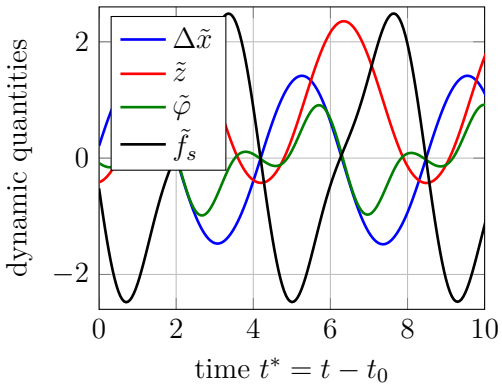

Fig. 4.6: steady state motion for parameter set B. All quantities are normalized as $\Delta\tilde{x} = (x - x_s)/\mu\kappa_4$, $\tilde{z} = z/z_{stat}$, $\tilde{\varphi} = \varphi/\mu\kappa_3\kappa_4$ and $\tilde{f}_s = f_s/\mu\kappa_4$

Using the numerical integration procedures described in appendix B.3, the motion of the system in steady state, i.e. $x(t), z(t)$ and $\varphi(t)$, as well as the spring force $f_s(t)$ are determined for various sets of parameters. The initial condition are as follows:

$$\begin{aligned} x(0) &= 0 \ , & x'(0) &= 0 \ , \\ z(0) &= z_{stat} \ , & z'(0) &= 0 \ , \\ \varphi(0) &= 0 \ , & \varphi'(0) &= 0 \ , \\ x_s(0) &= 0 \ , \end{aligned} \tag{4.1.21}$$

where z_{stat} denotes the static displacement yielded with equations (4.1.18) and (B.4.1)

from appendix B.4:

$$z'' = 0 \Rightarrow z_{stat} = \frac{\kappa_4}{2\kappa_2} \ . \tag{4.1.22}$$

In order to determine the frictional resistance the spring force f_s is computed as:

$$f_s(t) = \kappa_1 \left(x_s(t) - x(t) + \kappa_8 \varphi(t) \right) \ . \tag{4.1.23}$$

This excitation force corresponds to the macroscopic resistance force of the overall system. Finally, with $\langle . \rangle$ being the time average, the effective coefficient of friction is computed as:

$$\mu_e = \frac{\langle f_s(t) \rangle}{\mu \kappa_4} \ . \tag{4.1.24}$$

Figures 4.5 and 4.6 depict the normalized steady state motion for two parameter sets as a function of time $t^* = t - t_0$. Here t_0 indicates a time at which the transient process is already completed. The two sets of parameters are as follows:

$$\text{set A:} \quad \kappa_{1-8} = \left(2, 1.2, 0.5, 10^{-4}, 0.5, 10^{-4}, 0.42, 0.5\right) \ , \tag{4.1.25}$$

$$\text{set B:} \quad \kappa_{1-8} = \left(2, 1.2, 0.5, 10^{-4}, 0.68, 10^{-4}, 0.42, 1.18\right) \ . \tag{4.1.26}$$

Despite the fact that the parameter sets only differ slightly, i.e. $\mu = 0.5$ and $\kappa_8 = 0.5$ for set A versus $\mu = 0.68$ and $\kappa_8 = 1.18$ for set B, the steady state motion of the system differs strongly. This becomes clearer considering the vertical displacement z that is represented by the red lines in Fig. 4.5 and Fig. 4.6. For set A applies $z = const.$, whereas for set B z follows an harmonic oscillation. A more detailed analysis of the influence of the different parameters is given in the following section 4.2.

4.2 System Dynamics and Frictional Resistance

Using the simulation model as described in section 4.1 appropriate parameter ranges of κ_{1-8} are identified that lead to a reduction of the effective frictional resistance μ_e. This is followed by a more detailed analysis in order to identify the parameter combination necessary for a (theoretical) maximal reduction. The experimental setting that is described in section 5.2 is designed such that it matches this parameter combination as closely as possible.

4.2.1 Influence of the Parameters

The non-dimensional model is described by eight parameters, each of it potentially influencing the motion and in turn the effective frictional resistance of the system. Starting point is the determination of appropriate basic points of the parameter space. These are described in the following.

The ratio of the base-spring stiffness and the contact stiffness κ_1 can be interpreted as a measure for the stiffness of the system. Hence, high values correspond to a stiff tribological system such as a disc brake. One example for a soft system is a pin-on disc tribometer with flexible arm. The range of κ_1 is assumed to be:

$$\kappa_1 = \frac{k_s}{k_x} \Rightarrow \kappa_1 \in \left[10^{-1}, 10\right] \ . \tag{4.2.1}$$

The ratio κ_2 depends on the contact geometry. A narrow bandwidth is considered:

$$\kappa_2 = \frac{k_z}{k_x} \Rightarrow \kappa_2 \in [1, 1.4] \ . \tag{4.2.2}$$

Parameter κ_3 denotes the ratio of height and width of the rigid body, i.e. the slenderness. Medium values are considered:

$$\kappa_3 = \frac{a}{b} \Rightarrow \kappa_3 \in [0.5, 1.5] \ . \tag{4.2.3}$$

Parameter κ_4 lacks an illustrative physical meaning. However, one can estimate it assuming a specimen of mass $m = 100$ g and half-width $b = 1$ cm and a tangential contact stiffness of $k_x \in [10^4, 10^5]$ N/m (see section 5.2.1):

$$\kappa_4 = \frac{mg}{k_x b} \Rightarrow \kappa_4 \in \left[10^{-4}, 10^{-2}\right] \ . \tag{4.2.4}$$

In this first step, medium values of the microscopic coefficient of friction are assumed:

$$\mu \in [0.2, 0.6] \ . \tag{4.2.5}$$

The parameter κ_6 depends inter alia on the speed of the constantly moving base v_0. Assuming a velocity range of $v_0 \in [1, 100]$ mm/s it results to:

$$\kappa_6 = \frac{v_0}{b}\sqrt{\frac{m}{k_x}} \Rightarrow \kappa_6 \in \left[10^{-4}, 10^{-2}\right] \ . \tag{4.2.6}$$

Assuming a rectangular shape of the rigid body and taking into account[2] (4.2.3), the ratio of the rotational inertia results to:

$$\kappa_7 = \frac{\Theta}{mb^2} = \frac{4}{12}\left(1 + \kappa_3^2\right) \Rightarrow \kappa_7 \in [0.5, 1.5] \ . \tag{4.2.7}$$

Finally, κ_8 denotes the ratio of the lever arm and the height. Allowing the spring to be applied underneath the centre of gravity, the range of κ_8 results to:

$$\kappa_8 = \frac{h}{a} \Rightarrow \kappa_8 \in [-0.8, 0.8] \ . \tag{4.2.8}$$

[2]It is important to emphasize that κ_7 is an independent parameter and is not influenced by κ_3, as the exact shape of the rigid body might differ from the rectangular shape.

Following a straightforward approach one would for instance analyse ten different values for each parameter. This would result in 10^8 different parameter combinations. Consequently, given the computation time for one combination of approximately 90 s, this would finally require an overall computation time of 300 years if one uses a standard PC and simulate one combination after the other. To avoid this, the so called design of experiments (DoE) approach is used, which is introduced in detail at appendix A.2. This method systematically minimizes the effort needed for a sufficiently accurate analysis. A so-called full-factorial experimental schedule is used that considers all possible basic points in parameter space. Thus, three values of each parameter (minimum, intermediate, maximum) are taken and the motion of the system in steady state is computed to give the effective coefficient of friction. Overall, this leads to $3^8 = 6561$ different combinations. In order to enhance the overall computation time, the calculation is performed in parallel on a graphics processing unit (GPU). Using a Geforce GTX 560 GPU and a step size of $\Delta t = 1 \cdot 10^{-3}$ the whole calculation takes about 15 min for a non-dimensional period of observation of $T = 4000$. Finally, the main effect is calculated, which is the mean of all $6561/3 = 2187$ combinations in which one specific parameter is held constant. The so called interaction effect, which describes the interaction between different parameters, is not considered here, since the high number of combinations preclude a meaningful evaluation. For computation of the main effect only solutions without tilting of the specimen are considered, see also section 4.2.2. For this purpose, solutions with high rotational amplitudes are excluded from the evaluation. Figure 4.7 depicts the main effect on the effective coefficient of friction μ_e. The overall influence of factors is rather low, as the maximal reduction is in the range of 10 %.

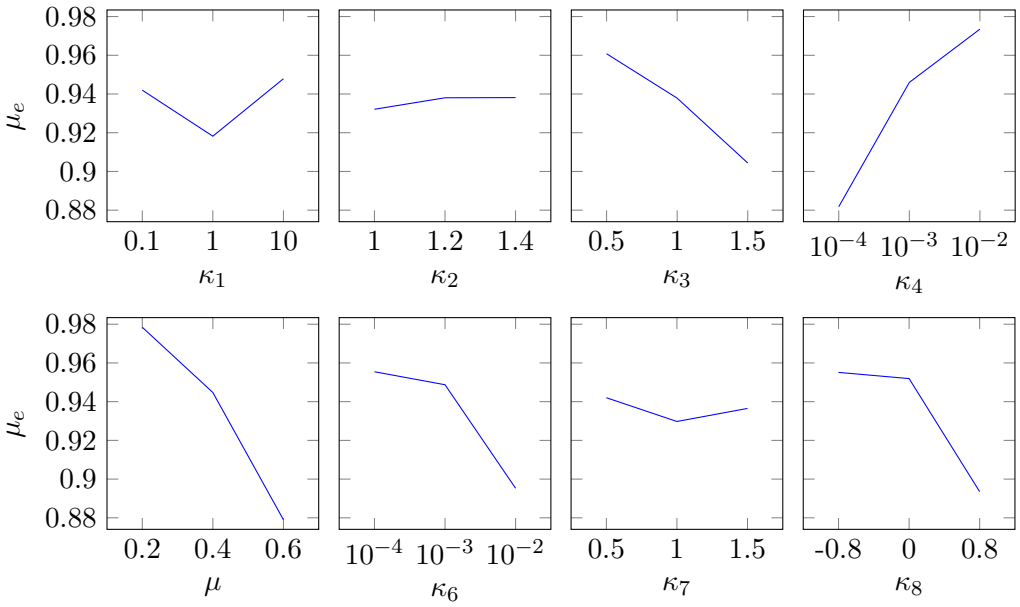

Fig. 4.7: main effect-plot of the eight parameters of influence κ_{1-8} on the effective coefficient of friction μ_e

On the one hand, this may mean that the individual influence of all parameters is low and there do not exist any points in the parameter space that lead to a strong reduction. On the other hand, this may indicate that only a few parameters are from great influence, whereas the majority has almost no influence. Thus, a strong reduction would only occur in a few points in parameter space. In this work the DoE analysis rather serves as a tool for the identification of convenient parameter combinations. Despite the fact that a further analysis is given later in section 4.2.2 and section 4.2.3, the results are briefly interpreted. However, it must emphasized that the results of the DoE should be considered with caution, as the overall effect is rather low.
More specifically, it turns out that μ_e is low for κ_1 around 1, meaning that a similarity of the excitation and contact stiffness is convenient. This resembles to the model of Martins et al. in which a large stiffness parameter s_M or a small s_M combined with a large damping lead to an apparently smooth sliding with an effective coefficient of friction lower than the static one [10]. The ratio κ_2 has a low influence. In contrast, κ_3 is from great influence indicating that a more compact shape of the rigid body decreases μ_e. A higher κ_3 leads to a higher rotational moment of the spring force f_s in comparison to the contact forces. Conversely, the friction increases with increasing κ_4. Thus, low ratio of mass and contact stiffness reduces the effective friction in this system. The influence of the microscopic friction μ is relatively high, where μ_e decreases with increasing μ. This effect is consistent with the beam model by Adams [47] and can be explained by an increasing interplay of the tangential forces and the rotational moment that leads to self-excited oscillations. The friction also decreases for increasing κ_6 indicating that the effective friction decreases with increasing velocity. This effect also occurs in the slip wave model of Adams [50] and in the rigid body model of Martins et al. [10]. In addition, the effect of decreasing friction with increasing velocity was experienced in numerous experiments [77, 78, 79] where an overview is given for example in [9]. The influence of κ_7, which depends on the rotational inertia, is relatively poor. In contrast, the lever arm of the base, which is represented by κ_8, is from great influence. The effective friction decreases with increasing lever arm, thus with an increasing moment of the spring force f_s with respect to the contact spots. This increases the coupling between the rotational moment and the friction forces and is consistent with the beam model [47].
In addition, the main effect on the minimal vertical amplitude in steady state z_{min}/z_{stat} is computed as given in Fig. 4.8. Here z_{stat} is the static displacement as defined in (4.1.22). It shows that the amplitudes are negative and reach values of -100. A negative z_{min} indicates jumping of the rigid body, i.e. a total release of the contact spots. In addition, a high magnitude of z_{min} indicates instabilities and self-excited oscillations of the rigid body in the normal direction that are caused by the interplay of the friction force and the rotational moment. However, it should again be emphasized that the high magnitudes can indicate two scenarios. Namely, a small number of parameters combinations can exhibit very high corresponding magnitudes while the remaining combinations exhibit no jumping at all. Or a large number of parameter combinations can exhibit similarly high amplitudes. In both cases, jumping must not necessarily occur in all combinations.

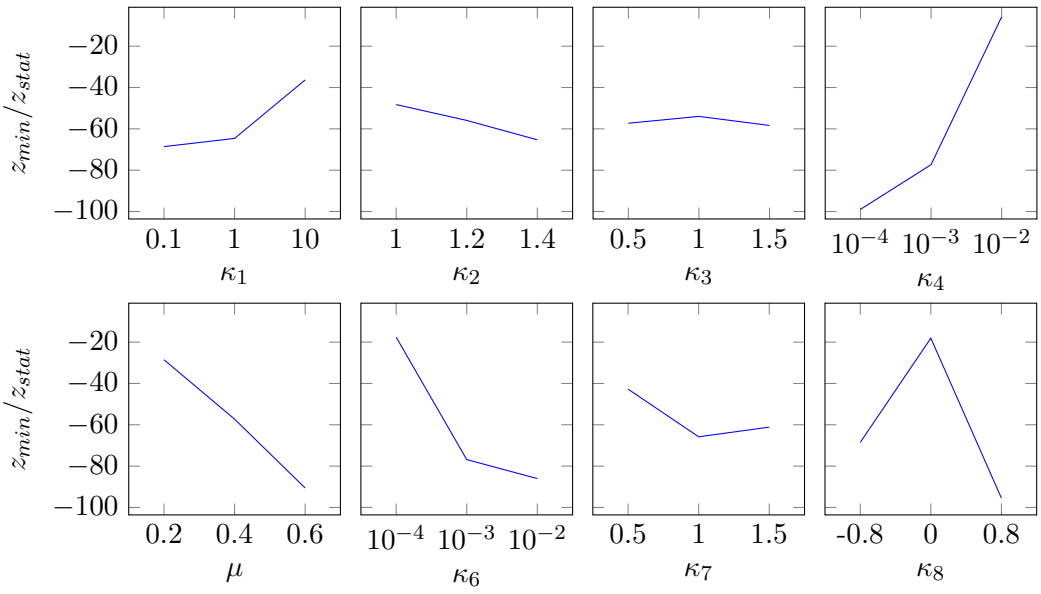

Fig. 4.8: main effect-plot of the eight parameters of influence κ_{1-8} on the vertical minimal amplitude z_{min}/z_{stat}

In detail, it shows that κ_2, κ_3 and κ_7 all have a weak effect on the vertical amplitude. The absolute value increases with decreasing κ_1, what shows that the vertical motion is stronger, the weaker the guidance of the spring. Decreasing κ_4 strongly increases the magnitude of z_{min}. Thus, a heavier specimen jumps less strongly for the same contact stiffness and width b. The magnitudes of z_{min} strongly increase with μ. This may be explained with the effect that a higher friction increases the coupling between lateral and vertical translation and rotation, what leads to higher displacements in the vertical direction. This is again consistent with the Adams beam model where increasing μ leads to increasing instabilities [47]. The same effect occurs in the Martins et al. model, where the normal displacement increases with the friction parameter f_M [10]. Parameter κ_6 has a strong effect, indicating that a higher velocity generates higher vertical jumps. One can assume that a higher velocity simply increases the kinetic energy of the system that is then transferred to the vertical motion through the coupling effect. In addition, it shows that the vertical amplitudes are weak for $\kappa_8 = 0$.

Taken together, the DoE analysis shows that a relatively narrow parameter range needs to be matched in order to induce a reduction. Especially for the parameters κ_4, μ and κ_6 the reduction is accompanied with an increasing amplitude of the oscillation in the vertical direction. Again it should be emphasized that the DoE analysis is used to determine parameter combinations that enable a significant reduction. It is not the intention to give a detailed analysis at this point. However, the results are consistent with those found in the literature.

4.2.2 Reduction of the Frictional Resistance

In the following some of the parameters are kept constant for a more detailed analysis. The results of section 4.2.1 show that a significant reduction requires κ_1 (macroscopic stiffness) around 1 and low values of κ_4 (normal force vs. contact stiffness times half width). In addition, the influence of κ_2 and κ_7 is relatively poor and high values of κ_6 lead to a strong amplification of the vertical amplitudes. These and the parameter κ_3 are kept fixed, where the exact values are listed in Tab. 4.2.1. A low value for κ_6 is chosen in order to induce only small vertical amplitudes in the range of the static displacement z_{stat}. This maintains the microscopic character of the walking effect. The remaining parameters are the microscopic friction μ and the position of the lever arm κ_8. According to the DoE analysis, both have a significant influence on the efficient friction. In addition κ_8 is relatively easy to vary in real experiments and the influence of μ was already examined by other authors [10, 47] what gives the possibility for comparison.

Tab. 4.2.1: parameters that are constant in the detailed parameter study

parameter	κ_1	κ_2	κ_3	κ_4	κ_6	κ_7
value	2	1.2	0.5	10^{-4}	10^{-4}	0.42

A parameter study for 1600 combinations of the two remaining factors is conducted. Again, the influence on the effective friction μ_e is examined, which is shown in Fig. 4.9. In addition, the influence on the minimal vertical amplitude of the motion of the centre of gravity of the specimen is examined, which is shown in Fig. 4.10. In both figures occur three characteristic parameter ranges, namely the *no effect-range*, the *reduction range* and the *critical range*. These can be explained as follows.

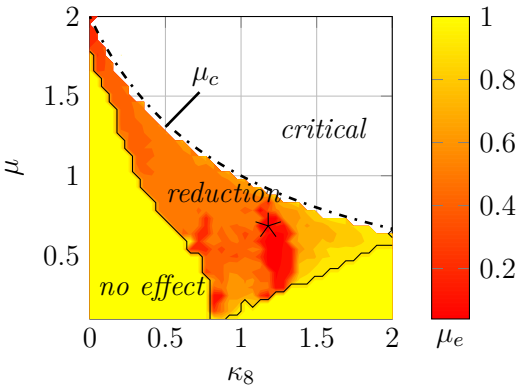

Fig. 4.9: parameter study of κ_8 and μ for the effective coefficient μ_e. The star denotes the maximal reduction of 98 %. The dash-dot line gives μ_c of (4.2.13)

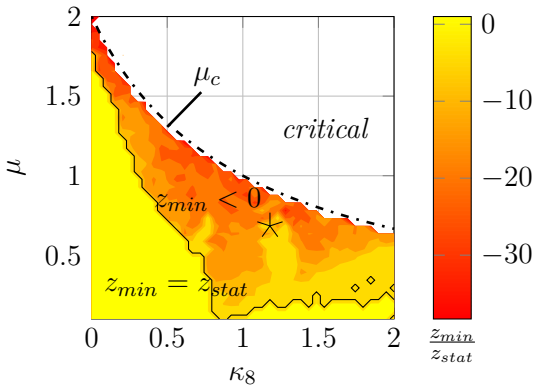

Fig. 4.10: parameter study of κ_8 and μ for the minimal amplitude z_{min}/z_{stat}. In the reduction range applies $z_{min} < 0$. The dash-dot line gives μ_c of (4.2.13)

No Effect Range Here no reduction of the macroscopic frictional resistance occurs at all, i.e. $\mu_e = 1$. This range is indicated by the solid line in Fig. 4.9. The comparison of Fig. 4.9 and Fig. 4.10 shows that this parameter range coincides with a region of low vertical amplitudes or even of no vertical vibrations at all. The region of constant vertical displacement is delimited by the solid line in Fig. 4.10. This indicates that vertical vibrations play an important role in the reduction effect. Without vertical vibration, no reduction occurs at all. This is consistent with the known experiments of Tolstoi et al. [39, 40, 93].

Critical Range The reason of the critical behaviour of the system is caused by a tilting of the rigid body over spot 2. It is indicated by the white regions in Fig. 4.9 and Fig. 4.10. The simulation is stopped in this case, because the model as stated in (4.1.16) - (4.1.19) is no longer valid as the magnitudes of φ no longer permit linearization of the trigonometric functions. In order to give an explanation for this effect the dimensionful system as depicted in Fig. 4.2 (b) is used. Consider a tilted position of the rigid body such that contact 1 is completely released. This is situation is sketched in Fig. 4.11 where a free body diagram is given. The only forces acting on the rigid body are the spring force F_s, the force of gravity mg and the forces in the right contact 2.

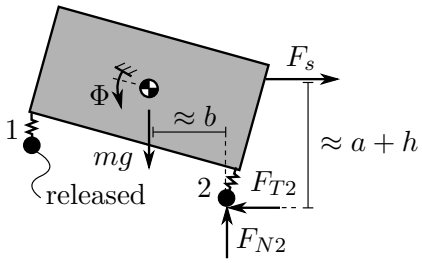

Fig. 4.11: free body diagram of the system in a tilted position

Using the principle of angular momentum with respect to contact 2 and assuming small rotations, i.e. $\Phi \ll 1$, gives:

$$\Theta^{(2)}\ddot{\Phi} = -F_s\,(h+a) + mgb\,. \tag{4.2.9}$$

A further tilting in the clockwise direction requires a negative angular acceleration $\ddot{\Phi} < 0$, what yields:

$$F_s\,(h+a) > mgb\,. \tag{4.2.10}$$

Assuming sliding of spot 2 and a constant velocity v_0, the spring force F_s must match the tangential force F_{T2}. In turn, F_{T2} corresponds to the actual friction bound, i.e. $F_{T2} = \mu F_{N2}$. Given the free body diagram of Fig. 4.11 and the assumption $\ddot{Z} = 0$ the spring force in the tilting state results to:

$$F_s = F_{T2} = \mu F_{N2} = \mu mg\,. \tag{4.2.11}$$

Inserting this into (4.2.10) gives the condition for the coefficient of friction for which the rigid body tilts over spot 2:

$$\mu > \frac{mgb}{mg\,(h+a)} = \frac{b}{(h+a)}\ . \tag{4.2.12}$$

Finally, using the definition of the non-dimensional parameters as listed in Tab. 4.1.1, the non-dimensional form of the critical coefficient μ_c for the limiting case yields:

$$\mu_c = \frac{1}{\kappa_3\,(1+\kappa_8)}\ . \tag{4.2.13}$$

Relation (4.2.13) is denoted by the dash-dot line in Fig. 4.9 and Fig. 4.10 and is in good agreement with the simulation results. Within the critical limit, the rotational amplitudes where small, i.e. $\varphi < 1 \cdot 10^{-3}$. A similar type of critical system behaviour was also studied by Martins et al. for their sliding block model. In this, the maximum value $\bar{f}_M$ of the friction parameter f_M was chosen such that steady sliding equilibrium ceases to be possible due to tumbling of the block [10]. The case $\kappa_3 = 1$ and $\kappa_8 = 1$ exactly corresponds to the case $\bar{f}_M = 1/h_M$, where h_M is the ratio of height and length of the block. They conclude that no one would run a comparable experiment allowing for the occurrence of such large oscillations. However, they point out that the same may not be true for instance in a pin-on-disk tribometer having very flexible arms and a small contact region.

Reduction Range For a specific range of parameters occurs a significant reduction of μ_e over 50 %. The comparison of Fig. 4.9 and Fig. 4.10 shows that the reduction coincides with negative vertical amplitude z_{min}. This indicates that a total release of the contact spots, i.e. jumping, is an important prerequisite for a reduction in this system. Thus, one reason for the reduction are oscillations of the rigid body in the vertical direction. This is consistent with the well-known experiments of Tolstoi et al. [39, 40, 93] and with theoretical works [10, 41, 42, 47]. However, the amplitudes are of the order of the static vertical displacement. Hence, in a real system these vibrations are from a microscopic character and can be superposed unnoticed to an apparently smooth sliding motion. The maximal reduction of 98% is denoted by the star and occurs at $\kappa_8 = 1.18$ and $\mu = 0.68$. The corresponding minimum amplitude is $z_{min}/z_{stat} = -0.42$.

For a further analysis, the relative stick time of the contact spots is computed, which is the ratio of the time a specific contact sticks $T_{s1/2}$ and the period of observation T:

$$t_{s1/2} = \frac{T_{s1/2}}{T}\ . \tag{4.2.14}$$

The stick times are depicted in Fig. 4.12 and Fig. 4.13.

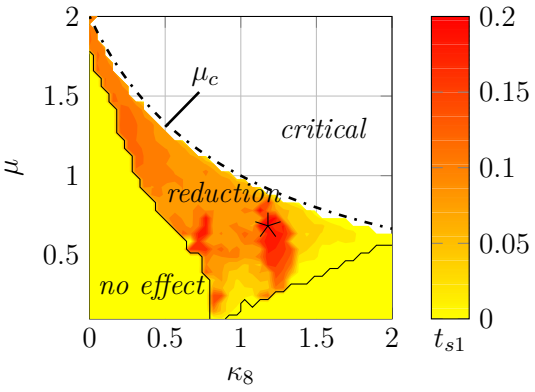

Fig. 4.12: parameter study of κ_8 and μ for the relative stick time t_{s1} of contact 1. In the reduction range applies $t_{s1} \approx 15\%$

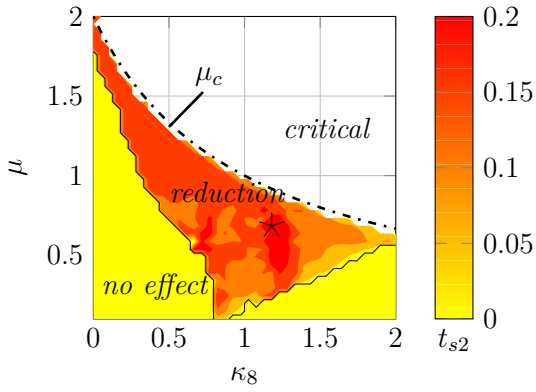

Fig. 4.13: parameter study of κ_8 and μ for the relative stick time t_{s2} of contact 2. In the reduction range applies $t_{s2} \approx 20\%$

It shows that sticking coincides with the reduction with $t_{s1} \approx 15\%$ and $t_{s2} \approx 20\%$ in the reduction range. In contrast, no sticking occurs in the no effect range. Thus, sticking is important for the reduction. There are three explanations for this. Firstly, sticking leads to storage of elastic energy in the contacts. This energy is needed for the jumping that occurs in the reduction range, as shown in Fig. 4.10. Secondly, the concept of micro-walking implies that only one spot is sticking, while the other one is slipping or is completely released from the substrate as introduced in section 4.1. And thirdly, sticking may decrease the average value of the friction force as observed by Martins et al. [10]. Furthermore, the Pearson correlation coefficients r_1 and r_2 are computed to examine the linear correlation between the velocity of a spot $s'_{1/2}$ and the corresponding normal spring deflection $u_{z1/2}$, i.e. the corresponding normal force. More information on the correlation coefficients is given in appendix A.1.4. The velocities are computed as the central difference of the motion of the spots divided by the time step Δt:

$$s'_{1/2}(t) = \frac{1}{2\Delta t}\left(s_{1/2}(t+\Delta t) - s_{1/2}(t-\Delta t)\right) \ , \tag{4.2.15}$$

where the motion of spots $s_{1/2}$ is given as:

$$s_{1/2}(t) = x(t) + \varphi(t) - u_{x1/2}(t) \ . \tag{4.2.16}$$

Figures 4.14 and 4.15 give the correlations r_1 and r_2 for the spots. The case $r = 1$ describes a positive linear correlation between two quantities. A comparison of the different parameter ranges in both figures shows that the correlations are about -0.5 in the reduction range. This indicates a negative linear correlation of spot velocities and normal forces as low forces coincide with high velocities and vice versa. This means that the spots make most of their motion while the corresponding normal forces are low. In addition, they stick, i.e. $s'_{1/2} = 0$, while the corresponding normal force is high. Firstly, this indicates that the specimen walks as proposed in section 4.1. Secondly, this indicates that the rigid body and its contact spots make most of the forward motion while being

totally released from the substrate. This is in particular confirmed by comparison of Fig. 4.9 and Fig. 4.10, what shows that the reduction coincides with negative vertical amplitudes z_{min}, i.e. jumping of the rigid body.

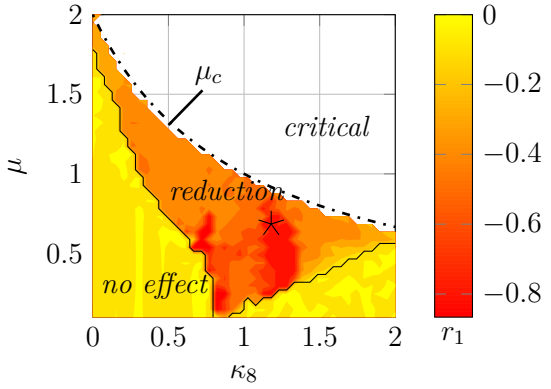

Fig. 4.14: parameter study of κ_8 and μ for the correlation coefficient r_1 of velocity s_1' and normal deflection u_{z1} of contact 1. In the reduction range applies $r_1 \lesssim -0.5$

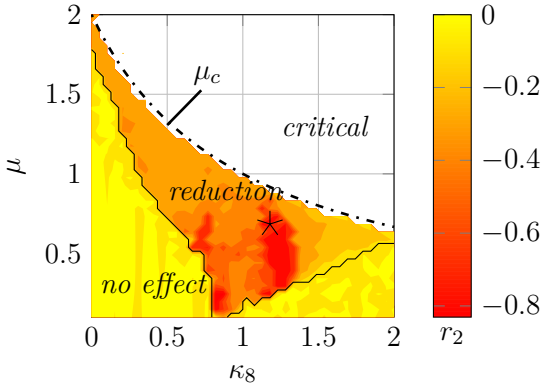

Fig. 4.15: parameter study of κ_8 and μ for the correlation coefficient r_2 of velocity s_2' and normal deflection u_{z2} of contact 2. In the reduction range applies $r_2 \lesssim -0.5$

4.2.3 Vanishing Frictional Resistance

In order to illustrate the proposed effects, the maximal reduction case is considered, which is symbolized by the black star in the figures 4.9, 4.10 and 4.12-4.15. The corresponding parameter combination is given as:

$$\kappa_{1-8} = \left(2, 1.2, 0.5, 10^{-4}, 0.68, 10^{-4}, 0.42, 1.18\right) \ . \tag{4.2.17}$$

The maximum is 98% and the corresponding minimal amplitude is $z_{min}/z_{stat} = -0.42$. This indicates jumping of the rigid body, i.e. a complete release of the contact spots. In order to examine the influence of the initial conditions on the steady state and the transient process, the DoE approach as described in appendix A.2 is used. Three initial values for each motion variable are used what gives $3^7 = 2187$ combinations of initial conditions. The initial displacements are chosen on basis of the vertical static displacement as defined in equation (4.1.22):

$$x\left(0\right), z\left(0\right), \varphi\left(0\right), x_s\left(0\right) \in \left[-z_{stat}, 0, z_{stat}\right] \ , \tag{4.2.18}$$

and the base velocity, i.e. the parameter κ_6, gives the initial velocities:

$$x'\left(0\right), z'\left(0\right), \varphi'\left(0\right) \in \left[-\kappa_6, 0, \kappa_6\right] \ . \tag{4.2.19}$$

The non-dimensional mean kinetic energy of the steady state serves as a measure:

$$\bar{e}_{kin} = \frac{1}{\kappa_4 z_{stat}} \frac{1}{2} \left(x'^2 + z'^2 + \frac{\kappa_7}{\kappa_3^2} \varphi'^2 \right) \ . \tag{4.2.20}$$

For comparison, the non-dimensional initial mechanical energy is computed:

$$e_m(0) = \frac{1}{\kappa_4 z_{stat}} \frac{1}{2} \left(u_{x1}^2 + u_{x2}^2 + \kappa_2 \left(u_{z1}^2 + u_{z2}^2 \right) + \kappa_1 \left(x_s - x + \kappa_8 \right)^2 - \kappa_4 z \right) + e_{kin}(0) \ . \tag{4.2.21}$$

Figure 4.16 gives the main effects of the initial conditions on the steady state kinetic energy, which is depicted by the red line, and on the initial mechanical energy, which is represented by the blue line. It shows that the steady state kinetic energy is not influenced by the initial conditions. One can argue that the frictional damping leads to a decay of the oscillations that are caused by the initial mechanical energy. For the considered range of initial conditions the system reaches practically the same steady state.

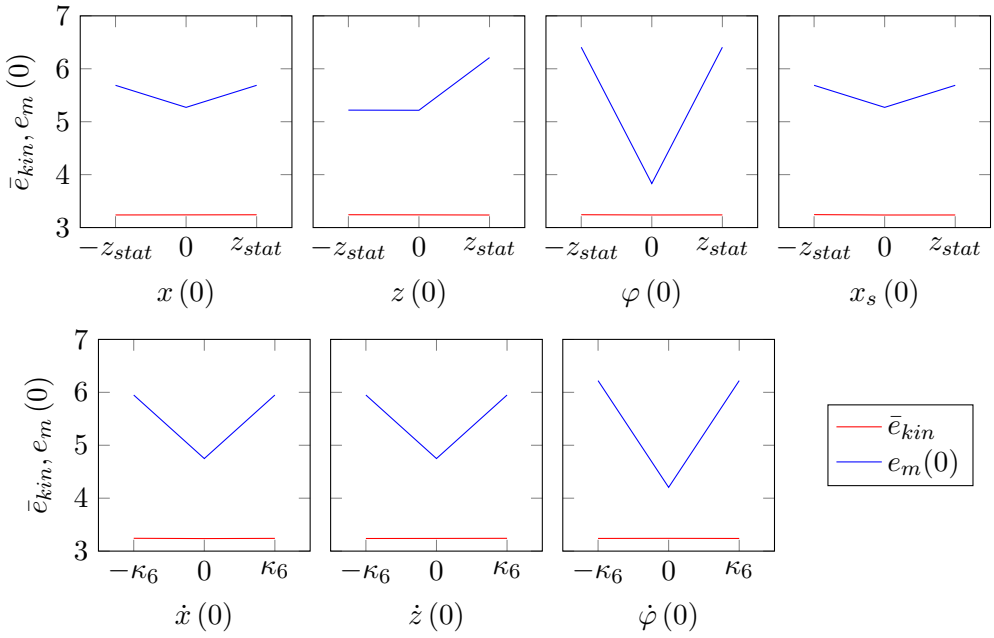

Fig. 4.16: main effect-plot of the initial conditions on the mean kinetic energy in steady state (red line) and the corresponding initial mechanical energy (blue line)

Figure 4.17 depicts the phase-space diagram for the relative displacement $x - x_s$ for the maximal reduction combination. The black dot depicts the initial conditions $x(0) = 0$ and $x'(0) = 0$. After the blue coloured transient process, the system reaches a stable limit cycle (lc), which is dark coloured. Several dynamic quantities as a function of the time $t^* = t - t_0$ in steady state are displayed in Fig. 4.18. Here t_0 indicates a time at which the transient process is already completed. The difference $\Delta x = x(t) - x(t_0)$ is shown, to give all quantities in one plot. It shows that the centre of gravity exhibits a harmonic oscillation around the static displacement z_{stat}, what leads to highly varying normal deflections of the springs. As one expects, their maximum approximately coincides with

the maximum vertical displacement. The small shift between u_{z1} and u_{z2} is caused by the rotation φ.

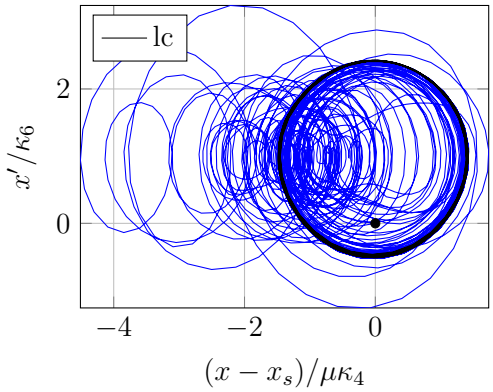

Fig. 4.17: phase space diagram of the lateral motion for the maximal reduction range. The system reaches a stable limit cycle (lc)

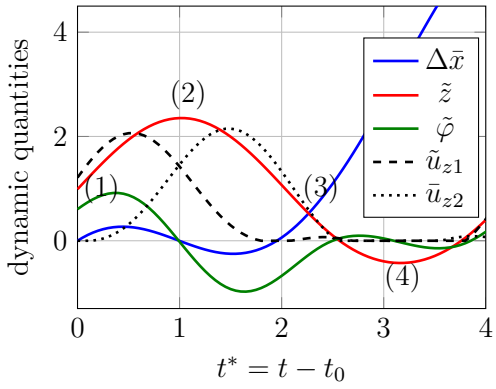

Fig. 4.18: motion of the system for the maximal reduction range. Dynamic quantities are normalized as $\Delta\bar{x} = \Delta x/\mu\kappa_4$, $\tilde{z} = z/z_{stat}$, $\tilde{\varphi} = \varphi/\mu\kappa_3\kappa_4$ and $\bar{u}_{z1/2} = u_{z1/2}/\mu\kappa_4$

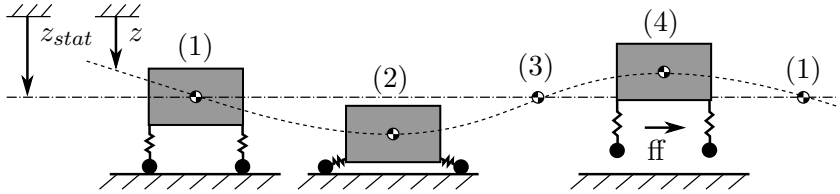

Fig. 4.19: phases of motion of the specimen in the vanishing reduction range. The rigid body follows harmonic oscillation in the vertical direction. The rotation is not shown as $\varphi < 1 \cdot 10^{-3}$ applies in steady state

The vertical motion is highly synchronized with the lateral translation x. More specifically, the rigid body makes most of the lateral displacement when the vertical displacement is negative, i.e. the body is jumping, and the contacts are released from the substrate. One can identify four specific states as marked in Fig. 4.18 and Fig. 4.19:

(1) *start of sticking phase*: sticking contact spots, downward movement and increasing normal forces, only minor lateral motion

(2) *turning point*: end of downward movement, sticking contact spots, high normal forces, storage of elastic energy

(3) *end of sticking phase*: upward movement and start of forward movement

(4) *microscopic jump*: release of the spots and zero contact forces, fast forward (ff) motion of the rigid body

The motion can be characterized as a highly synchronized vertical and lateral vibration with alternating jumping and sticking phases of the rigid body. It is this particular system behaviour that leads to an almost vanishing frictional resistance. This matches the effect of micro-walking as introduced in section 4.1.

4.2.4 Summary of the Theoretical Results

Considering the overall results of section 4.2, one can finally identify three main factors that are responsible for the reduction effect of the frictional resistance:

1. The coupling of the tangential, vertical and rotational degrees of freedom causes self-excited oscillations in the vertical direction. As the friction forces in the contact spots are mainly responsible for this, the amplitudes grow with increasing microscopic friction and lever arm of the base spring with respect to the contact spots. This effect is consistent with theoretical works of Martins et al. [10] and Adams [47].

2. The experimental works of Tolstoi et al. [39, 40, 93] showed that the normal vibrations themselves already cause a reduction due to the non-linearity between normal separation and normal force. However, in the present work a linear dependency between spring deflections and contact forces is assumed. Hence, the reduction is caused by another effect.
   The most significant effect in the micro-walking machine is the reduction of the overall resistance force that is induced by the strong correlation between low or even zero contact forces and forward motion respectively high normal forces and sticking contacts. This corresponds to the micro-walking as proposed in section 4.1.

3. Jumping and fast forward motion of the rigid body requires energy that is stored in the elastic springs. This is maintained by a characteristic alternation between storage and motion phase: the spots stick and energy is conserved that is than used for the vertical jumps and the tangential fast forward motion. Furthermore, sticking simply decreases the average value of the friction force as observed by Martins et al. [10].

One can conclude that the dynamic mode that is responsible for the reduction is the proposed micro-walking effect, i.e. a convenient synchronization of lateral and vertical motion and a jumping of the rigid body with released contacts.

4.3 Experiments

The results of section 4.2 give clear but also strict guidelines for the design of a real technical system with the effect of frictional resistance reduction through self-excited oscillations. However, there exist certain experimental limits, as discussed in detail in section 5.2. Firstly, there occur differences in the geometry and the contact configuration between theoretical and real system. These are mainly caused by the fact that the two-dimensionality of the theoretical model cannot be simply transferred to the real world in particular due to alignment problems. Secondly, there exist several practical limitations which make it impossible to reach the values of the non-dimensional parameters that are required for the almost vanishing friction. For instance, simultaneously fulfilling the conditions $\kappa_1 \approx 1$ (ratio of spring stiffness and contact stiffness) and $\kappa_4 \approx 1 \cdot 10^{-4}$ (normal force vs. contact stiffness times half width) is very hard in practice as discussed in section 5.2.3. Thirdly, the results show that there exists a critical coefficient of friction μ_c that depends on the geometry respectively the point of application of the spring force as shown in section 4.2.2. To avoid the critical range, the experiments are limited to negative values of κ_8 (ratio of lever arm of the base), i.e. the point of application of f_s is always underneath the centre of gravity. According to equation (4.2.13) this will enhance the stability of the experiment with respect to the rotation, i.e. will avoid tumbling of the rigid body, but will also decrease the reduction. Finally, some of the parameters are easier to vary in the experiments than others. For instance, it does not require much effort to change κ_8 or κ_6 (velocity of the base v_0). In contrast, changing κ_3 (slenderness of the rigid body) or κ_7 (ratio of rotational inertia) requires an update of the geometry and changing μ requires a different combination of materials. This would lead to undesired changes in several other parameters as κ_1, κ_4 and κ_6 as they depend on material properties. Overall, five parameter sets are considered which are named set 1–5. The physical parameters are given in section 5.2 in Tab. 5.2.1.

4.3.1 Experimental Results

Due to the reasons stated above, i.e. the effort for a variation of certain parameters, firstly significantly different parameter ranges without intermediate combinations are compared as listed in Tab. 4.3.1. In order to identify convenient parameter combinations, the extended model as introduced in section 5.2.3 and appendix B.4 is used. It shows that within the experimental limits, the theoretical maximal reduction is about 50%. Thus, the reduction in the experiment is expected to be lower than in the theoretical model of section 4.1. However, the contact stiffness was initially underestimated. On this basis an insufficient spring stiffness was chosen such that the stiffness parameter was $\kappa_1 = 0.1$ instead of the intended $\kappa_1 = 2$. Set 1 meets the theoretical maximal range within the experimental limits except for κ_1. Set 2 has unsuitable geometry and inertia properties, i.e. κ_3 is inconveniently changed. Set 3 and set 4 correspond to the previous ones with low κ_1, i.e. a very soft base-spring. For this purpose, a spiral spring with stiffness $k_{s-SP} = 60\,\mathrm{N/m}$ is used. In the experiments, the base velocity v_0 is varied, which is linear proportional to the non-dimensional parameter κ_6.

Tab. 4.3.1: parameters of the different sets used in the experiment. Parameters κ_2 and κ_8 are the same for all

set	κ_1	κ_2	κ_3	κ_4	μ	κ_7	κ_8
1	≈ 0.1	1.33	1.51	$2 \cdot 10^{-4}$	0.79	0.95	-0.47
2	≈ 0.1	1.33	0.85	$1 \cdot 10^{-4}$	0.79	0.25	-0.47
3	$\approx 10^{-4}$	1.33	1.51	$2 \cdot 10^{-4}$	0.68	0.95	-0.47
4	$\approx 10^{-4}$	1.33	0.85	$1 \cdot 10^{-4}$	0.68	0.25	-0.47

The spring force $F_s(t)$ is measured and the effective coefficient of friction is computed as defined in equation (5.2.2). Figure 4.20 depicts the results of the different sets. For the sake of clarity, all curves are plotted over v_0 and not over κ_6 as this parameter is cross-influenced by other quantities that change between the sets. The reduction for set 1 is about 54%, meaning that the effective friction μ_e is more than halved even for $\kappa_1 = 0.1$. In contrast, no significant reduction applies for the other sets. The effective friction slightly varies within a range of approximately 10% of μ. One can conclude, that the effect of friction minimization as introduced in section 4.2 does not occur for sets 2-4, thus $\mu_e \approx 1$. This means, just as with the theoretical results, that in order to induce the friction minimizing effect, a very narrow parameter range has to be met. In addition, the effect hardly depends on velocity but only occurs if a certain velocity limit is exceeded as can be seen for set 1 where μ_e is halved only for $v_0 \geq 15$ mm/s. However, the experimental results show that it is possible to induce the effects introduced in section 4.2 in a real system.

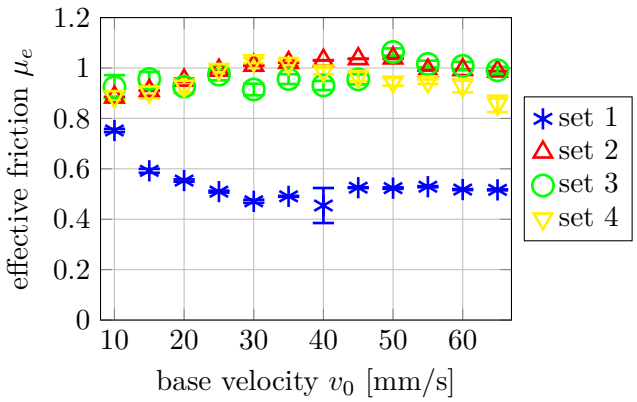

Fig. 4.20: effective coefficient of friction μ_e for varying base velocity v_0 and different parameter sets

In the experiments, the only time varying value that is measured is the spring force in the base. The normal oscillations have not been measured. Nevertheless, one can

assume that whenever instabilities occur in the normal direction, i.e. strong oscillations, they will also affect the tangential direction due to the coupling effect. Thus, self-excited oscillations in the normal direction must be detectable in the time response of the base spring. Figure 4.21 displays the time response of the spring force F_s for set 1 and set 2. It shows that in case of set 1, which is represented by the blue line, the reduction is accompanied with self-induced oscillations as F_s oscillates with high frequency and magnitude. The force reaches negative values, meaning that the specimen pushes the base point of the spring. For set 2, which is represented by the red line, the force is not oscillating and is positive all the time. In this case the instability, i.e. self-excited oscillations in the vertical direction with high amplitude, do not occur at all. Consequently no reduction is induced.

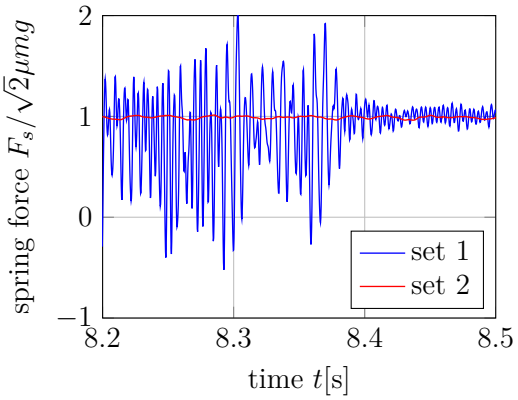

Fig. 4.21: time course of the spring force for set 1 and set 2 for $v_0 = 20$ mm/s. Instability occurs only for set 1 but stops temporarily

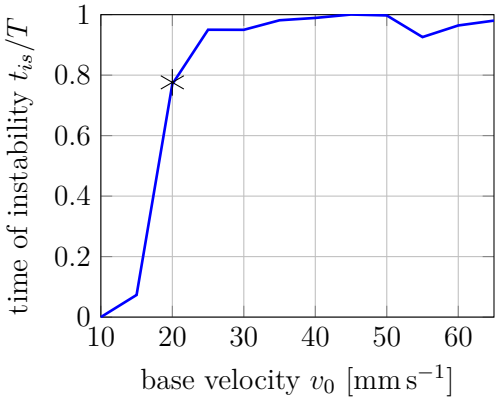

Fig. 4.22: relative time of instability t_{is} as a function of the base velocity v_0 for experimental set 1. Star shows $v_0 = 20$ mm/s

Additionally, it shows that the vibrations of the force of set 1 significantly decrease temporarily. This can be seen in Fig. 4.21 for $t > 8.4$ s. Consequently, the instability as well as the reduction effect temporarily pauses. In contrast, such an effect does not occur in the simulation at all. One can conclude that the pausing is caused by experimental imperfections rather than self-stabilization. The geometry and the microscopic friction, which is influenced inter alia by the roughness and contamination by dust, will slightly change when the substrate is moved along the specimen. In order to determine the ratio of the time the instability occurs, i.e. a significant increase of the amplitudes of F_s with negative values, and the time of observation t_{is}/T, the revolving variance $var\left(F_s\left(t\right)\right)$ of the friction force is considered. Within the Dirichlet window with size $2t_D$ of the time response, the variance is defined as:

$$var\left(F_s\left(t\right)\right) = \sqrt{\frac{1}{2t_D/\Delta t}\sum_{t_i=t-t_D}^{t_i=t-t_D} F_s\left(t_i\right) - \bar{F}_s\left(t\right)}\,, \tag{4.3.1}$$

where $\bar{F}_s(t)$ denotes the corresponding mean within the window:

$$\bar{F}_s(t) = \frac{1}{2t_D/\Delta t} \sum_{t_i=t-t_D}^{t_i=t-t_D} F_s(t_i) \; . \tag{4.3.2}$$

Here $F_s(t_i)$ denotes the spring force of the measurement sample i at time t_i. The window $2t_D$ corresponds to approximately 10 characteristic periods of $F_s(t)$. As a criterion, only those time sections are regarded as instable in which $var(F_s(t)) > 0.1$ applies. In addition, for determination of the effective friction μ_e only instable time sections are taken into account. Figure 4.22 gives the relative time of instability t_{is}/T for set 1. It shows that $t_{is} \approx T$ applies if a certain velocity limit is exceeded. Additionally the self-induced oscillations highly coincide with minimized friction as can be seen by comparison with Fig. 4.20. The instability is thus crucial for the reduction effect. This confirms the results of the theoretical model given in section 4.2.

4.3.2 Comparison of Experiment and Model

The results of section 4.2.2 indicate that the application point of the spring is from great influence for the reduction. For this reason, the joint influence of the velocity v_0, i.e. parameter κ_6, and the position of the lever arm, which refers to κ_8, is examined. Four values of κ_8 are considered. In the experiment this is simply realized by several differently positioned mounting holes, as shown in Fig. 4.23 (a). The specimen is then rotated such that the line between the selected mounting hole and the centre of gravity is vertical. As sketched in Fig. 4.23 (b), the experiments are restricted to values of $\kappa_8 < 0$ in order to reduce *unwanted* instabilities of the motion, i.e. tumbling and tilting of the rigid body.

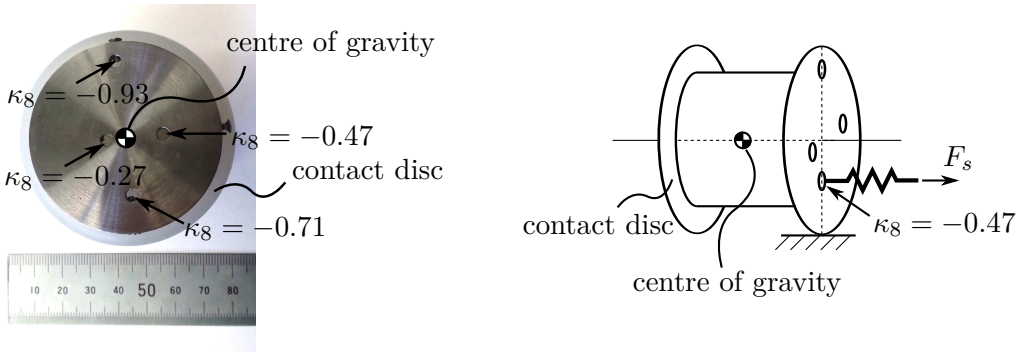

(a) front view (b) lateral view

Fig. 4.23: specimen with four positions of the lever arm of the spring with respect to centre of gravity, i.e. four values of parameter κ_8. (a) front view. (b) lateral view with the line between centre of gravity and the mounting hole for $\kappa_8 = -0.47$ being vertical

This refers to the critical coefficient as defined in equation (4.2.13):

$$\mu_c = \frac{1}{\kappa_3 \left(1 + \kappa_8\right)} \,. \tag{4.3.3}$$

Thus, the lower the value of κ_8, the higher the critical coefficient. However, this will also decrease the maximal possible reduction. For a mutual verification, the extended model is used, which is described in section 5.2.3 and appendix B.4. In comparison to the experiments shown in section 4.3.1 a stiffer material for the connection element is used and the mass of the specimen is increased to lower the influence of unwanted side-effects. With this, the maximal reduction parameter range is identified as listed in Tab. 4.3.2. Theoretically, this combination gives a maximal reduction of about 50%.

Tab. 4.3.2: maximum parameter range of the experimental set

set	κ_1	κ_2	κ_3	κ_4	μ	κ_7
5	≈ 2	1.33	1.51	$2 \cdot 10^{-4}$	0.75	1.77

Figure 4.24 shows a contour plot of the effective coefficient of friction for 1600 combinations of v_0 and κ_8. Both, higher values of v_0 and κ_8 increase the reduction. Thus, a higher rotational moment of the spring force with respect to the contact spots leads to higher reduction. Additionally, the yellow area shows the limit range which is delimited by the black line. Here no reduction occurs at all. Thus, one can conclude that there exists a limit velocity that has to be exceeded in order to induce the reduction effect. And that this limit velocity depends on the lever arm of the spring.

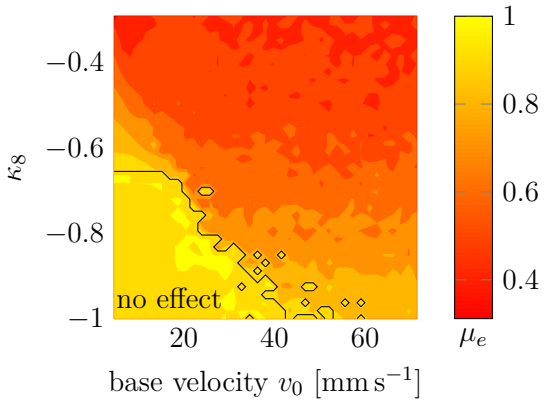

Fig. 4.24: surface plot of the effective coefficient of friction μ_e as a function of v_0 and κ_8. Simulation model

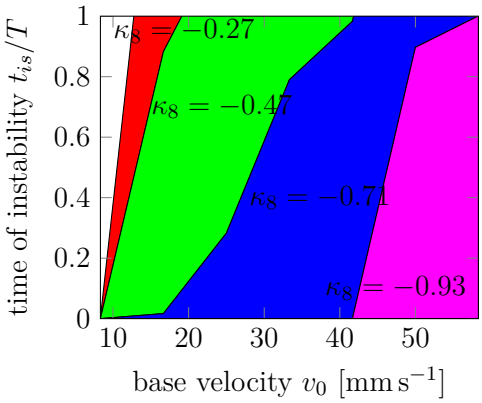

Fig. 4.25: area plot of time portion of the instability t_{is}/T as a function of base velocity v_0 for different κ_8. Experiment

Figure 4.26 gives a comparison of the theoretical values, which are symbolized by the circles, and the experimental results, which are denoted by the error-bars and marks.

Although there occurs a certain deviation between theory and experiments, the overall trend is similar. A certain velocity limit exists that has to be exceeded for the reduction effect to occur. For $\kappa_8 = -0.93$ and $\kappa_8 = -0.71$ this velocity threshold is about $v_0 = 40$ mm/s respectively $v_0 = 25$ mm/s. This agrees with the simulation as shown by the corresponding pink and blue circles. For $\kappa_8 = -0.47$ and $\kappa_8 = -0.27$ the limit velocity is approximately $v_0 = 15$ mm/s. This does not coincide with the simulation, where no limiting velocity exists for these values of κ_8. However, in the experiments the reduction increases with increasing velocity once the limit velocity is exceeded, what agrees with the simulation. It turns out that for every κ_8 examined, the specific maximal reduction is higher in the experiments. For $\kappa_8 = -0.93$ the reduction is 52%, for $\kappa_8 = -0.71$ it is 48% and for $\kappa_8 = -0.47$ it is 60% in the experiments. The maximal reduction is 73% and occurs for $\kappa_8 = -0.27$.

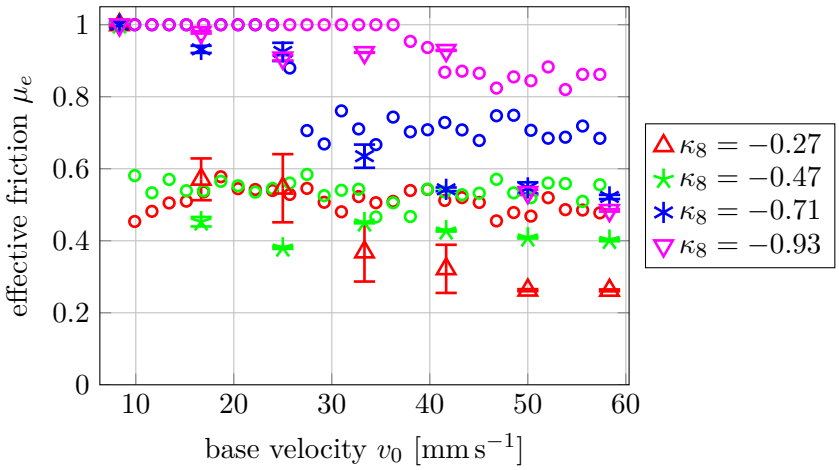

Fig. 4.26: effective coefficient of friction μ_e as a function of base velocity v_0 for different κ_8. Simulation (circles) and experiment (error-bars and marks) show that a velocity limit has to be exceeded to induce the friction minimizing effect

In addition, Fig. 4.25 gives area plots of the time portion of instability t_{is}/T for the four cases of κ_8. The time of instability is determined on basis of the revolving variance as defined in equation (4.3.1). It shows that t_{is} increases with the base velocity v_0 and lever arm ratio κ_8. Thus, the higher the rotational moment of the spring force of the base with respect to the contacts, the higher is the relative time of instability. In addition, the velocity threshold for the instability to occur, i.e. the velocity for which $t_{is} \approx 1$ applies, is lower for a higher rotational moment. Comparison of Fig. 4.25 and Fig. 4.26 shows that the reduction effect also highly coincides with increased time portion of instability. The experimental results confirm the results of the DoE as shown in Fig. 4.7, where the reduction increases with increasing κ_8 and increasing velocity, i.e. increasing parameter κ_6. As stated in section 4.2.2, the reduction effect is caused by self-excited vertical oscillations of the rigid body. These oscillations increase with an increasing moment of the spring force with respect to the contacts what increases the coupling between the

rotational moment and the friction forces. In addition, the oscillations increase with the velocity as this increases the kinetic energy that is transferred to the vertical motion through the coupling effect. The effect of decreasing kinetic friction with increasing velocity was experienced in many experiments [77, 78, 79] where an overview is given for example in [9]. The same effect also occurs in theory as in the slip wave model of Adams [50] or in the rigid body model of Martins et al. [10]. However, the deviations between experiment and model are relatively high. One reason for this might be a deviation between the real parameters of the experiment and the theoretical values. Another one might be that the model does not capture the true contact mechanics. Section 5.2.3 gives a detailed discussion of the deviations between theory and experiment.

4.4 Summary

On basis of important experimental [39, 40] and theoretical works [10, 47] a simulation model is introduced, in order to examine the influence of the system dynamics on sliding friction. The model captures known basic effects as the coupling between normal and tangential motion and adds features as the spatial variation of stick and slip zones. In theory, the frictional resistance almost vanishes when a certain parameter range is met. If so, self-excited vibrations in the vertical direction occur and the system moves in a characteristic dynamic mode. The different mechanisms that are responsible for the reduction can be summarized as:

1. self-excited oscillations in the vertical direction caused by the coupling effect
2. strong correlation between low or even zero contact forces and forward motion
3. characteristic alternation between storage and motion phase

In the reduction mode the system moves in such a way that the forward motion is highly synchronized with the vertical vibrations and thus normal forces in the contact. It moves forward at low normal forces or even released contacts and almost stops at high normal forces. This dynamic mode is referred to as micro-walking. The amplitudes of the vertical oscillations can be rather small, i.e. they are from the order of the static vertical displacement, and can thus be characterized as microscopic. This means that a significant reduction can be accompanied with apparently smooth sliding of the system, i.e. the oscillation can remain undetected in a real system.
Both, simulations and experiments, show that the reduction requires a sufficient speed and high moment of excitation with respect to the contact spots to enhance the kinematic coupling and the self-excited vibrations. Another important criterion for the effect to occur is a similarity of the excitation and contact stiffness, meaning that there is a medium guidance of the base motion. The experiments confirm the theoretical results with the maximal reduction being 73%. However, there is a discrepancy between simulation and experiment as the final results differ slightly indicating that further research is needed. In this, attempts should be made to achieve the theoretical maximal range with a reduction of 98 %, i.e. with an almost vanishing macroscopic frictional resistance.

Chapter 5

Experimental Analysis

Two tribological experimental rigs have been built in order to examine the theoretical results. Firstly, the rolling body test rig. It is used to investigate the effects of shakedown and ratcheting in incomplete contacts and is described in section 5.1. Secondly, the micro-walking machine test rig which is used to measure the influence of system dynamics on sliding friction. This experimental rig is introduced in section 5.2. The computers and measurement devices of the Institute of Mechanics have been used for measurement and control of the experiments. The measurement results in the present work are given with confidence interval on the confidence level 68.3%, as described in appendix A.1.1.

5.1 Experimental Rig for the Rolling Body Effects

The experimental rig sketched in Fig. 5.1 is used to investigate the effect of oscillating rolling. It is mounted on a vibration-isolated table in order to minimize the influence of external dynamic interferences. The experimental rig consists of a drive unit with joint kinematics, rolling body (1) and a movable substrate (2), which is mounted on a friction reduced cross-roller table. The tangential force is applied through a weight pot which is connected to the substrate via a string. This enables an efficient and precise control of F_T which is the result of the force of gravity of the pot $G = m_T g$ reduced by the resistance force of the cross-roller table, i.e. $F_T = m_T g - F_W$. The resistance force is measured to be $F_W = 0.1$ N. The force of gravity of the sphere acts as the normal force F_N, which is measured at the centre of the contact using a load cell. The rolling motion is generated by the linear drive and the joint kinematics. In theory, the fulcrum of the lever arms is on the same level as the contact point of the rolling body, see also section 5.1.5. Consequently, a lateral motion of the linear drive with amplitude W leads to a rotation of the lever arm with an angle of rotation:

$$\varphi \approx \left(\frac{W}{R}\right) , \tag{5.1.1}$$

where R denotes the radius of the rolling body. This leads to a lateral motion of the bearing points x_m und x_o shown in Fig. 5.1. Assuming small amplitudes $\varphi \ll 1$ the

lateral motion results to:

$$x_m = W \quad \text{and} \quad x_o = 2W \,, \tag{5.1.2}$$

what leads to a rolling motion of the body in which the actual point of contact corresponds to the instantaneous centre of motion.

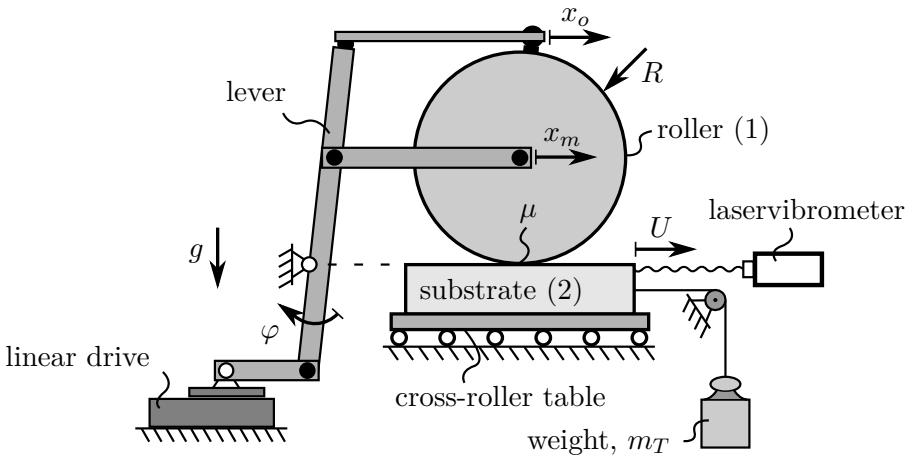

Fig. 5.1: experimental rig for the oscillating rolling: rolling body (1), kinematic joints and movable substrate (2)

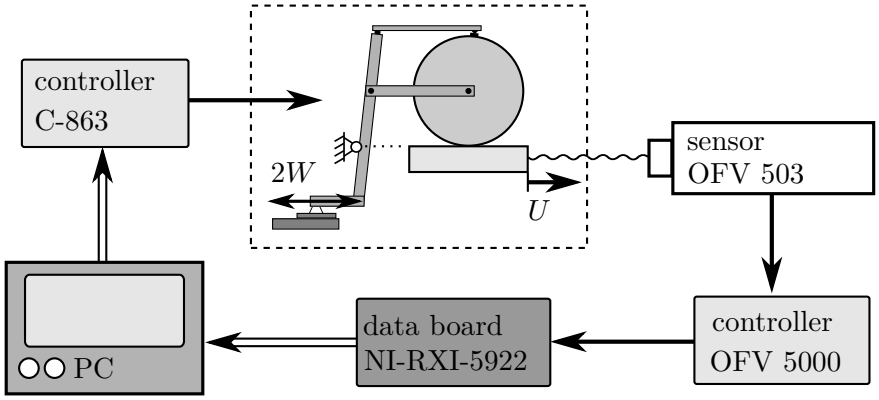

Fig. 5.2: experimental rig for the oscillating rolling with measurement chain consisting of laservibrometer, controller and PC

In order to keep the deviation from theoretical, ideal rolling motion as small as possible, an accurate adjustment of the geometry is needed. This is achieved using spacers between the substrate and the cross-roller table and spring washers on the upper bearing points. The entire experimental rig including the measurement chain is depicted in Fig. 5.2. As described previously, the rolling motion is generated by a high precision linear drive M 403.02-DG/M 405-DG which is controlled using a C-863 controller. Both devices are

made by *Physik Instrumente GmbH & Co. KG*. The displacement of the substrate U is measured by a laservibrometer. It consists of the sensor unit OFV 503 and the controller FV 5000 both made by *Polytec GmbH*. The measurement resolution in the experiments is 80 nm. The electrical output signals of the controller are fed to the PC using a 24-bit data acquisition card NI PXI-5922 made by *National Instruments Corporation*.

5.1.1 Parallel Alignment of Force and Oscillation

Figure 5.3 shows the experimental set-up for the parallel case, including the vibration-isolated table. Here the rolling body (1) is a massive steel sphere and the substrate (2) consists of silicone rubber with a thickness of 8 mm. Both, the Young's modulus of the substrate E_2 and the coefficient of friction between sphere and substrate μ are determined using the least square method (LS), as described in appendix A.1.2. In this, the static displacement U_{stat} as a function of F_T is measured firstly and the according static displacement for different combinations of the parameters E_2 and μ is computed using equation (2.1.18). Secondly, the parameters for which the sum of the squared deviations between experiment and theory is the smallest are identified. For the parallel set-up, this gives $E_2 = 5.2$ MPa and $\mu = 0.57$. There are two reasons for this procedure. Firstly, the experimental setup does not allow a sufficiently accurate direct measurement of μ. Secondly, only mean values of the Shore-A hardness without tolerance ranges are known. If the given mean value for the Shore-A hardness is used, the Young's modulus results to $E_2 \approx 5$ MPa according to Boussinesq, respectively $E_2 \approx 6$ MPa according to Kunz and Studer where both values are taken from [98]. This matches the values gained using the mean square method. In addition, the optical measurements as explained in section 5.1.5 give almost the same contact radii as the theory taking into account the fitted values. Table 5.1.1 gives all important parameters of the parallel set-up.

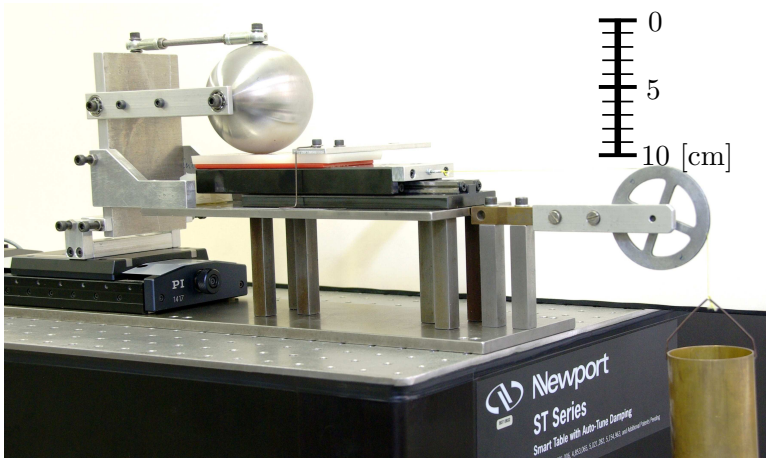

Fig. 5.3: rolling body experimental rig with sphere and parallel alignment of tangential force F_T and oscillating rolling W

Tab. 5.1.1: parameters of the rolling body experimental rig with sphere and parallel alignment of force F_T and direction of the rolling W

parameter	symbol	value	unit
radius	R	40	mm
coefficient of friction (LS)	μ	0.57	1
Young's modules (LS)	E_1/E_2	$206 \cdot 10^3/5.2$	MPa
Poisson-ratios	ν_1/ν_2	0.3/0.5	1
normal force	F_N	21.1	N
contact radius	a	4.56	mm
indentation depth	d	0.52	mm

5.1.2 Perpendicular Alignment of Force and Oscillation

In this case, the rolling is aligned perpendicular to the tangential force as shown in Fig. 5.4. Again, a solid steel sphere acts as the rolling body (1) and silicon rubber with thickness 8 mm is used for the substrate (2). Likewise, the parameters μ and E_2 are determined with the least square method: $E_2 = 4.35$ MPa and $\mu = 0.93$. The difference to the parallel case is because another sort of silicone from another supplier is used. Again, the optical measurements as explained in section 5.1.5 show a good agreement with the theory taking into account the fitted values. Table 5.1.2 provides a summary of all important parameters for the perpendicular alignment.

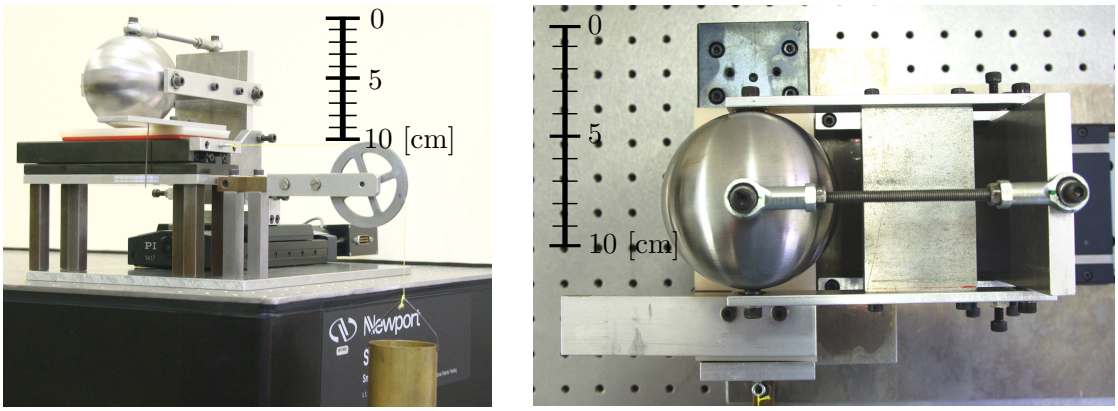

(a) lateral view (b) top view

Fig. 5.4: rolling body experimental rig with sphere an perpendicular alignment of tangential force F_T and oscillation W. (a) lateral view and (b) top view

Tab. 5.1.2: parameters of the rolling body experimental rig with sphere and perpendicular alignment of force F_T and direction of the rolling W

parameter	symbol	value	unit
radius	R	40	mm
coefficient of friction (LS)	μ	0.93	1
Young's modules (LS)	E_1/E_2	$206 \cdot 10^3/4.35$	MPa
Poisson-ratios	ν_1/ν_2	0.3/0.5	1
normal force	F_N	21.19	N
contact radius	a	4.8	mm
indentation depth	d	0.58	mm

5.1.3 Cylindrical Roller and Parallel Alignment

In this case, a cylindrical roller with radius 40 mm and length 80 mm is used as the rolling body (1) and silicone rubber with 5 mm thickness is used for the substrate (2). As shown in Fig. 5.5 (a), rolling motion and tangential force are aligned parallel to each other. The cylinder has a 1 mm chamfer and almost flushes with the substrate. This configuration is chosen in order to minimize the influence of the edges of the contact on the pressure distribution, as discussed in detail in section 5.1.5. Again, another sort of silicone rubber is used. With the least square method the parameters result to $\mu = 0.79$ and $E_2 = 3.6$ MPa. In this case the results of the three dimensional simulation are used for comparison. Again, the fitted values show good agreement with the optical measurements. Other important parameters are listed in Tab. 5.1.3.

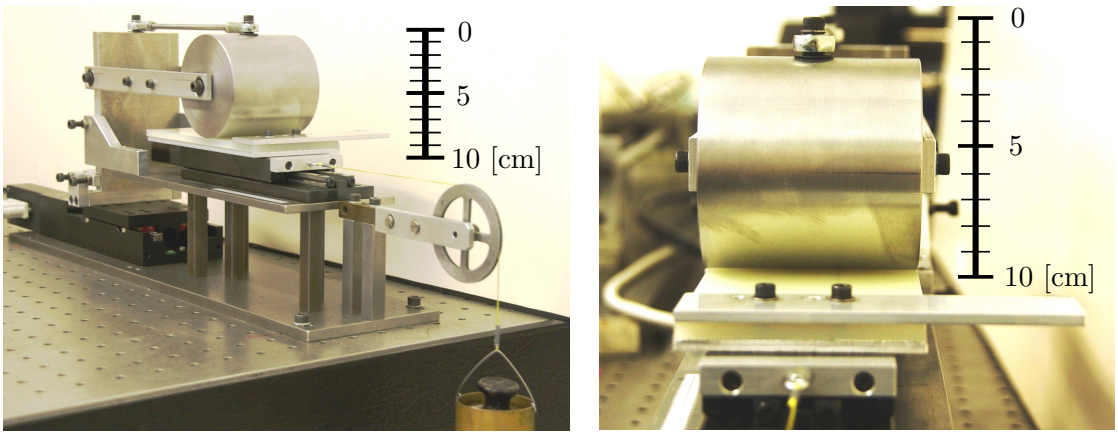

(a) lateral view (b) front view

Fig. 5.5: (a) rolling body experimental rig with cylindrical roller an parallel alignment of tangential force F_T and rolling amplitude W. (b) cylindrical roller almost flushes with the substrate

Tab. 5.1.3: parameters of the rolling body experimental rig with cylindrical roller and parallel alignment of force F_T and direction of the rolling W

parameter	symbol	value	unit
radius	R	40	mm
length	L	80	mm
coefficient of friction (LS)	μ	0.79	1
Young's modules (LS)	E_1/E_2	$206 \cdot 10^3/3.6$	MPa
Poisson-ratios	ν_1/ν_2	0.3/0.5	1
normal force	F_N	32.3	N
contact width	$2a$	4.2	mm
indentation depth	d	0.26	mm

5.1.4 Experimental Procedures

In order to increase the reproducibility, it is briefly described how the experiments are conducted and a few time responses of measured values are shown. For the shakedown case the final experimental results are given in the sections 3.2.2, 3.4.2 and 3.5.3. For the ratcheting case the final experimental results are given in the sections 3.3, 3.4.3 and 3.5.4. The parameters of influence f_T and w as well as the displacement u are normalized as described in equation (3.1.4) for the spherical rollers respectively equation (3.5.13) for the cylindrical roller.

Shakedown for Spherical and Cylindrical Rollers The procedure to measure the shakedown displacement u_{sd} of the substrate is as follows:

1. placing of the rolling body on the substrate
2. application of the tangential force f_T using the weight pot
3. wait for $60 - 90$ s until static equilibrium is reached
4. oscillating rolling for $n = 12$ periods with specific subcritical amplitude $w < w_{lim}$

In order to study a particular combination of parameters three to five iterations, i.e. measuring runs, are performed before the experimental set-up is changed. Figure 5.6 shows the time response of the displacement of the substrate for $f_T = 0.19$ and different w in case of $w \perp f_T$. The displacement stops after several periods and a safe shakedown occurs. The small oscillations around the shakedown displacements are caused by slight geometrical deviations, as explained in section 5.1.5. The last value of the displacement was chosen as the resulting displacement after shakedown. The roller is then in its initial upright position. Examples of time responses for $w \parallel f_T$ and for the cylindrical roller are not given here, as they are very much the same, except for the final displacement.

Shakedown Limits for Spherical Rollers Figure 5.7 gives the displacement for $f_T = 0.64$ and $w \perp f_T$ for the limit case and three experimental runs. These experiments are used to determine the maximal amplitude w_{lim}. Therefore, starting from a safe shakedown state, the amplitude is increased stepwise $W = W + \Delta W$ until ratcheting occurred. The asterisks delimit the intervals in which the amplitude is held constant. The complete procedure to identify the maximal amplitude w_{lim} is as follows:

1. placing of the rolling body on the substrate
2. application of the tangential force f_T using the weight pot
3. wait for $60 - 90$ s until static equilibrium is reached
4. oscillating rolling for $n = 5 - 10$ periods and subcritical amplitude $w < w_{lim}$
5. increasing of the amplitude $W = W + \Delta W$
6. repeating of step 4. and 5. until ratcheting occurs

The incremental increases of the amplitudes are chosen as:

$$w \parallel f_T \Rightarrow \Delta W = 0.1 \text{ mm} , \tag{5.1.3}$$

$$w \perp f_T \Rightarrow \Delta W = 0.05 \text{ mm} . \tag{5.1.4}$$

The last amplitude before ratcheting is identified as the maximal amplitude w_{lim} and the result is the mean of three measurement runs. The time responses for the parallel case $w \parallel f_T$ are not given here, as they match with the perpendicular case except for the exact values.

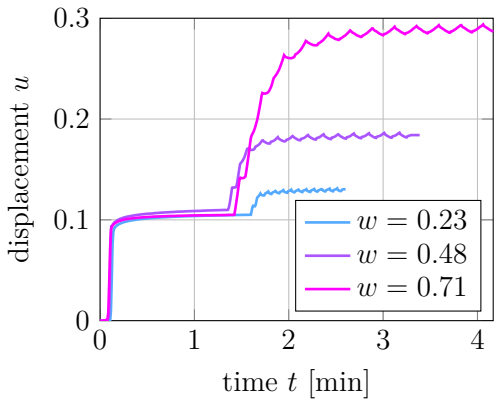

Fig. 5.6: displacement u for different oscillation amplitudes w and $f_T = 0.19$ in case of $w \perp f_T$ and shakedown

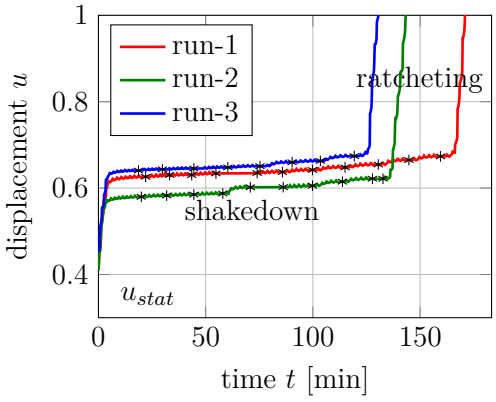

Fig. 5.7: three measurement runs for the displacement u for $f_T = 0.64$ and stepwise increase of w in case of $w \perp f_T$ for determination of w_{lim}

Shakedown Limits for Cylindrical Rollers The measurement procedure for determination of the maximal amplitude w_{lim} in case of the cylindrical roller resembles the one for the spherical rollers:

1. placing of the rolling body on the substrate
2. application of tangential force f_T using the weight pot
3. wait for $60 - 90$ s until static equilibrium is reached
4. oscillating rolling for $n = 60$ periods and sub-critical amplitude $w < w_{lim}$
5. increase amplitude $W = W + \Delta W$ with $\Delta W = 0.05$ mm
6. repeat step 4. and 5. until ratcheting occurs

Unfortunately, the distinction between shakedown and ratcheting is not as clear as for the spherical case even for a highly increased number of periods, i.e. 60 instead of 10. Figure 5.8 shows the displacement for $f_T = 0.42$ and a stepwise increase of w for three experimental runs. As can be seen, there occur regions of clear shakedown and regions of clear ratcheting with high incremental displacement per period. Here, the displacement for $f_T = 0.42$ and a stepwise increase of w is shown for three experimental runs. The asterisks delimit the intervals in which the amplitude is held constant. It shows that the transition region is ambiguous what makes it hard to identify the maximal amplitude.

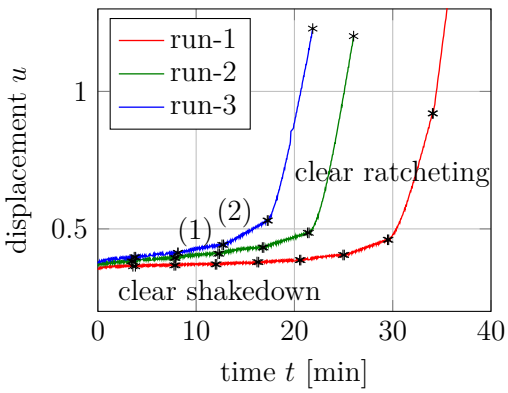

Fig. 5.8: displacement u for $f_T = 0.42$ and stepwise increase of w in case of the cylinder for determination of w_{lim}

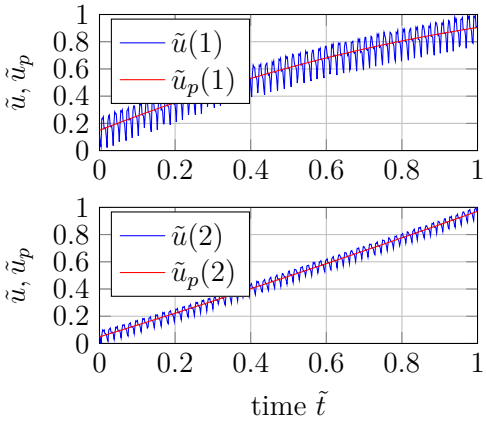

Fig. 5.9: conditioned displacement $\tilde{u}$ and polynomial fit $\tilde{u}_p$ for the intervals (1) and (2) in Fig. 5.8

In order to give a distinct and comprehensible criteria, the displacement of the substrate $\tilde{u}$ for a specific amplitude w is approximated with a second order polynomial fit:

$$\tilde{u}_p = p_2(w)\,\tilde{t}^2 + p_1(w)\,\tilde{t} + p_0(w) \ . \tag{5.1.5}$$

Here, $\tilde{u}$, $\tilde{u}_p$ and $\tilde{t}$ denote the conditioned and normalized displacement and time such that in the interval the displacement starts with 0 and reaches 1 at the end:

$$\tilde{u}\left(\tilde{t}=0\right)=0, \quad \tilde{u}\left(\tilde{t}=1\right)=1\ . \tag{5.1.6}$$

An example for the conditioned displacement as well as the polynomial approximation is given in Fig. 5.9. These refer to the intervals (1) and (2) of Fig. 5.8. It is assumed that the system still approaches a state of shakedown as long as the curvature of the polynomial fit (5.1.5) is negative. Otherwise ratcheting must have started:

$$\frac{\partial^2 \tilde{u}_p}{\partial \tilde{t}^2} < 0 \Rightarrow \text{ shakedown}\ , \tag{5.1.7}$$

$$\frac{\partial^2 \tilde{u}_p}{\partial \tilde{t}^2} > 0 \Rightarrow \text{ ratcheting}\ . \tag{5.1.8}$$

The last shakedown amplitude is then identified as the maximal shakedown amplitude. For the examples given in Fig. 5.9 the curvatures yield -0.65 for interval (1) and 0.13 for interval (2). Thus, one can conclude that the system still shakes down for w in interval (1) and ratcheting has started for w in interval (2). This is done for all the measurement runs.

Finally, the maximal amplitude is computed as the mean value of three measurement runs. Due to the described processes the maximal displacement cannot be read directly as the system has still not reached the final shakedown state. Therefore, an artificial criterion for determining the maximal displacement is defined. The displacement of the last shakedown interval U_{sd} and the first ratcheting interval U_{rt} are approximated linearly:

$$U_{sd}\left(t\right)=p_{11}t+p_{01} \quad \text{and} \quad U_{rt}\left(t\right)=p_{12}t+p_{02}\ . \tag{5.1.9}$$

The intersection of the two lines $U_{sd}\left(t\right)=U_{rt}\left(t\right)$ is assumed to give the maximal displacement:

$$U_{lim}=\frac{p_{02}-p_{01}}{p_{11}-p_{12}}p_{11}+p_{01}\ . \tag{5.1.10}$$

Although the maximal displacements match the theoretical values relatively good, see Fig. 3.45 in section 3.5.3, the deviations of the maximal amplitudes are relatively high, see Fig. 3.44 in section 3.5.3. For the maximal amplitudes w_{lim} the mean deviation is approximately 16%. Thus the maximal force $f_{T,lim}$ in the experiments is 16 % higher than the theoretical prediction. Due to the strong agreement between theory and simulation, see again Fig. 3.44 in section 3.5.3, one can conclude that the experiment is somehow faulty. Potential causes are:

- an incorrect criterion for the determination of the maximal amplitude
- deviations in the alignment of tangential force and rolling amplitude
- deviations in the pressure distribution, as discussed in section 5.1.5
- erroneous determination of the parameters of the experimental rig

Ratcheting for Spherical and Cylindrical Rollers The measurement procedure for determining the incremental displacement Δu is the same in all three cases that are considered:

1. placing of the rolling body on the substrate
2. application of tangential force f_T using the weight pot
3. wait for $60 - 90$ s until static equilibrium is reached
4. oscillating rolling for $n = 10 - 20$ periods and supercritical amplitude $w > w_{lim}$

In order to study a particular combination of parameters three to five iterations, i.e. measuring runs, are performed before the experimental set-up is changed.

5.1.5 Analysis of Deviations

Dynamic Influences In order to estimate the dynamic influences of the test rig, the eigenfrequencies of the system are determined. For this purpose, the rolling body and the main board of the joint kinematics are assumed to be rigid and only three degrees of freedom are considered: translation and rotation of the roller and translation of the substrate. The remaining components are modelled as linear elastic springs. With the values of Tab. 5.1.1 the first eigenfrequency [99] for the spherical roller and the parallel alignment of force and oscillation results to $f_1 = 22$ Hz. The highest excitation frequency occurs for the smallest amplitude $W = \frac{1}{4}a$. With a drive speed of $\dot{W} = 1$ m/s the highest excitation frequency results to $f_0 = 0.21$ Hz and is thus two orders of magnitude less than f_1. The excitation and the displacement of the substrate can thus be assumed to be quasi-static in relation to the natural oscillations of the system. In turn, its dynamic influences are neglected.
Also for the perpendicular alignment the eigenfrequencies are estimated using a simplified system with rigid body degrees of freedom only. With the values of Tab. 5.1.2, the first eigenfrequency results to $f_1 = 19$ Hz which also exceeds the highest excitation frequency of $f_0 = 0.21$ Hz by two orders of magnitude. The difference between the two settings is caused by the fact that the bending stiffness of the lever arms is lower than their tensile stiffness. Again, the dynamic influences of the system are neglected. For the cylindrical roller, the eigenfrequencies are assumed to be comparable to the settings with spherical rollers. Thus the excitation and the displacement of the substrate are again assumed to be quasi-static in relation to the natural oscillations.

Kinematic Deviations Figure 5.10 depicts the rigid body displacement of the spherical rolling contact for $w \parallel f_T$ in case of shakedown. As one can see, some slight oscillations occur in the shakedown state. These are caused by small geometrical deviations of the experimental setting. The model is such that the main bearing of the lever kinematics is on the same level as the lowest point of the rigid sphere, i.e. the contact point. Thus, the instantaneous centre of motion of the sphere coincides with its

lowest point. However, in the experiment occurs a small deviation Δh such that the true instantaneous centre is on a higher level, as depicted in Fig. 5.11. During rolling, this will induce a small displacement of the substrate $\Delta\hat{U}$ which is a function of the rotation $\varphi \approx \frac{W}{R}$ around the instantaneous centre of motion:

$$\Delta\hat{U} = \frac{W}{R}\Delta h \; . \tag{5.1.11}$$

This effect causes slight oscillations of the displacement around the shakedown value as can be seen in Fig. 5.10. These oscillations also occurred in the unloaded case, i.e. $f_T = 0$. For the parallel case and $f_T = 0$ and $w = 0.75$ the amplitude of the oscillation is measured:

$$\Delta\hat{U} = (1.55 \pm 0.13)\ \mu\text{m} \Rightarrow \Delta h = (62.17 \pm 5.38)\ \mu\text{m} \; . \tag{5.1.12}$$

One can assume that these oscillations are from the same order for all the cases that are considered. Although these geometric deviations might have a small influence on the contact area, this effect can be neglected. The displacement u when the roller is in its upright position is taken as the experimental result u_{sd} for the shakedown case.

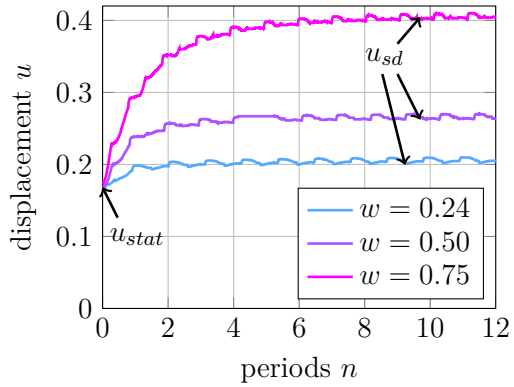

Fig. 5.10: displacement u for different oscillation amplitudes w and $f_T = 0.24$ in case of shakedown for $w \parallel f_T$ (experiment)

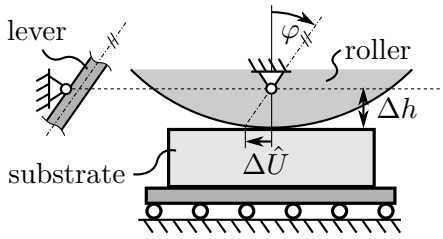

Fig. 5.11: height difference between bearing and contact point Δh causes deviation of the displacement $\Delta\hat{U}$

Half-Space Assumption In the experiments, a rubber substrate is used that is glued to a metal plate which again is mounted on the cross roller table. It is to be discussed to which extent the finite layer thickness of the rubber b contradicts the theoretical assumption of a semi-infinite substrate. The half-space model assumes that all boundaries of the semi-infinite bodies are sufficiently distant from the contact, so that the relative displacements in the contact are independent of the remote boundary conditions [52]. The elastic deformations decrease with $1/r$, with r being the distance to the contact area, and the stresses and strains decrease in proportion to $1/r^2$. Therefore, the elastic energy of the deformation is concentrated in a volume with linear dimensions of the

order of the contact width D_c [65], as shown in Fig. 5.12. Considering this, the layer thickness is of great influence for the contact stresses and the contact area. In case that $b \gg D_c$, the half-space assumption is not violated and the contact stresses are given by the Hertz theory [56]. In case that $b < D_c$ the contact area is reduced and the maximum pressure is increased in comparison with the Hertzian solution [100].

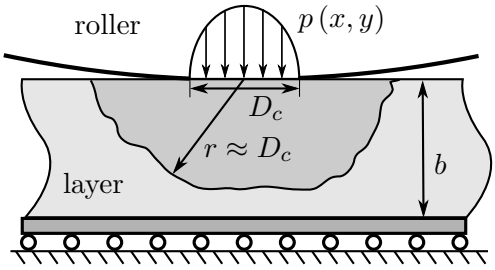

Fig. 5.12: model of the contact between roller and elastic layer of thickness b. Deformation is concentrated in a volume with linear dimensions of the order of the contact width D_c (shaded area)

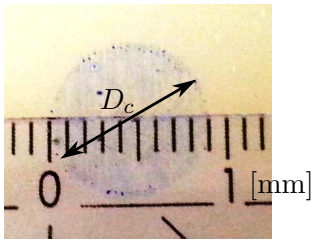

Fig. 5.13: optical measurement of the contact area in case of the spherical roller. The diameter is approximately $D_c \approx 9$ mm

For the experiments, the ratios of the layer thickness b and the contact length D_c are calculated as:

$$\left(\frac{b}{D_c}\right)_{sphere} = \frac{8\text{ mm}}{9\text{ mm}} \approx 0.9 \quad \text{and} \quad \left(\frac{b}{D_c}\right)_{cylinder} = \frac{5\text{ mm}}{4.2\text{ mm}} \approx 1.2\,. \tag{5.1.13}$$

The layer thickness is thus of comparable size as the contact length D_c. For frictional contacts incorporating elastic layers as in the experiments presented here, the contact can assumed to be effectively Hertzian for $b \geq D_c$ [101, 52]. Thus, one can conclude that the experiments are sufficiently covered by the Hertzian theory and satisfy the half-space assumption. This is also supported by optical measurements of the contact radii. In these, the rollers are covered with stamping ink before indentation. After removing the roller from the substrate, a coloured imprint remains at the surface that indicates the size of the contact area, as shown in Fig. 5.13. The measured radii agree well with the theoretical values computed with the Hertz theory.

Boundary of the Cylindrical Contact The model of the cylindrical rolling contact assumes the stress distribution to be constant in the y direction perpendicular to the rolling. However, the finite length of the cylinder causes a much sever state of stress in the contact. Although the Hertzian theory predicts the pressure correctly over the majority of the contact, significant deviations occur at the boundaries [56], as shown in the diagrams in Fig. 5.14. In case of two coincident sharp ends as shown in Fig. 5.14 (a), the free end of the solids expand slightly what reduces the pressure as:

$$p_0' \approx \left(1 - \nu^2\right) p_0\,. \tag{5.1.14}$$

A sharp stress concentration occurs when the mating substrate extends beyond the roller, as in Fig. 5.14 (b). For a frictionless contact with $\beta = 0$, the pressure in the close neighbourhood of the edge will vary as $y^{-0.23}$ [102]. This problem is typically avoided by barrelling the rollers as depicted in Fig. 5.14 (c). Here, the pressure increases slightly and then relaxes, resulting in a dog-bone shape of the contact area. Provided that the radius at the ends is significantly larger than the contact width, both bodies can be regarded as half-spaces [56]. Kunert gives the profile correction for the cylinder, that is needed to leave unchanged the elliptical pressure in the rolling direction but to achieve a constant pressure in the perpendicular direction [89]. However, such a profile is very difficult to manufacture and is correct only at the design load.

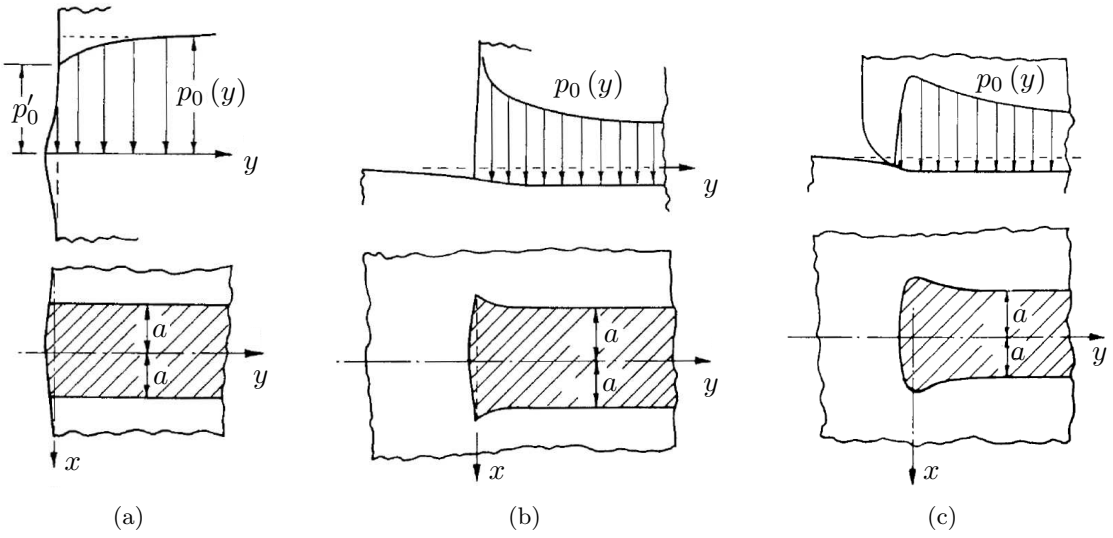

Fig. 5.14: boundary effects of the cylindrical roller. (a) two coincident sharp ends, (b) one sharp end and (c) rounded end, taken from [56]

Considering these relations and practical restrictions of the measurement set-up, the test rig is built as a mixture of type (a) and (c). The cylinder has a 1 mm chamfer and almost flushes with the substrate. In addition, the ratio of the length of the line contact L and the contact width $2a$ is $L/a \approx 20$. Although these characteristics might minimize the boundary effects, they cannot fully be neglected. The increased maximal pressure in case (c) might be one reason for the increased maximal load that is observed in the experiments in comparison with the theoretical value, as shown in section 3.5.3 in Fig. 3.44.

Viscoelasticity of Rubber The silicone rubber, which serves as the substrate in the experiments, is assumed to be elastic in the considered parameter range. In fact the rheology of rubber is characterized as viscoelastic, meaning that it exhibits both elastic and viscous characteristics. Mechanically, this is described by the time dependent shear

modulus $G(t)$ function:

$$G(t) = \frac{1}{2\pi} \int_{-\infty}^{\infty} \frac{1}{\omega} \left(G' \sin(\omega t) + G' \cos(\omega t) \right) \mathrm{d}\omega \ . \tag{5.1.15}$$

Here G' and G'' denote the storage respectively the loss modulus and ω is the frequency of the stress acting inside of the rubber [55]. The standard rheological model for rubber is a combination of a spring (G_1) and a so called Maxwell element, which is a series connection of another spring (G_2) and a dash-pot (η), as shown in Fig. 5.15 (b). Usually for rubber, G_2 is much larger than G_1.

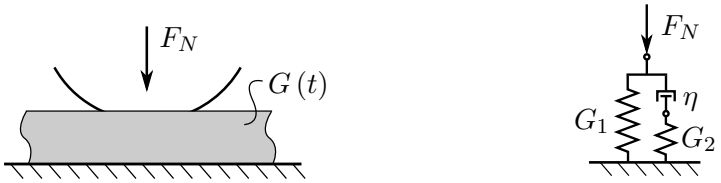

(a) rubber substrate (b) standard model

Fig. 5.15: (a) contact of rubber substrate and indenter. (b) standard rheological model for rubber

As this standard model is a parallel connection, the corresponding modules are given as:

$$G' = G_1 + G_2 \frac{(\omega\tau_r)^2}{1 + (\omega\tau_r)^2} \quad \text{and} \quad G'' = G_2 \frac{(\omega\tau_r)^2}{1 + (\omega\tau_r)^2} \ , \tag{5.1.16}$$

where $\tau_r = \frac{\eta}{G_2}$ denotes the relaxation time. For low frequencies, i.e. $\omega < G_1/\eta$, rubber behaves almost elastic with $G(t) \approx G_1$. Likewise for very high frequencies, i.e. $\omega > G_2/\eta$, rubber also behaves almost elastic with $G(t) \approx G_2$ [55]. The viscous dissipation can be neglected in both cases. In contrast, in the intermediate range, rubber behaves like a viscous fluid doing periodic loading, i.e. it exhibits high dissipation. Now, for the silicone rubber used in the experiments the viscosity is approximately $\eta = 40$ Pas [103] and the quasi-static shear-modulus is measured $G_1 = 1.7$ MPa as listed in Tab. 5.1.1. Given the speed of the linear drive of $\dot{W} = 1$ mm/s, the highest excitation frequency results to $f_0 = 0.21$ Hz what yields:

$$\frac{\omega}{G_1/\eta} = \frac{2\pi \cdot 0.21 \text{ Hz} \cdot 40 \text{ Pas}}{1.7 \text{ MPa}} \approx 3 \cdot 10^{-5} \Rightarrow G(t) \approx G_1 \ . \tag{5.1.17}$$

Thus, one can assume the rubber to behave elastic in the examined parameter range.

5.2 Experimental Rig for the Micro-Walking Effect

The experimental set-up shown in Fig. 5.16 is used to investigate the micro-walking effect. Most important components are the specimen and the substrate. The drive moves the substrate with velocity v_0 relative to the specimen. Thus, the system corresponds to the well-known moving belt model.

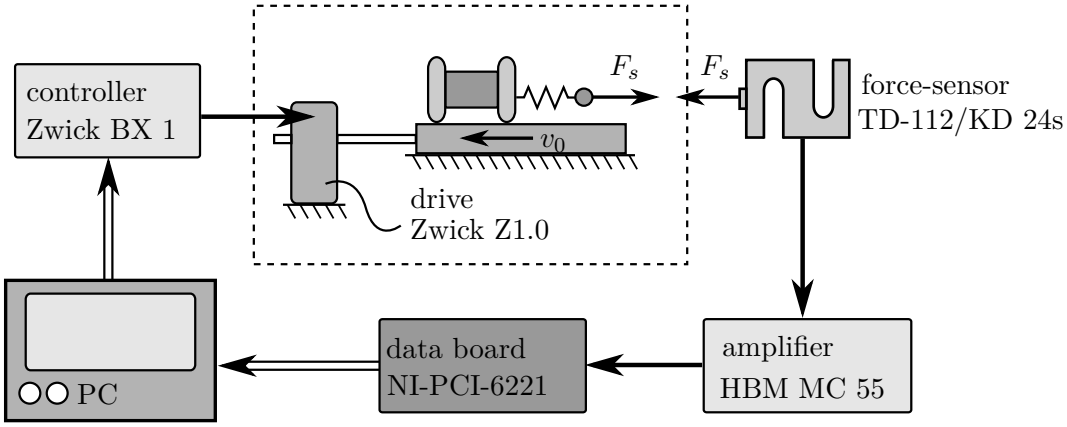

Fig. 5.16: experimental rig for the micro-walking effect with measurement chain consisting of force sensor, amplifier, data board and PC

The experimental rig is powered by an electro-mechanical testing actuator made by *Zwick GmbH & Co. KG* whose good ganging properties reduce unwanted dynamic interactions. The actuator is controlled using the controller BX-1. Straight rods act as the spring between specimen and base. The spring force F_s is measured at the base of the spring using a S-force sensor. Different sensors are used, namely the sensor TD-112 by *Yuyao Tongda Scales Co., Ltd.* and the sensor KD24s by *ME measurement systems GmbH*. The latter one has smaller dimensions and allows a larger adjustment range of the height of the base. For amplification of the sensor signal, the amplifier system MGC of the company *HBM* is used, which essentially consists of the amplifier HBM MC 55. The measured signals are fed to the PC via a measuring system with 16-bit data acquisition board, namely NI PCI-6221 by *National Instruments Corporation*, which also serves to control the drive. The sampling frequency used to measure the spring force F_s is chosen to be $f_{samp} = 4000$ Hz. This satisfies the Whittaker–Nyquist–Kotelnikov–Shannon theorem [104] as:

$$f_{samp} = 4000 \text{ Hz} > 2 \times \frac{\Omega_{exp}}{2\pi} \approx 760 \text{ Hz} \,, \tag{5.2.1}$$

where Ω_{exp} is determined from the frequency spectrum of the time response of F_s as shown in section 5.2.3. Finally, the effective coefficient of friction μ_e is computed as:

$$\mu_e = \frac{\langle F_s(t) \rangle}{\sqrt{2}\mu m g}. \tag{5.2.2}$$

5.2.1 Parameters of the Experimental Rig

The materials and the exact dimensions of the specimen and the substrate are chosen such that the dimensionless parameter combinations, which are determined with the numerical model as described in section 4.2.1 and section 4.2.2, are met as closely as possible. However, experimental feasibility leads to certain limitations as discussed below. The specimen has an hourglass shape as shown in Fig. 5.17 (a). It consists of a steel centrepiece and two contact discs made of polypropylene ($E_{PP} = 1.4$ GPa). This configuration enables a quick adjustment of the geometry and thus inertia properties. The substrate consists of smooth window glass ($E_{GS} = 90$ GPa) and has a prism shape as shown in Fig. 5.17 (b) and Fig. 5.18 (a). On the one hand, this configuration enhances the stability and parallelism of the motion of the specimen. On the other hand, the contact configuration of the experiment differs slightly from the initial theoretical model introduced in section 4.1.3. Thus, for the comparison in section 4.3.2 an extended model as described in sections 5.2.3 and appendix B.4 is used. Other dimensions and parameters of the experimental rig and the different combinations for set 1-5 are given in Tab. 5.2.1. A detailed discussion of how these parameters are determined is given below. In addition a deviation analysis is given in section 5.2.3.

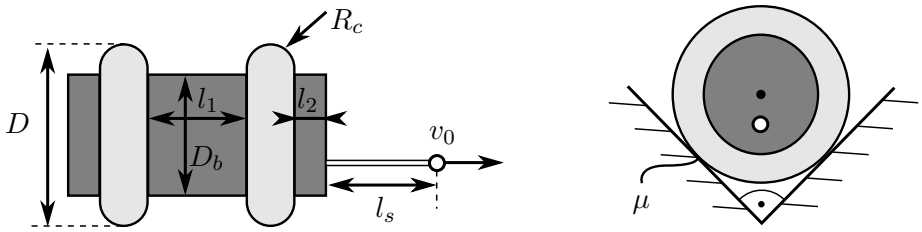

(a) lateral view (b) front view

Fig. 5.17: (a) lateral view of the hourglass-shaped specimen with dimensions. (b) front view of the specimen with prism-shaped substrate

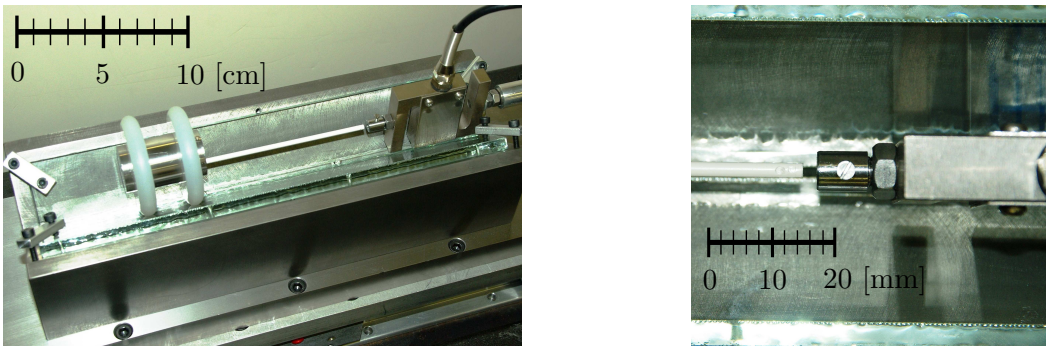

(a) experimental rig (b) mount of the spring

Fig. 5.18: (a) experimental rig for the micro-walking effect consisting of specimen and prism-shaped substrate. (b) mount of the spring at the S-force sensor with spring rod

Tab. 5.2.1: parameters of the micro-walking experimental rig for the different parameter combinations set 1-5. The numbers in brackets gives the corresponding set

parameter	symbol	value	unit
radius	R_c	5	mm
contact disc diameter	D	60	mm
body diameter	D_b	$30\,(1,2,3,4)\,/50\,(5)$	mm
model half-height	a	21.2	mm
length of centre part	l_1	$18\,(1,3,5)\,/40\,(2,4)$	mm
model half-width	b	$14\,(1,3,5)\,/25\,(2,4)$	mm
length of side-disc	l_2	5	mm
mass of specimen	m	$201\,(1,3)\,/327\,(2,4)\,/490\,(5)$	g
length of spring-rod	l_s	100	mm
friction coefficient	μ	$0.79\,(1,2)\,/0.68\,(3,4)\,/0.75\,(5)$	1
Young's modules	E_{PP}/E_{GS}	1.4/90	GPa
Poisson-ratios	ν_{PP}/ν_{GS}	0.4/0.3	1
contact diameter	D_c	1.8	mm

Contact Stiffness and Contact Diameter The contacts between specimen and substrate are modelled as linear springs with normal and tangential stiffness:

$$k_z = E^* D_c \quad \text{and} \quad k_x = G^* D_c \,. \tag{5.2.3}$$

The effective modules E^* and G^* directly depend on the materials in contact, whereas the contact diameter D_c is a function of the actual contact configuration as sketched in Fig. 5.19 (a). Hence, it depends on the state of motion of the system. In the following, different ways for the estimation of D_c are presented.

1) If the contacts are assumed to be of the Hertzian type with an average normal force $\bar{F}_N = \frac{1}{2\sqrt{2}} mg$ acting on each single contact the contact width yields:

$$D_c = \left(\frac{6 \bar{F}_N R_c}{E^*} \right) \approx 0.4 \text{ mm} \,. \tag{5.2.4}$$

One drawback of this assumption is that in fact the normal force and thus D_c change in time. In addition, it remains unclear if the contact model is chosen correctly.

2) Due to wear, the shape of the contacts will soon not resemble a Hertzian contact but a flattened ellipse with a more or less constant effective diameter as shown in Fig. 5.19 (b). Here one wear spot in the contact zone is shown. A rather crude optical estimate of the conjugate diameters of the wear spots gives:

$$D_c = 2\sqrt{ab} \approx 2 \text{ mm} \,. \tag{5.2.5}$$

But again, the question remains whether the wear spots really correspond to the visible contact zones.

3) Another way to estimate the contact stiffness is to compare the characteristic frequencies of the spring forces of the experiment and the simulation as discussed in section 5.2.3. Assuming that the simulation maps the reality sufficiently accurate, the characteristic frequencies must match. This gives the characteristic time τ as defined in equations (4.1.11) and (5.2.35) and one can compute the contact stiffness as:

$$k_x = \frac{m}{\tau^2} \,. \tag{5.2.6}$$

The contact stiffness and diameter then yield:

$$k_x = (2.2 \pm 1.5) \cdot 10^6 \text{ N/m and } D_c = (1.8 \pm 1.2) \text{ mm} \,. \tag{5.2.7}$$

The values stated in (5.2.7) are used for approximation and for the comparison of experiment and simulation in section 4.3.2 as these values resemble to the flattened elliptical contact.

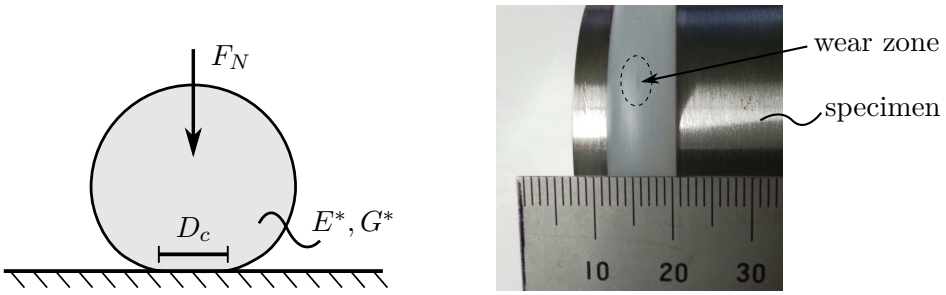

(a) model of the contact (b) wear zone at the specimen

Fig. 5.19: (a) contact of elastic body and rigid substrate with contact diameter D_c as a model of the contact zones of the between specimen. (b) contact disc with elliptical shaped wear zone

Spring Stiffness The parameter studies of the numerical model as described in section 4.2.1 show that the micro-walking effect occurs if for the dimensionless parameters κ_1 and κ_4 applies:

$$\kappa_1 = \frac{k_s}{k_x} \approx 1 \quad \text{and} \quad \kappa_4 = \frac{mg}{k_x b} \approx 10^{-4} \,. \tag{5.2.8}$$

The use of a soft spring, e.g. $k_s = 10^3$ N/m, would lead to experimental advantages as this increases the difference between the eigenfrequencies of the specimen and those of the experimental rig, i.e. drive and base frame. However, in order to fulfil (5.2.8) the

half width b would result in completely impractical values, as can be shown for typical dimensions of the experiment, e.g. $m = 100$ g, $g = 9.81$ m/s^2:

$$k_s = k_x \Rightarrow b = 10^4 \cdot \frac{mg}{k_s} \approx 10^4 \cdot \frac{1 \text{ N}}{10^3 \text{ N/m}} = 10 \text{ m} . \tag{5.2.9}$$

Instead, stiff polypropylene is used for the contact discs, such that the tangential stiffness results to $k_x = 2 \cdot 10^6$ N/m and the half width to $b = 10^{-2}$ m. In order to achieve a spring stiffness of $k_s \approx k_x$, straight rods made of fibre-reinforced plastic respectively polystyrene are used. Their corresponding Young's modules are measured on the basis of the DIN norm 178 [105] and result to:

$$E_{PS} = (3.42 \pm 0.02) \text{ GPa} , \tag{5.2.10}$$

$$E_{CF} = (176.66 \pm 2.02) \text{ GPa} . \tag{5.2.11}$$

The spring stiffness corresponds to the according longitudinal stiffness:

$$k_s = \frac{E_s A_s}{l_s} , \tag{5.2.12}$$

where A_s is the cross sectional area of the rod. Initially, the spring stiffness result to

$$k_{s-PS} = (2.42 \pm 0.14) \cdot 10^5 \text{ N/m} , \tag{5.2.13}$$

$$k_{s-SP} = 60 \text{ N/m} , \tag{5.2.14}$$

$$k_{s-CF} = (5.50 \pm 0.63) \cdot 10^6 \text{ N/m} , \tag{5.2.15}$$

where k_{s-SP} denotes the spring stiffness of the spiral spring used in section 4.3.1. This value is simply taken from the corresponding data sheet, where the uncertainty of the measurement is not given. However, the stiffness of the sensor used for determination of the spring force has to be taken into account. For the sensor KD24s the spring stiffness is $k_{KD24s} = 2 \cdot 10^7$ N/m. As it is in series with the spring, the effective spring stiffness $\tilde{k}_s$ can be determined as :

$$\tilde{k}_s = \left(\frac{1}{k_s} + \frac{1}{k_{KD24s}} \right)^{-1} , \tag{5.2.16}$$

what finally yields[1]:

$$\tilde{k}_{s-PS} = (2.38 \pm 0.14) \cdot 10^5 \text{ N/m} , \tag{5.2.17}$$

$$\tilde{k}_{s-CF} = (4.34 \pm 0.39) \cdot 10^6 \text{ N/m} . \tag{5.2.18}$$

The stiffness of the sensor TD-112 is not known. As its nominal load is higher than for the KD24s it is expected to be stiffer. Thus, according to (5.2.16) its influence is

[1]The sensor can assumed to be rigid in comparison to the spiral spring, i.e. it does not influence the stiffness in this case.

lower. In the end, the high error of measurement for the contact stiffness discussed in section 5.2.3 leads to the following rather crude estimates of the parameters κ_1:

$$\begin{aligned} \kappa_{1-PS} &= \frac{\tilde{k}_{s-PS}}{k_x} \approx 0.1 \quad && \rightarrow \text{used in set 1, 2} \ , \\ \kappa_{1-SP} &= \frac{k_{s-SP}}{k_x} \approx 10^{-4} && \rightarrow \text{used in set 3, 4} \ , \\ \kappa_{1-CF} &= \frac{\tilde{k}_{s-CF}}{k_x} \approx 2 && \rightarrow \text{used in set 5} \ . \end{aligned} \tag{5.2.19}$$

Sets 1-4 are used in the analysis of section 4.3.1 and are tabulated in Tab. 4.3.1. Set 5 is used in the comparison of experiment and simulation in section 4.3.2 and is described in Tab. 4.3.2.

5.2.2 Experimental Procedures

In order to increase the reproducibility, it is briefly described how the experiments are conducted and a few time responses of the spring force are shown. The final experimental results are given in sections 4.3.1 and 4.3.2. The experimental procedure used for detection of the time response of the spring force is as follows:

1) cleaning of the glass substrate with degreaser

2) alignment of the base and specimen and attaching of the spring

3) measuring run with desired velocity v_0

4) return run with velocity $v_0 = 15$ mm/s

The running distance is 190 mm. In order to ensure an almost stationary contact configuration, i.e. elliptical wear patches at the contact zones, about 100 runs for the running-in process are conducted after every change of the experimental set-up. In order to study a particular combination of parameters 10 to 20 iterations, i.e. measuring runs, are performed before the experimental set-up is changed. The following figures depict cut-outs of the time response of the normalized spring force F_s for the parameter set 5 as described in section 4.3.2 in Tab. 4.3.2, i.e. the maximum parameter set of the experiment. The lever arm ratio is $\kappa_8 = -0.71$. As shown in Fig. 5.20, where F_s for $v_0 = 8.33$ mm/s is given, only small oscillations occur in case that the base velocity v_0 falls below the limit velocity. If the limit velocity is exceeded, instabilities with high frequency occur, as shown in Fig. 5.21 which gives F_s for $v_0 = 33.33$ mm/s. These instabilities cause a reduction of the efficient coefficient of friction. Comparison of the close ups in Fig. 5.22 and Fig. 5.23 highlights the differences between the time responses.

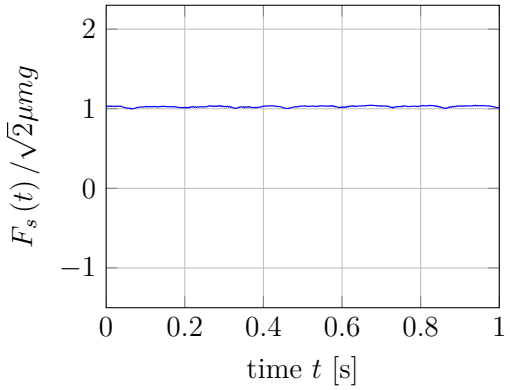

Fig. 5.20: time response of F_s for set 5 with the parameters as in Tab. 4.3.2 and $\kappa_8 = -0.71$ and $v_0 = 8.33$ mm/s

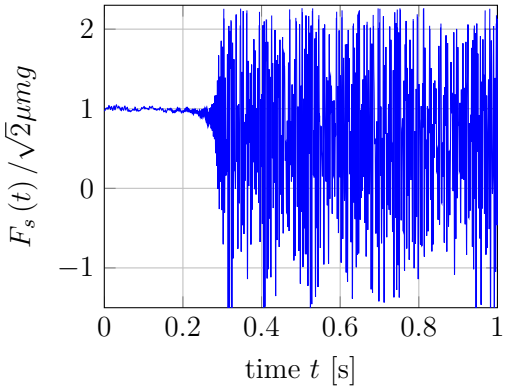

Fig. 5.21: time response of F_s for set 5 with the parameters as in Tab. 4.3.2 and $\kappa_8 = -0.71$ and $v_0 = 33.33$ mm/s

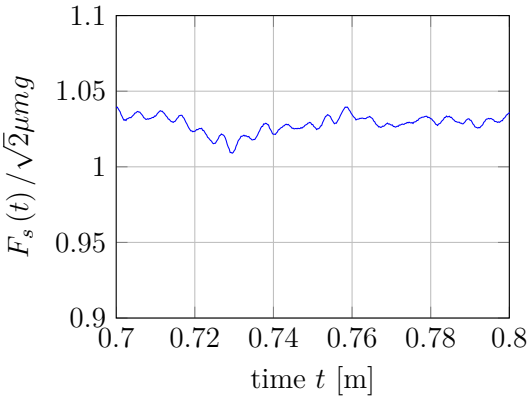

Fig. 5.22: close up of the time response of F_s for the parameters as in Tab. 4.3.2 and $\kappa_8 = -0.71$ and $v_0 = 8.33$ mm/s

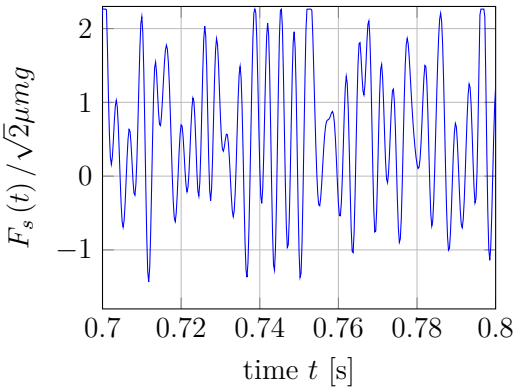

Fig. 5.23: close up of the time response of F_s for the parameters as in Tab. 4.3.2 and $\kappa_8 = -0.71$ and $v_0 = 33.33$ mm/s

5.2.3 Analysis of Deviations

Contact Configuration The geometry and contact configuration of the experiment differs from the theoretical model. This is mainly caused by the inability to replicate the two-dimensionality of the theoretical model in practice. For instance, usage of a lateral guidance in the y-direction would induce an additional friction force to the system, especially since it would theoretically have to be free of bearing clearance. However, the three dimensional experiment can be modelled as a two dimensional model that consists of three dimensional contacts. This is possible, since for symmetrical initial conditions[2],

[2]In this case the word symmetrical means that the rigid body is not rotated around the y- and z-direction and not displaced in the y-direction. This was tested by the author using a full 3-D model taking into account all 6 directions of motion.

the contact forces are symmetrical for all of the four contacts. The according equations of motion are then the same as for the theoretical model that are given in equations (4.1.16)-(4.1.19). One difference relates to the contact forces. The contact plane is inclined since the substrate is prism shaped. This leads to an additional spring deflection u_s as described in section B.4. There are four contacts spots each exhibiting its own spring deflections. But as the model is symmetrical, the two contacts on the left and on the right obtain the same contact conditions. Thus, only one contact on the left and one on the right are considered and the corresponding contact forces are doubled:

$$f_{N1/2} = 2 \cdot \kappa_2 \frac{\sqrt{2}}{2} \left(u_{n1/2} + u_{s1/2} \right) \ , \tag{5.2.20}$$

$$f_{T1/2} = 2 \cdot u_{x1/2} \ . \tag{5.2.21}$$

The equations of motion in the non-dimensional form yield:

$$x_s' = \kappa_6 \ , \tag{5.2.22}$$

$$x'' = -2u_{x1} - 2u_{x2} + \kappa_1 \left(x_s - x + \kappa_8 \varphi \right) \ , \tag{5.2.23}$$

$$z'' = -2\kappa_2 \frac{\sqrt{2}}{2} \left(u_{n1} + u_{s1} \right) - 2\kappa_2 \frac{\sqrt{2}}{2} \left(u_{n2} + u_{s2} \right) + \kappa_4 \ , \tag{5.2.24}$$

$$\begin{aligned} \varphi'' = & \frac{1}{\kappa_7} \left(-2\kappa_2\kappa_3 \frac{\sqrt{2}}{2} \left(u_{n1} + u_{s1} \right) (1 - \varphi) + 2\kappa_2\kappa_3 \frac{\sqrt{2}}{2} \left(u_{n2} + u_{s2} \right) (1 + \varphi) \right) \ , \\ & + \frac{1}{\kappa_7} \left(-2u_{x1} \left(\kappa_3^2 + \varphi \right) - 2u_{x2} \left(\kappa_3^2 - \varphi \right) - \kappa_1 \left(\kappa_3^2 \kappa_8 + \varphi \right) \left(x_s - x + \kappa_8 \varphi \right) \right) \ . \end{aligned} \tag{5.2.25}$$

As a consequence of the inclined contact plane, the effective coefficient for the experimental model must be computed as:

$$\mu_e = \frac{\langle f_s(t) \rangle}{\sqrt{2} \mu \kappa_4} \ . \tag{5.2.26}$$

Hence, it corresponds to μ_e of the experiment as defined in equation (5.2.2):

$$\mu_e = \frac{\langle F_s(t) \rangle}{\sqrt{2} \mu m g} . \tag{5.2.27}$$

Deviation of the Parameter Range Some of the parameters can simply be measured geometrically. This is the case for the parameters κ_3, κ_7 and κ_8. For these, the deviation between the *real* values of the experiment and the calculated ones is expected to be such small that it can be neglected. The microscopic friction μ can be determined experimentally using the test rig and base velocities below the threshold for the instability. Different batches for the material of the contact disc result in different values for the microscopic friction:

$$\begin{aligned} \mu &= 0.79 \pm 0.01 \quad \rightarrow \text{used in set 1, 2} \ , \\ \mu &= 0.68 \pm 0.03 \quad \rightarrow \text{used in set 3, 4} \ , \\ \mu &= 0.75 \pm 0.03 \quad \rightarrow \text{used in set 5} \ . \end{aligned} \tag{5.2.28}$$

Sets 1-4 are used in the analysis of section 4.3.1 and are tabulated in Tab. 4.3.1. Set 5 is used in the comparison of experiment and simulation in section 4.3.2 and is described in Tab. 4.3.2. The value of κ_2 can only be estimated as the real contact configuration remains unknown. This is not a problem, since the influence of κ_2 is only minor as shown in section 4.2.1. Assuming an approximately circular contact area and considering the parameters of Tab. 5.2.1, the Hertzian contact theory yields the parameter κ_2 as:

$$\kappa_2 \approx 1.33 \; . \tag{5.2.29}$$

In contrast the remaining parameters κ_1 and κ_6 are of great influence as shown in section 4.2.1. Both depend on the *unknown* tangential contact stiffness k_x. One way to estimate k_x, is to determine the non-dimensional time:

$$\tau = \sqrt{\frac{m}{k_x}} \Rightarrow k_x = \frac{m}{\tau^2} \; . \tag{5.2.30}$$

For this purpose the time response of the normalized spring force of both, experiment and simulation, is determined. Afterwards, the corresponding frequency spectra S_s [99] are computed. For the simulation S_s is computed as:

$$S_{s-sim} = \frac{1}{T} \int_0^T \frac{f_s\,(t)}{\sqrt{2}\mu\kappa_4} \exp\left(-i\Omega t\right) \mathrm{d}t \; , \tag{5.2.31}$$

and for the experiment it is computed as:

$$S_{s-exp} = \frac{1}{T} \int_0^T \frac{F_s\,(t)}{\sqrt{2}\mu m g} \exp\left(-i\Omega t\right) \mathrm{d}t \; . \tag{5.2.32}$$

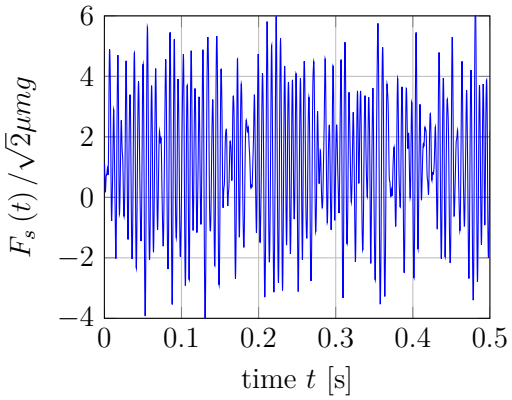

Fig. 5.24: time response of the spring force F_s for the parameter set 5

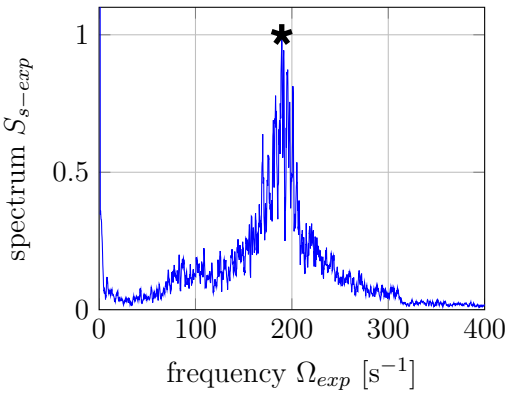

Fig. 5.25: frequency spectrum S_{s-exp} of F_s for the for the parameter set 5

Figure 5.24 gives the time response of F_s of the experiment for the parameter set:

$$\text{set 5:} \quad \kappa_{1-8} = \left(2, 1.33, 1.51, 2 \cdot 10^{-4}, 0.75, 1.6 \cdot 10^{-3}, 1.77, -0.47\right) . \tag{5.2.33}$$

Figure 5.25 shows the corresponding frequency spectra S_s where the star denotes the characteristic frequency Ω_{exp}. Assuming that the simulation maps the reality sufficiently accurate, the frequencies must match, i.e. $\Omega_{sim} = \Omega_{exp}$. In case of the simulation, the characteristic frequency Ω_{sim} is given as the computed non-dimensional frequency ω_{sim} divided by the characteristic time τ:

$$\Omega_{sim} = \frac{\omega_{sim}}{\tau} \, . \tag{5.2.34}$$

Thus, the characteristic time is determined as:

$$\frac{\omega_{sim}}{\tau} = \Omega_{sim} = \Omega_{exp} \Rightarrow \tau = \frac{\omega_{sim}}{\Omega_{exp}} \, . \tag{5.2.35}$$

In order to determine τ, 10 time responses of the force for different base velocities are measured and the characteristic frequencies are computed. The results are shown in Fig. 5.26 and Fig. 5.27. The mean frequencies result to:

$$\Omega_{exp} = (240 \pm 62) \text{ Hz} \quad \text{and} \quad \omega_{sim} = 0.1 \pm 0.006 \, , \tag{5.2.36}$$

what yields the characteristic time as:

$$\tau = (4.7 \pm 1.5) \cdot 10^{-4} \text{ s} \, . \tag{5.2.37}$$

Finally, under the assumption that the contact stiffness is the same for all velocities, the contact stiffness can be identified as:

$$k_x = \frac{m}{\tau^2} = m \left(\frac{\Omega_{exp}}{\omega_{sim}} \right)^2 = (2.2 \pm 1.5) \cdot 10^6 \text{ N/m} \, . \tag{5.2.38}$$

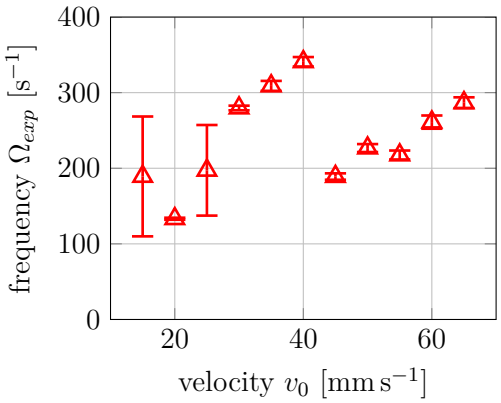

Fig. 5.26: characteristic frequency Ω_{exp} as a function of the velocity v_0

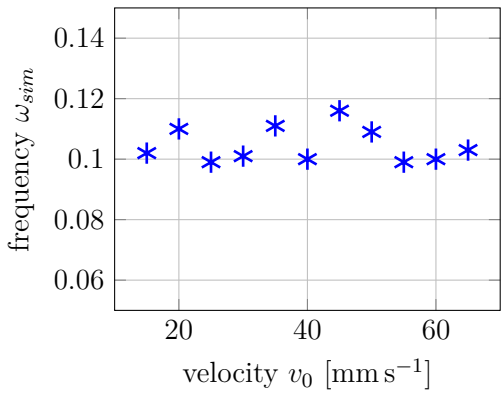

Fig. 5.27: characteristic frequency ω_{sim} as a function of the velocity v_0

It shows that the absolute error of measurement is high. This is caused by the highly varying frequencies of the experiments as depicted in Fig. 5.26. One reason for this is

the changing contact configuration as discussed in section 5.2.1. Firstly, the contact stiffness changes with the load as in the Hertzian contact. Secondly, there is a constant wear that changes the contact area. Thus, the resulting stiffness of (5.2.38) is not more than an indicator for the magnitude of the real contact stiffness, which obviously changes for the different test runs. Additionally, it remains unclear if the rest of the parameters is estimated correctly. Furthermore, the parameters κ_1 and κ_6 used in the simulations are determined in advance on basis of an educated guess for k_x. One can conclude that the model at least captures the basic effects of the experiment and shows the correct magnitudes. Figure 5.28 gives a comparison of the time response of the normalized measured force F_s and the force of the simulation model f_s for parameter set 5. It shows that the amplitudes match relatively good.

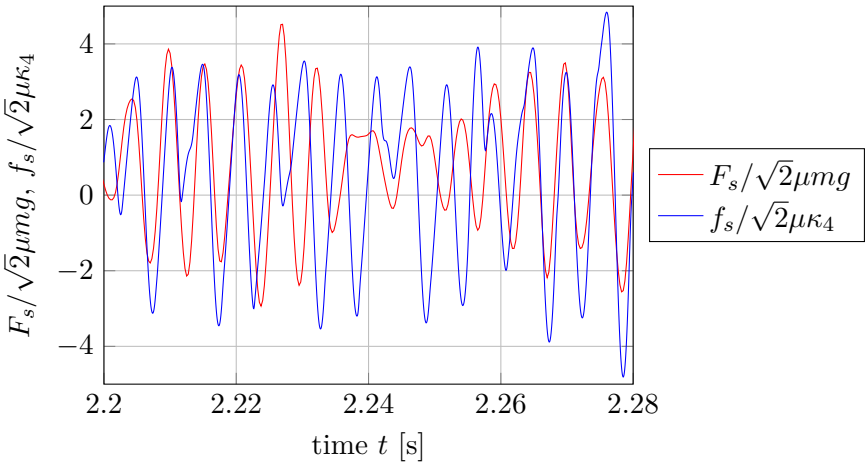

Fig. 5.28: time response of the spring force for the experiment and simulation for the parameter set 5. The time of the simulation is computed with the characteristic time τ

Influence of the Spring A more accurate modelling would characterize the connecting element between base and specimen as a beam consisting of a stiffness that considers all of the three degrees of motion of the model. It is to be determined whether these unwanted influences can be neglected. For this purpose the model shown in Fig. 5.29 is chosen that consists of an Euler-Bernoulli beam that is connected to a rigid mass that is supported by a spring with the contact stiffness k_z. As $k_z \approx k_x \approx k_s$ applies in the reduction regime, the contact stiffness corresponds to the longitudinal stiffness of the beam k_s as in (5.2.12). The well-known beam theory gives the elastic force F_{bZ} and the moment $M_{b\Phi}$ that act from the beam on the mass [106]:

$$F_{bZ} = \frac{3E_sI_s}{l_s^3} w\left(l_s\right) \quad \text{and} \quad M_{b\Phi} = \frac{E_sI_s}{l_s} w'\left(l_s\right) \ . \tag{5.2.39}$$

Here $w\left(l_s\right)$ and $w'\left(l_s\right)$ give the displacement and the rotation of the beam at $x = l_s$.

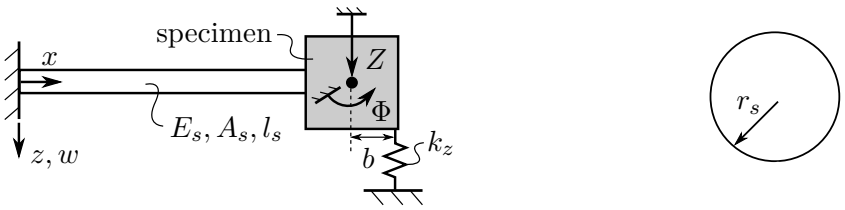

(a) beam model (b) cross section

Fig. 5.29: (a) beam model of the connection element of the system. (b) cross section of the beam

The other important loads are the force F_{cZ} and the moment $M_{c\Phi}$ of the contact:

$$F_{cZ} = k_z Z = k_s Z \quad \text{and} \quad M_{c\Phi} = k_z b^2 \Phi = k_s b^2 \Phi \; . \tag{5.2.40}$$

With (5.2.39), (5.2.40) and (5.2.12) the ratios of the forces and moments yield:

$$\frac{F_{bZ}}{F_{cZ}} = \frac{\frac{3E_s I_s}{l_s^3} w\left(l_s\right)}{\frac{E_s A_s}{l_s} Z} \quad \text{and} \quad \frac{M_{b\Phi}}{M_{c\Phi}} = \frac{\frac{E_s I_s}{l_s} w'\left(l_s\right)}{\frac{E_s A_s}{l_s} b^2 \Phi} \; . \tag{5.2.41}$$

As $w\left(l_s\right) = Z$ and $w'\left(l_s\right) = \Phi$ as well as $A_s = r_s^2$ and $I_s = \frac{\pi}{4} r_s^2$ this gives:

$$\frac{F_{bZ}}{F_{cZ}} = \frac{3}{4} \left(\frac{r_s}{l_s}\right)^2 \quad \text{and} \quad \frac{M_{b\Phi}}{M_{c\Phi}} = \frac{1}{4} \left(\frac{b}{r_s}\right)^2 \; . \tag{5.2.42}$$

Finally, with $r_s = 1 \cdot 10^{-3}$ mm, $l_s = 1 \cdot 10^{-1}$ m and $b = 1 \cdot 10^{-2}$ m this yields:

$$\frac{F_{bZ}}{F_{cZ}} \approx 10^{-4} \quad \text{and} \quad \frac{M_{b\Phi}}{M_{c\Phi}} \approx 10^{-2} \; . \tag{5.2.43}$$

Thus, one can conclude that the influence of the connection element on the vertical displacement and the rotation can be neglected in the modelling, as the corresponding loads are by orders lower than the contact forces and moments. Therefore, the bending and torsional-stiffness of the connection element is not considered and it can be modelled as a simple spring.

Chapter 6

Conclusion and Outlook

6.1 Conclusion

Two principally different models have been introduced to examine the influence of microscopic slip on the macroscopic behaviour of mechanical systems with friction. Firstly, the oscillatory rolling contact, which corresponds to a Hertzian contact with time varying contact area and pressure distribution. Secondly, the micro-walking machine, which corresponds to a rigid slider with several independent contact spots.

6.1.1 Shakedown and Ratcheting in Incomplete Contacts

As generic models for incomplete contacts, the oscillating rolling contacts with constant load regime F_T and F_N have been introduced. Basic assumptions are dry friction of the Coulomb type with constant coefficient of friction μ and linear elastic material behaviour. Additionally, the systems are assumed to be quasi-static and from an uncoupled type, i.e. Dundur's constant $\beta = 0$. Thus, variations in the normal force will not induce any tangential displacement and vice versa. The system resembles a tangentially loaded contact problem from the Hertzian type that is superposed by a slight oscillatory rolling of the upper body. This rolling resembles to a rocking motion, i.e. a back and forth movement of the point of application of the normal force as in the rocking punch examined by Mugadu et al. [27]. In consequence, the pressure distribution and the contact region are varied within every cycle of the rolling. In the analysis, the MDR [67], the CONTACT simulation software [88], classical analytical contact mechanics [56, 55] and experimental test rigs have been used. Depending on the system parameters two distinct cases can occur.

Shakedown In the first few periods the rolling leads to partial slip and increases the rigid body displacement of the substrate. In case that the rolling amplitude w and the tangential force f_T fall below the so-called shakedown limits, the system reaches a new equilibrium and the centre of the initial contact area remains in a state of stick. During the transient, the traction is increased until a residual force is formed that balances

the macroscopic tangential force. This process is referred to as a frictional shakedown [25, 26]. In the experiment, the shakedown state is reached after 10-12 periods of rolling. For all three cases that have been considered, i.e. spherical roller with parallel and perpendicular alignment of load and oscillation and cylindrical roller with parallel alignment, the shakedown displacement and the shakedown limits have been derived. The former describes the new equilibrium state. The latter gives the maximal tangential force for a given rolling amplitude for which a safe shakedown occurs and vice versa. In all three cases it turns out that shakedown is accompanied with a significant reduction of the tangential load capacity. The reduction in all three cases is approximately:

$$f_{T,lim} \approx 1 - w_{lim} \; . \tag{6.1.1}$$

This effect must be considered in the design of force locked connections in which the contact is incomplete and the pressure distribution varies in the described manner. Comparison of the three cases shows that spherical contacts can bear higher tangential loads than cylindrical ones. In addition, the parameter range of the shakedown displacement is narrower for the cylindrical case, i.e. the final shakedown displacements differ only slightly for different f_T and w.

Ratcheting In case that the shakedown limits are exceeded, an effect called ratcheting occurs. The alternating slip processes cover the complete initial contact area and shakedown is no more possible. Depending on the actual rolling direction one side of the contact sticks while the other slips. This accumulated displacement results in a rigid body motion referred to as ratcheting or walking [27, 28, 29]. Approximation functions for the incremental slip per period as a function of the tangential load and the rolling amplitude have been derived. These are in good agreement with the experimental results and show qualitatively good agreement with the results for the walking of the rocking punch [27]. The ratcheting effect can be used for the generation and control of small displacements in case that an increase of the tangential loading is not possible or high accuracy is needed as in MEMS. Comparison shows that the incremental displacement is highest for the spherical contact with perpendicular setting of load and rolling and lowest for the cylindrical setting.

The results of the different methods show good agreement. The MDR [67] enables to deduce the analytical form of the shakedown state and the shakedown limits. This would have been almost impossible using classical contact mechanics as for instance the Catteneo-Mindlin approach [59, 60] or the Ciavarella-Jäger principle [58, 62]. This is because both, contact area and traction distribution are not known and are the product of a transient process. However, comparison with the experiments and the 3-D CONTACT simulation indicates that the MDR results are only qualitatively correct. The slight deviation that occurs is caused by the missing rotational symmetry of the contact configuration after shakedown, what violates one basic assumption of the MDR. Nevertheless, the results show that the MDR has again proven to be a very suitable method for the analytical description and simulation of frictional contacts.

6.1.2 Dynamic Influences on Sliding Friction

The so called micro-walking machine is introduced in order to study the system behaviour in case that the tangential load is sufficient to induce gross sliding. It consists of a rigid body with several contact spots that are assumed to be linear elastic and independent from one another. Again, dry friction of the Coulomb type is assumed with a constant coefficient of friction μ and no distinction between static and kinetic case. The system takes into account spatial variation of stick- and slip zones and contact forces, thereby enabling micro-walking of the specimen. This characterizes a dynamic mode in which the system travels most of the forward motion while the normal forces in the contacts are low in comparison to the average value. This causes a reduction of the effective coefficient of friction, i.e. a lower apparent macroscopic frictional resistance. For the analysis numerical simulations and an experimental rig have been used.

Parameters of Influence In a first step, parameter combinations are identified for which a significant reduction occurs. The results indicate that a reduction is induced if the stiffness of the excitation and the contact stiffness are comparable in size. In addition, the friction decreases with increasing velocity, increasing microscopic friction and increasing coupling between rotational moment and friction forces. These results are consistent with those gained with more or less comparable models [10, 47, 50].

Vanishing Frictional Resistance The maximal reduction is 98 % in theory and 73 % in the experiments. A further analysis of the results shows that the reduction is caused by self-excited oscillations that are induced by the coupling of the different degrees of motion. The excitation causes a rotation of the rigid body which increases the contact forces and induces oscillations in the vertical direction. This instability is characterized by a microscopic jumping of the rigid body with released contacts that is in strong correlation with the lateral motion: low or zero contact forces coincide with a fast forward motion of the rigid body. In addition, the alternation between storage and motion phase is identified as the prerequisite for the characteristic jumping and fast forward movement. The reduction increases with increasing velocity, increasing lever arm of the excitation and with increasing microscopic friction as all of these effects support the instability, i.e. increase the amplitude of the vertical oscillations. However, the vertical amplitudes in the reduction range are of the order of the static deflection, i.e. the self-excited oscillations are from a microscopic character. Taken together, the model shows that micro-vibrations play an important role for the dynamic influences on the effective frictional resistance of systems that exhibit apparently smooth sliding. In these systems, the experimentally observed dependency of the frictional resistance on dynamic quantities might be explained by microscopic effects that are influenced by macroscopic system features such as the stiffness or the geometry. One example for this being the rate weakening of the friction coefficient. The model shows that this effect can be explained to some extent by dynamic instabilities that simply increase with the sliding velocity. This is particularly important for the design of tribometers.

The results of the simulations give a clear but also strict guideline for the parameter range that needs to be adjusted if one wants to induce this reduction through dynamic instabilities. Both, the design-phase of the experimental rig and the experiments itself show that this parameter range is narrow and hard to reach. For instance, matching the non-dimensional parameters in reality is very challenging. Furthermore, a change of the scaling of the model would change the non-dimensional parameters, due to cross influences and some constant parameters as for instance the gravitational acceleration. Thus, it remains vague to what extent the proposed effect occurs in practical systems. However, the results provide a solid starting point for further research and development of applications in technical systems.

6.1.3 The Interplay of System Dynamics and Friction

The first model explains the failure of force locked connections under the influence of oscillations in the pressure distribution. The second model shows that micro-vibrations can be responsible for the dynamic influences on the effective frictional resistance of systems that exhibit apparently smooth sliding. Although both systems are relatively different in terms of basic assumptions (nominally static vs. dynamic) and type of analysis (analytic derivations vs. numerical experiments) the results are fairly connected to each other. As shown in Fig. 6.1, the different phenomena can be imagined as neighbouring scenarios. The range of scenarios starts on the left with the shakedown effect. In this range, a system that is subjected to oscillating loads will reach a new equilibrium after some periods, i.e. it will remain stable as long as both tangential force and oscillation amplitude fall below the shakedown limits. If these are exceeded, the system will enter the next scenario. Ratcheting starts which is an accumulation of micro-slip that alternately affects the whole contact area and leads to a continuing rigid body motion. If the instability limit is exceeded, the system enters the next scenario: the micro-walking range. Here, self-excited oscillations occur that lead to temporarily released contacts. The instability limit depends on different system properties such as the sliding velocity, stiffness, mass and geometry.

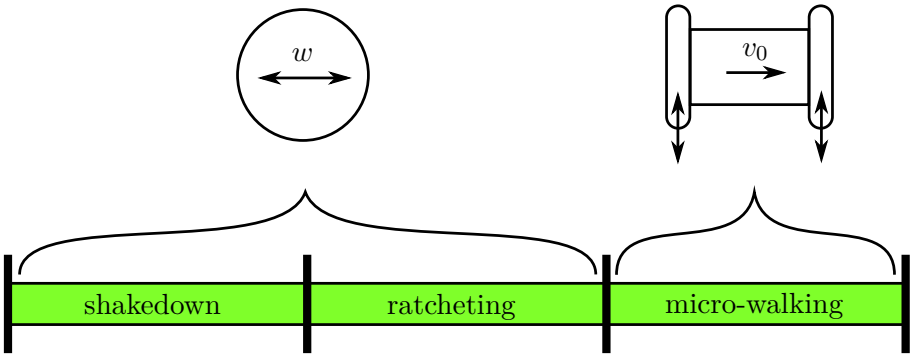

Fig. 6.1: scenarios in mechanical systems with friction and oscillations

The consequences of the different effects are very similar. In the case of shakedown occurs a significant reduction of the maximal tangential load capacity. In consequence, the force that is needed to induce a rigid body motion in the case of ratcheting is lower than expected, i.e. the effective frictional resistance is reduced. This is the same effect as in the case of micro-walking. Thus, as stated in the introduction of this work all of these effects strongly influence the macroscopic behaviour of the system although they occur at the micro-scale. In the model for shakedown and ratcheting in incomplete contacts, the oscillations are externally driven. In contrast, in the micro-walking machine the oscillations are self-excited. Consequently, throughout this work the different effects are considered separately. However, a mechanical system with friction that is subjected to oscillations in the contact area or contact stresses can successively or simultaneously exhibit all these effects. Therefore, future research should combine the two models to give further insights to the subject of dynamic influences in mechanical systems with friction.

6.2 Outlook

In addition to a possible combination of the two models proposed in this work, there exist several other promising extensions that are briefly described in the following section.

6.2.1 Shakedown and Ratcheting in Incomplete Contacts

Shakedown in Contacts of Rough Surfaces Since all technical surfaces are rough to some extent, one interesting extension of the work is to consider shakedown and ratcheting in the contact of rough surfaces. Starting point is the tangentially loaded contact between an elastic half-space and a rigid rough indenter. Instead of oscillatory rolling on can consider rocking of the contacting bodies that is induced by a moving normal force as in the rocking and walking punch of Mugadu et al. [27]. The MDR enables to map the initial 3D system to a one-dimensional system of independent elements [67] and has proven to be a suitable instrument for the modelling of fractal rough surfaces [70, 71]. For this reason, one can expect that also shakedown and ratcheting in rough surfaces can be simulated using the MDR.

Shakedown for Further Contact Geometries Further research is needed to examine other forms of smooth rolling bodies as cones or ellipsoids. Although it remains vague whether an analytical description of the shakedown limits of these systems can be achieved, it is certainly possible to conduct 3D simulations using the CONTACT model and to conduct experiments using the rolling body test rig.

Interaction of Parameters Especially for technical applications it would be interesting to consider the interaction of different parameters. For example, the oscillatory rolling might be superposed by varying normal and tangential forces. Or the influence of the alignment of load and oscillation for angles between 0 and $\pi/2$ can be considered.

6.2.2 Dynamic Influences on Sliding Friction

Extended Experiments As the theoretical maximal reduction of the frictional resistance is not reached, further development of the experimental test rig is needed in order to match the maximal range of the non-dimensional parameters. One possibility is to identify other maximal parameter combinations that are easier to reach in practice. Another possibility is to attach some kind of guide-way such that the two-dimensional character of the theoretical model can be reproduced. For this, a plane substrate instead of a prism shaped substrate needs to be used.

Contribution of Instability Mechanisms The simulations show that several mechanisms contribute to the reduction effect: vibrations in the normal direction, synchronization of tangential and normal motion and characteristic alternation between storage and motion phase. Attempts should be made to reveal which of the proposed effects contributes mostly to the reduction. For this purpose, models and experiments must be designed where certain effects can be switched off. For instance, one can avoid jumping of the specimen using a vertical guidance in order to examine the influence of the rotation.

Practical Guidelines The origin for the work on the dynamic influences of the frictional resistance is the poor reproducibility of measurements of friction coefficients. Therefore, the results should be revised in order to give practical guidelines for the design of tribometers. This can be followed by analysis and improvement of an existing tribometer with regard to its dynamic properties.

Measurement of Normal Oscillations The only dynamic quantity that is measured in the experiments is the time response of the spring force at the base. Although, the time responses of the spring forces of simulation and experiment match relatively good, it would be an important extension to measure the normal translation of the rigid body in order to compare it to the simulation results. Especially, since in accordance to many other authors [39, 40] the normal oscillations are responsible for the reduction effect. The experimental set-up makes it easy to measure the normal displacement as the mean position of the rigid body is constant and the substrate is moved. For this, the laser vibrometer used in the rolling body experiments can be applied to the micro-walking machine test rig.

Parameters The DoE analysis indicates that certain parameters deserve further analysis as they have a significant impact on the frictional resistance. For instance, increasing ratio of height and width of the specimen increases the friction. For this purpose, also instability analysis can be used, where one considers perturbations of the steady sliding solutions.

References

[1] G. Amontons. *De la Resistance Cause'e Dans la Machines*. Memoire de l'Académie Royale des Sciences, Paris, 1699.

[2] C. A. Coulomb. *Théorie des Machines Simples*. Bachelier, Paris, 1821.

[3] F. P. Bowden and D. Tabor. *The Friction and Lubrication of Solids*. Clarendon Press, Oxford, 1950.

[4] E. Rabinowicz. *Friction and Wear of Materials*. Wiley, 1965.

[5] P. J. Blau. The Significance and Use of the Friction Coefficient. *Tribology International*, 34(9):585–591, 2001.

[6] E. Popova and V. L. Popov. The Research Works of Coulomb and Amontons and Generalized Laws of Friction. *Friction*, 3(2):183–190, June 2015.

[7] J. H. Dieterich. Time-Dependent Friction and the Mechanics of Stick-Slip. *Pure and Applied Geophysics*, 116(4–5):790–806, 1978.

[8] R. Stribeck. Kugellager für Beliebige Belastungen. *Zeitschrift des Vereins Deutscher Ingenieure*, 45(3):73–79, 1901.

[9] J. T. Oden and J. A. C. Martins. Models and Computational Methods for Dynamic Friction Phenomena. *Computer Methods in Applied Mechanics and Engineering*, 52(1–3):527–634, 1985.

[10] J. A. C. Martins, J. T. Oden, and F. M. F. Simões. A Study of Static and Kinetic Friction. *International Journal of Engineering Science*, 28(1):29–92, 1990.

[11] K.F. Chung and K.H. Ip. Finite Element Modeling of Bolted Connections Between Cold-Formed Steel Strips and Hot Rolled Steel Plates Under Static Shear Loading. *Engineering Structures*, 22(10):1271–1284, 2000.

[12] C. T. McCarthy, M. A. McCarthy, W. F. Stanley, and V. P. Lawlor. Experiences with Modeling Friction in Composite Bolted Joints. *Journal of Composite Materials*, 39(21):1881–1908, 2005.

[13] B. Li, S. N. Melkote, and S. Y. Liang. Analysis of Reactions and Minimum Clamping Force for Machining Fixtures with Large Contact Areas. *The International Journal of Advanced Manufacturing Technology*, 16(2):79–84, 2000.

[14] J. D. Booker, C. E. Truman, S. Wittig, and Z. Mohammed. A Comparison of Shrink-Fit Holding Torque Using Probabilistic, Micromechanical and Experimental Approaches. *Proceedings of the Institution of Mechanical Engineers, Part B: Journal of Engineering Manufacture*, 218(2):175–187, 2004.

[15] R. L. Burguete and E. A. Patterson. Comparison of Numerical and Experimental Analyses for Contact Problems Under Normal and Tangential Loads. *Proceedings of the Institution of Mechanical Engineers, Part G: Journal of Aerospace Engineering*, 215(2):113–123, 2001.

[16] H. Murthy, G. Harish, and T. N. Farris. Efficient Modeling of Fretting of Blade/Disk Contacts Including Load History Effects. *Journal of Tribology*, 126(1):56–64, 2004.

[17] C. J. Hartwigsen, Y. Song, D. M. Mc Farland, L. A. Bergman, and A. F. Vakakis. Experimental Study of Non-Linear Effects in a Typical Shear Lap Joint Configuration. *Journal of Sound and Vibration*, 277(1-2):327–351, 2004.

[18] M. Z. Huq and J. P. Celis. Fretting Fatigue in Alumina Tested Under Oscillating Normal Load. *Journal of the American Ceramic Society*, 85(4):986–988, 2002.

[19] D. Nowell, D. Dini, and D.A. Hills. Recent Developments in the Understanding of Fretting Fatigue. *Engineering Fracture Mechanics*, 73(2):207–222, 2006.

[20] C. M. Churchman and D. A. Hills. General Results for Complete Contacts Subject to Oscillatory Shear. *Journal of the Mechanics and Physics of Solids*, 54(6):1186–1205, 2006.

[21] N. Antoni, Q.-S. Nguyen, J.-L. Ligier, P. Saffré, and J. Pastor. On the Cumulative Microslip Phenomenon. *European Journal of Mechanics - A/Solids*, 26(4):626–646, 2007.

[22] J. A. König. *Shakedown of Elastic-Plastic Structures*. Elsevier, 2012.

[23] C. M. Churchman, A. M. Korsunsky, and D. A. Hills. The Application of Plasticity Principles to Friction. *The Journal of Strain Analysis for Engineering Design*, 41(4):323–328, 2006.

[24] E. Melan. Theorie Statisch Unbestimmter Systeme aus Ideal-Plastischem Baustoff. *S.-B. Akad. Wiss. Wien. Math.-nat. Kl. II a*, 145:195–218, 1936.

[25] A. Klarbring, M. Ciavarella, and J.R. Barber. Shakedown in Elastic Contact Problems with Coulomb Friction. *International Journal of Solids and Structures*, 44:8355–8365, 2007.

[26] J. R. Barber, A. Klarbring, and M. Ciavarella. Shakedown in Frictional Contact Problems for the Continuum. *Comptes Rendus Mecanique*, 336(1-2):34–41, 2008.

[27] A. Mugadu, A. Sackfield, and D. A. Hills. Analysis of a Rocking and Walking Punch–Part I: Initial Transient and Steady State. *ASME Journal of Applied Mechanics*, 71(2):225–233, 2004.

[28] D. Nowell. Analysis of a Rocking and Walking Punch–Part II: General Numerical Solution Using Quadratic Programming. *ASME Journal of Applied Mechanics*, 71(2):234–239, 2004.

[29] M. Ciavarella. On the Rocking and Walking Flat Punch: Effect of Elastic Dissimilarity. *Tribology International*, 83:130–138, 2015.

[30] Bo Persson. *Sliding Friction: Physical Principles and Applications*. Springer, Berlin, Heidelberg, 2000.

[31] K. Shin, M. J. Brennan, J. E. Oh, and C. J. Harris. Analysis of Disc Brake Noise Using a Two-Degree-of-Freedom Model. *Journal of Sound and Vibration*, 254(5):837–848, 2002.

[32] K. Liu and E. Bamba. Analytical Model of Sliding Friction in an Overrunning Clutch. *Tribology International*, 38(2):187–194, 2005.

[33] O. Bilkay and O. Anlagan. Computer Simulation of Stick-Slip Motion in Machine Tool Slideways. *Tribology International*, 37(4):347–351, 2004.

[34] S. C. Scholes, S. M. Green, and A. Unsworth. The Wear of Metal-on-Metal Total Hip Prostheses Measured in a Hip Simulator. *Proceedings of the Institution of Mechanical Engineers, Part H: Journal of Engineering in Medicine*, 215(6):523–530, 2001.

[35] C. W. McCutchen. The Frictional Properties of Animal Joints. *Wear*, 5(1):1–17, 1962.

[36] Christopher H. Scholz. Earthquakes and Friction Laws. *Nature*, 391(6662):37–42, 1998.

[37] V. Lampaert, F. Al-Bender, and J. Swevers. Experimental Characterization of Dry Friction at Low Velocities on a Developed Tribometer Setup for Macroscopic Measurements. *Tribology Letters*, 16(1):95–105, 2004.

[38] E. J. Berger, M. R. Begley, and M. Mahajani. Structural Dynamic Effects on Interface Response: Formulation and Simulation Under Partial Slipping Conditions. *ASME Journal of Applied Mechanics*, 67(4):785–792, 2000.

[39] D. M. Tolstoi. Significance of the Normal Degree of Freedom and Natural Normal Vibrations in Contact Friction. *Wear*, 10(3):199–213, 1967.

[40] D. Godfrey. Vibration Reduces Metal to Metal Contact and Causes an Apparent Reduction in Friction. *ASLE Transactions*, 10(2):183–192, 1967.

[41] A. A. Polycarpou and A. Soom. Boundary and Mixed Friction in the Presence of Dynamic Normal Loads: Part I: System Model. *Journal of Tribology*, 117:255–260, 1995.

[42] A. A. Polycarpou and A. Soom. Boundary and Mixed Friction in the Presence of Dynamic Normal Loads. II: Friction Transients. *Journal of Tribology*, 117:261–266, 1995.

[43] W. W. Tworzydlo and O. N. Hamzeh. On the Importance of Normal Vibrations in Modeling of Stick Slip in Rock Sliding. *Journal of Geophysical Research: Solid Earth*, 102(B7):15091–15103, 1997.

[44] D. P. Hess and A. Soom. Normal and Angular Motions at Rough Planar Contacts During Sliding With Friction. *Journal of Tribology*, 114(3):567–578, 1992.

[45] E. J. Berger. Friction Modeling for Dynamic System Simulation. *Applied Mechanics Reviews*, 55(6):535–577, 2002.

[46] W. W. Twozydlo, E. B. Becker, and J. T. Oden. Numerical Modeling of Friction-Induced Vibrations and Dynamic Instabilities. *Applied Mechanics Reviews*, 47(7):255–274, 1994.

[47] G. G. Adams. Self-Excited Oscillations in Sliding With a Constant Friction Coefficient - A Simple Model. *Journal of Tribology*, 118:819–823, 1996.

[48] M. Comninou and J. Dundurs. Can Two Solids Slide Without Slipping? *International Journal of Solids and Structures*, 14(4):251–260, 1978.

[49] G. G. Adams. Self-Excited Oscillations of Two Elastic Half-Spaces Sliding With a Constant Coefficient of Friction. *ASME Journal of Applied Mechanics*, 62(4):867–872, 1995.

[50] G. G. Adams. Steady Sliding of Two Elastic Half-Spaces with Friction Reduction due to Interface Stick-Slip. *ASME Journal of Applied Mechanics*, 65(2):470–475, 1998.

[51] H. Storck, W. Littmann, J. Wallaschek, and M. Mracek. The Effect of Friction Reduction in Presence of Ultrasonic Vibrations and Its Relevance to Travelling Wave Ultrasonic Motors. *Ultrasonics*, 40(1-8):379–383, 2002.

[52] D. A. Hills, D. Nowell, and A. Sackfield. *Mechanics of Elastic Contacts*. Butterworth-Heinemann Limited, 1993.

[53] J. Dundurs. Discussion: Edge-Bonded Dissimilar Orthogonal Elastic Wedges Under Normal and Shear Loading (Bogy, D. B., Journal of Applied Mechanics, 35, pp. 460–466, 1968). *ASME Journal of Applied Mechanics*, 36(3):650–652, 1969.

[54] J. R. Barber. *Elasticity*, volume 172 of *Solid Mechanics and Its Applications*. Springer Netherlands, Dordrecht, 2010.

[55] V.L. Popov. *Contact Mechanics and Friction: Physical Principles and Applications*. Springer, Berlin, Heidelberg, 2010.

[56] K. L. Johnson. *Contact Mechanics*. Cambridge University Press, 1987.

[57] H. Hertz. Über die Berührung Fester Elastischer Körper. *Journal für die Reine und Angewandte Mathematik*, 92:156–171, 1881.

[58] M. Ciavarella. Tangential Loading of General Three-Dimensional Contacts. *ASME Journal of Applied Mechanics*, 65(4):998–1003, 1998.

[59] C. Cattaneo. Sui Contatto di Due Corpi Elastici: Distribuzione Locale Degli Sforzi. *Rendiconti dell'Accademia Nazionale dei Lincei*, 27:342–348, 434–436, 474–478, 1938.

[60] R. D. Mindlin. Compliance of Elastic Bodies in Contact. *ASME Journal of Applied Mechanics*, 16:259–268, 1949.

[61] M. Ciavarella. The generalized Cattaneo Partial Slip Plane Contact Problem. I–Theory. *International Journal of Solids and Structures*, 35(18):2349–2362, 1998.

[62] J. Jäger. A New Principle in Contact Mechanics. *Journal of tribology*, 120(4):677–684, 1998.

[63] O. Reynolds. On Rolling-Friction. *Philosophical Transactions of the Royal Society of London*, 166(0):155–174, January 1876.

[64] P.J. Vermeulen and K.L. Johnson. Contact of Nonspherical Elastic Bodies Transmitting Tangential Forces. *ASME Journal of Applied Mechanics*, 31:338–340, 1964.

[65] V.L. Popov and S.G. Psakhie. Numerical Simulation Methods in Tribology. *Tribology International*, 40(6):916–923, 2007.

[66] T. Geike. *Theoretische Grundlagen eines schnellen Berechnungsverfahrens für den Kontakt rauer Oberflächen*. PhD thesis, Technische Universität Berlin, 2008.

[67] V. L. Popov and M. Heß. *Method of Dimensionality Reduction in Contact Mechanics and Friction*. Springer, Berlin, Heidelberg, 2015.

[68] T. Geike and V. L. Popov. Mapping of Three-Dimensional Contact Problems into one Dimension. *Physical Review E*, 76(3):036710, 2007.

[69] M. Heß. *Über die Exakte Abbildung Ausgewählter Dreidimensionaler Kontakte auf Systeme mit Niedrigerer Räumlicher Dimension*. PhD thesis, Technische Universität Berlin, 2011.

[70] R. Pohrt, V. L. Popov, and A. E. Filippov. Normal Contact Stiffness of Elastic Solids With Fractal Rough Surfaces for One- and Three-Dimensional Systems. *Physical Review E*, 86(2):026710, 2012.

[71] R. Pohrt and V. L. Popov. Investigation of the Dry Normal Contact Between Fractal Rough Surfaces Using the Reduction Method, Comparison to 3D Simulations. *Physical Mesomechanics*, 15(5-6):275–279, 2013.

[72] S. Kürschner and V. L. Popov. Penetration of Self-Affine Fractal Rough Rigid Bodies Into a Model Elastomer Having a Linear Viscous Rheology. *Physical Review E*, 87(4):042802, 2013.

[73] A. V. Dimaki, A. I. Dmitriev, Y. S. Chai, and V. L. Popov. Rapid Simulation Procedure for Fretting Wear on the Basis of the Method of Dimensionality Reduction. *International Journal of Solids and Structures*, 51(25–26):4215–4220, 2014.

[74] E. Teidelt. *Oscillating Contacts: Friction Induced Motion and Control of Friction*. PhD thesis, Technische Universität Berlin, 2015.

[75] V. L. Popov and M. Heß. Method of Dimensionality Reduction in Contact Mechanics and Friction: a Users Handbook. I. Axially-Symmetric Contacts. *Facta Universitatis, Series: Mechanical Engineering*, 12(1):1–14, 2014.

[76] V. L. Popov. Basic Ideas and Applications of the Method of Reduction of Dimensionality in Contact Mechanics. *Physical Mesomechanics*, 15(5-6):254–263, 2012.

[77] J. B. Sampson, F. Morgan, D. W. Reed, and M. Muskat. Studies in Lubrication: XII. Friction Behavior During the Slip Portion of the Stick–Slip Process. *Journal of Applied Physics*, 14(12):689–700, 1943.

[78] E. Rabinowicz. The Intrinsic Variables Affecting the Stick-Slip Process. *Proceedings of the Physical Society*, 71(4):668, 1958.

[79] F. Heslot, T. Baumberger, B. Perrin, B. Caroli, and C. Caroli. Creep, Stick-Slip, and Dry-Friction Dynamics: Experiments and a Heuristic Model. *Physical Review E*, 49(6):4973–4988, 1994.

[80] J. Awrejcewicz and P. Olejnik. Analysis of Dynamic Systems With Various Friction Laws. *Applied Mechanics Reviews*, 58(6):389, 2005.

[81] R. I. Leine, D. H. van Campen, A. de Kraker, and L. van den Steen. Stick-Slip Vibrations Induced by Alternate Friction Models. *Nonlinear Dynamics*, 16(1):41–54, 1998.

[82] F. A. Tariku and R. J. Rogers. Improved Dynamic Friction Models for Simulation of One-Dimensional and Two-Dimensional Stick-Slip Motion. *Journal of Tribology*, 123(4):661–669, 2001.

[83] F. J. Elmer. Nonlinear Dynamics of Dry Friction. *Journal of Physics A: Mathematical and General*, 30:6057, 1997.

[84] D. Karnopp. Computer Simulation of Stick-Slip Friction in Mechanical Dynamic Systems. *Journal of Dynamic Systems, Measurement, and Control*, 107(1):100–103, 1985.

[85] P. Dupont, V. Hayward, B. Armstrong, and F. Altpeter. Single State Elastoplastic Friction Models. *IEEE Transactions on Automatic Control*, 47(5):787–792, 2002.

[86] P. R. Dahl. A Solid Friction Model. Technical Report ADA041920, The Aerospace Cooperation, El Segundo, CA, 1968.

[87] M. Ciavarella. Frictional Energy Dissipation in Hertzian Contact Under Biaxial Tangential Harmonically Varying Loads. *The Journal of Strain Analysis for Engineering Design*, 49(1):27–32, 2014.

[88] E. A. H. Vollebregt. *User Guide for CONTACT, Vollebregt & Kalker's Rolling and Sliding Contact Model*, 2014.

[89] K. Kunert. Spannungsverteilung im Halbraum bei Elliptischer Flächenpressungsverteilung über einer Rechteckigen Druckfläche. *Forschung auf dem Gebiet des Ingenieurwesens A*, 27(6):165–174, 1961.

[90] M. J. Puttock and E. G. Thwaite. Elastic Compression of Spheres and Cylinders at Point and Line Contact. Technical Report 25, Commonwealth Scientific and Industrial Research Organization, Australia, 1969.

[91] E. Jahnke and F. Emde. *Tables of Functions With Formulae and Curves*. Dover Publications, 1945.

[92] H. Poritsky. Stresses and Deflections of Cylindrical Bodies in Contact with Application to Contact of Gears and of Locomotive Wheels. *ASME Journal of Applied Mechanics*, 17:191–201, 1950.

[93] D. M. Tolstoi, G. A. Borisova, and S.R. Grigorova. Role of Intrinsic Contact Oscillations in Normal Direction During Friction. *Nature of the Friction of Solids*, page 116, 1971.

[94] B. Zohuri. Dimensional Analysis. In *Dimensional Analysis and Self-Similarity Methods for Engineers and Scientists*, pages 1–92. Springer International Publishing, 2015.

[95] D. Gross, W. Hauger, J. Schröder, and W. A. Wall. *Technische Mechanik 3*. Springer-Lehrbuch. Springer, Berlin, Heidelberg, 2012.

[96] S. H. Strogatz. *Nonlinear Dynamics and Chaos*. Westview Press, 1994.

[97] G. Golub and M. J. Ortega. *Scientific Computing*. B.G. Teubner, 1996.

[98] J. Kunz and M. Studer. Bauteilauslegung: Druck-Elastizitätsmodul über Shore-A-Härte Ermitteln. *Kunststoffe*, 6:92–94, 2006.

[99] D. J. Inman. *Engineering Vibration*. Prentice Hall, 2001.

[100] P. Meijers. The Contact Problem of a Rigid Cylinder on an Elastic Layer. *Applied Scientific Research*, 18(1):353–383, 1968.

[101] D. Nowell and D. A. Hills. Contact Problems Incorporating Elastic Layers. *International Journal of Solids and Structures*, 24(1):105–115, 1988.

[102] J. Dundurs and M. S. Lee. Stress Concentration at a Sharp Edge in Contact Problems. *Journal of Elasticity*, 2(2):109–112, 1972.

[103] Wacker Silicones. *RTV Silikonkautschuke - Kleben, Abdichten, Vergiessen und Beschichten*. www.wacker.com/cms/media/publications/downloads/6019_DE_1.pdf, 2015.

[104] R. J. Marks II. *Handbook of Fourier Analysis and Its Applications*. Oxford University Press, Oxford, 2008.

[105] Norm DIN EN ISO 178: Plastics - Determination of Flexural Properties, September 2013.

[106] D. Gross, W. Hauger, J. Schröder, and W. A. Wall. *Technische Mechanik 2*. Springer-Lehrbuch. Springer, Berlin, Heidelberg, 2012.

[107] Norm DIN 1319-3: Fundamentals of Metrology-Part 3: Evalutaion of Measurements of a Single Measurand, Measurement Uncertainty, 1996.

[108] Norm DIN 1319-4: Fundamentals of Metrology-Part 4: Evaluation of Measurements, Measurement Uncertainty, 1999.

[109] L. Papula. *Mathematik für Ingenieure und Naturwissenschaftler Band 3*, volume 4. Vieweg-Verlag, 2001.

[110] A. Björck. *Numerical Methods for Least Squares Problems*. SIAM, 1996.

[111] J. Wooldridge. *Introductory Econometrics: A Modern Approach*. Cengage Learning, 2008.

[112] J. L. Rodgers and W. A. Nicewander. Thirteen Ways to Look at the Correlation Coefficient. *The American Statistician*, 42(1):59–66, 1988.

[113] L. Fahrmeier, R. Künstler, I. Pigeot, and G. Tutz. *Statistik, der Weg zur Datenanalyse*. Springer Berlin Heidelberg, 2001.

[114] G. J. Park. *Analytic Methods for Design Practice*. Springer London, London, 2007.

[115] K. Siebertz, D. van Bebber, and T. Hochkirchen. *Statistische Versuchsplanung*. Springer Berlin Heidelberg, Berlin, Heidelberg, 2010.

[116] J. J. Kalker. The Computation of Three-Dimensional Rolling Contact With Dry Friction. *International Journal for Numerical Methods in Engineering*, 14(9):1293–1307, 1979.

[117] J. J. Kalker. A Fast Algorithm for the Simplified Theory of Rolling Contact. *Vehicle System Dynamics*, 11(1):1–13, 1982.

[118] J. J. Kalker. *Three-Dimensional Elastic Bodies in Rolling Contact*. Springer, October 1990.

[119] M.P. Allen and D.J. Tildesley. *Computer Simulation of Liquids*. Clarendon Press, Oxford, 1987.

Appendix A

Statistics

A.1 Analysis of the Experiments

A.1.1 Specification of Measurement Results

Experimental measurements are always subjected to some statistical deviations, which are caused, among other things, mainly by imperfections of the instruments and their operation. The specific value x_i of a measurement i differs from one another and thus scatters around the mean value $\bar{x}$, which is defined as the arithmetic mean of the particular measurements:

$$\bar{x} = \frac{1}{n} \sum_{i=1}^{n} x_i \ . \tag{A.1.1}$$

With increasing number of measurements, the arithmetic mean approaches the so-called expected value x_e. In order to evaluate the uncertainty of measurement, the standard deviation of the mean value is considered, which indicates how far the mean value of measurement differs from the true value x_e :

$$\sigma_{\bar{x}} = \frac{1}{\sqrt{n}} \sqrt{\frac{1}{n-1} \sum_{i=1}^{n} (x_i - \bar{x})^2} \ . \tag{A.1.2}$$

For $n \to \infty$ one can determine with the probability density $h(x)$ that the true value x_e lies within the range $\bar{x} \pm \sigma_{\bar{x}}$ with a probability of 68.3%. This range is defined as the confidence interval on the confidence level 68.3%. In case of only a few measurement values n, one has to use the so-called student-t distribution for the probability density $h(x)$. This is considered by the correction term t that is tabulated for instance in the DIN norm 1319-3 for different numbers of measurements n and for various confidence intervals [107]. A measurement result is then specified as follows:

$$x = \bar{x} \pm t\sigma_{\bar{x}} \ , \tag{A.1.3}$$

where t is taken from tables. Unless otherwise noted, the measurement results in the present work are given with confidence intervals on the confidence level 68.3%. In case

that a certain measurement variable y is a function G[1] of an arbitrary number m of uncorrelated variables x_k the uncertainty of measurement follows from the so called Gaussian error propagation law that is also defined in the DIN norm 1319-4 [108]:

$$\sigma_{\bar{y}} = \sqrt{\sum_{k=1}^{m} \left(\frac{\partial G}{\partial x_k} \right)^2 \sigma_{\bar{x}_k}^2} \; . \tag{A.1.4}$$

A.1.2 Identification of Parameters

Not all parameters of the experimental rigs are known or can be measured directly. Examples include the coefficient of friction μ, the elastic modulus of the substrate of the rolling body test rigs E_2 and the mapping parameter κ that occurs due to the violated rotational symmetry. In order to determine the unknown values the so called method of least squares is used. In the first step, the sum of the squared deviation between the measured variable y_i and the model function $f(x_i, \alpha_j)$ is computed:

$$S_j = \sum_{i=1}^{n} \left(f(x_i, \alpha_j) - y_i \right)^2 \; . \tag{A.1.5}$$

Here α_j denotes a specific set j of a number of model parameters in the model function and n is the number of observations or measurements. In the second step, the parameter set j for which the corresponding S_j is minimal is chosen for determination of the unknown parameters. The two basic assumptions for this approach are normally distributed measurement deviations of y_i and a correct measurement of the independent variable x_i. In practice this means that the measurement deviations of x_i must be small compared to those of y_i [109]. Linear model functions $f(x_i, \alpha_j)$ enable the analytical determination of both the minimum and the parameters α_j. Otherwise iterative methods are used [110]. However, in the present work mostly non-linear functions derived from physical principles are used for $f(x_i, \alpha_j)$, as for instance the static displacement of the substrate $U_{stat}(F_T, \alpha)$ with $\alpha = (E, \mu)$. Often, only one or two parameters occur in the functions. Thus it is useful to compute S_j for a sufficiently high resolution of α_j. The minimum can then easily be detected.

A.1.3 Curve Fitting and Regression

Curve fitting and regression are widely used instruments in many areas, particularly in econometrics, where a good introduction is given by Woolridge [111]. The aim is to construct a smooth function that approximately fits the given data x_i and y_i. For instance in a linear regression analysis the starting point is the model function:

$$y = \alpha x + \beta \; . \tag{A.1.6}$$

The coefficients α and β have to be determined such that the model function reflects the relation between x and y as good as possible. For this the least square method is used.

[1] Here G can be a known function or a guessed model function.

Based on the estimated parameters $\hat{\alpha}$ and $\hat{\beta}$ one can calculate the fitted value $\hat{y}_i$. The deviation between the fit $\hat{y}_i$ and each measured value y_i is called the residual δy_i:

$$y_i = \hat{y}_i + \delta y_i \ . \tag{A.1.7}$$

The goodness of the fit is determined by several measures. Besides others, the explained sum of squares (SSE) and the residual sum of squares (SSR) are important:

$$SSE = \sum_{i=1}^{n} (\hat{y}_i - \bar{y})^2 \ , \tag{A.1.8}$$

$$SSR = \sum_{i=1}^{n} \delta y_i^2 \ , \tag{A.1.9}$$

where $\bar{y}$ is the mean of all measured values.

Tab. A.1.1: quality of the curve fitting results

reference	fitted model function	SSE	R^2
(3.2.17)	$f_T = 1 - wu_{sd} - (1 - u_{sd})^{3/2}$	$3 \cdot 10^{-7}$	1
(3.3.2)	$\eta_{fit} = 4.77\sqrt{u_{stat}}$	0.257	0.986
(3.3.4)	$\Delta u = \sqrt{2\left(1 - (1 - f_T)^{2/3}\right)}\,(w - w_{lim})$	0.011	0.989
(3.4.8)	$f_T = 1 - 1.1wu_{sd} - (1 - u_{sd})^{3/2}$	$5 \cdot 10^{-4}$	0.999
(3.4.15)	$\Delta u = \sqrt{5\left(1 - (1 - f_T)^{2/3}\right)}\,(w - w_{\mathrm{lim}})$	0.048	0.975
(3.5.11)	$U_{stat} = U_0\Big(1 - \Big(1 - \frac{F_T}{\mu F_N}\Big)\Big)^{0.92}$	$3 \cdot 10^{-5}$	1
(3.5.12)	$U_0 = \mu\frac{2F_N}{\pi E^* L}\left(\frac{1}{2}\left(1 + \ln(4)\right) + \ln\left(1.8\frac{E^*}{G^*}\frac{L}{a}\right)\right)$	$4 \cdot 10^{-4}$	1
(3.5.26)	$u_{sd} = 1 - (1 - f_T)^{0.92} + 0.3f_T$	$7 \cdot 10^{-2}$	0.999
(3.5.28)	$w_{\mathrm{lim}} = 1 - f_{T,\mathrm{lim}}^{0.73}$	$2 \cdot 10^{-2}$	0.999
(3.5.29)	$u_{\mathrm{lim}} = f_{T,\mathrm{lim}}^{0.87}$	$5 \cdot 10^{-5}$	0.999
(3.5.30)	$\Delta u = 0.64 f_T\,(w - w_{\mathrm{lim}})$	$2 \cdot 10^{-3}$	0.95

SST and SSR define the coefficient of determination R^2 which is the ratio of the explained variation and the total variation:

$$R^2 = \frac{SSE}{SSE + SSR} \ . \tag{A.1.10}$$

The ratio R^2 is interpreted as the fraction of the sample variation in y that is explained by x. In case of a perfect fit all data points would lie on the model function, which yields $R^2 = 1$. A value of R^2 equal to zero indicates a poor fit. Table A.1.1 gives an overview of the different fits together with the SSE and R^2 values.

A.1.4 Correlations

The correlation coefficient measures the strength of the linear correlation of two variables x and y. One of the most common coefficients is the Bravais-Pearson product-moment correlation r, which is a dimensionless index that is invariant to linear transformation of either variable [112]:

$$r = \frac{\sum_{i=1}^{n} (x_i - \bar{x})(y_i - \bar{y})}{\sqrt{\sum_{i=1}^{n} (x_i - \bar{x})^2 \sum_{i=1}^{n} (y_i - \bar{y})^2}} \,. \tag{A.1.11}$$

Here $\bar{x}$ and $\bar{y}$ denote the mean value of a sample with n observations. Consider a diagram in which x_i depicts the horizontal coordinate and y_i depicts the vertical coordinate. The more the distribution of values of x_i and y_i resembles a straight line, the closer is r to 1 or -1 in case of a negative slope. It is important to know that the case $r \approx 0$ does not indicate no correlation but only indicates no linear correlation. In a coarse raster one can classify the correlation as [113]:

$$\begin{array}{rlll} & |r| & < 0.5 & \text{weak correlation} \,, \\ 0.5 \leq & |r| & < 0.8 & \text{medium correlation} \,, \\ 0.8 \leq & |r| & & \text{strong correlation} \,. \end{array} \tag{A.1.12}$$

But this raster strongly depends on the variable examined. Therefore, correlation coefficients are particularly useful as comparative measurements. They are rather from an exploratory and descriptive character. The following form of (A.1.11) is very useful for a revolving calculation of r as needed for simulations on the GPU:

$$r = \frac{\sum_{i=1}^{n} x_i y_i - n\bar{x}\bar{y}}{\sqrt{\left(\sum_{i=1}^{n} x_i^2 - n\bar{x}^2\right)\left(\sum_{i=1}^{n} y_i^2 - n\bar{y}^2\right)}} \,. \tag{A.1.13}$$

A.2 Design of Experiments

The term design of experiments (DoE) describes a specific method used for an efficient planning and execution of experiments with several parameters of influence [114, 115]. The intended area of application are experiments in the real world, where the experimentalist often lacks deep knowledge about the real underlying mechanisms of the examined system. The DoE then helps to fill this black box and enables to develop model functions. In the case of the micro-walking machine exists a precisely known numerical model. Thus, it is not necessary to consider the experimental principles of replication, randomization and blocking because the experimental conditions do not change. However, one can make good use of the evaluation methods. In the first step, the overall number of parameters is divided into two groups: *factors* whose influence is studied and all other parameters that are held constant. The different adjustments of the factors are called levels. In case of the basic principle of the DoE, the so-called full factorial

experimental schedule, every factor is varied and all possible combinations are taken into account. For n levels and k factors, the full-factorial schedule gives:

$$m = n^k \tag{A.2.1}$$

different combinations of parameters. For example, if one considers two factors a, b and two levels for each factor, this yields $2^2 = 4$ points in the parameter space as shown in Fig. A.1 (a). The experiment gives four different results y. The so-called main-effect $\bar{y}$ is a measure for the influence of a specific factor and is given by the mean for all combinations in which this factor is held constant. For example the main effect for the factor $a = a_1$ is given as:

$$\bar{y}_{a1} = \frac{1}{2} \left(y\left(a_1, b_1\right) + y\left(a_1, b_2,\right) \right) \ . \tag{A.2.2}$$

The so called main-effect plot summarizes all main effects as in Fig. A.1 (b). In addition, the interaction-effect plot shows the interaction between the different factors, as shown in Fig. A.1 (c). It gives the influence of a specific factor, b in this case, while the other factor is kept constant.

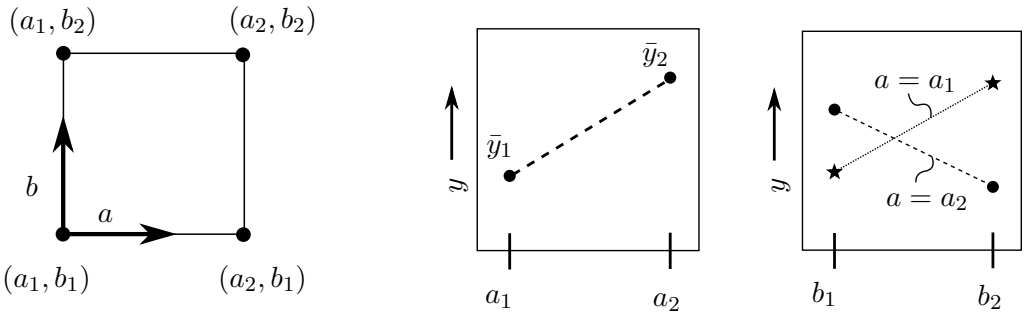

(a) parameter space (b) main effect (c) interaction effect

Fig. A.1: design of experiments (DoE). (a) parameter space. (b) main effect plot. (c) interaction effect plot

The drawback of the full factorial experimental schedule is the large number of factor level combinations in comparison to other methods of the DoE. However, as every experiment is only conducted once, the full-factorial schedule is used in the analysis of the parameters of influence of the micro-walking machine.

Appendix B

Numerical Methods

In order to carry out simulations of the different systems, several numerical models are used that are briefly discussed in the following section. Important algorithms are illustrated in pseudo-code-notation. Please refer to the given references for more detailed information on the methods used in this work.

B.1 Incremental MDR Simulation

One of the most important properties of the MDR model is the decoupling of the degrees of freedom of the elements of the foundation. Consequently, the numerical effort of the MDR system is of the order $\mathcal{O} = n$, where n gives the numbers of elements, i.e. degrees of freedom. In comparison, the numerical effort of the boundary element method (BEM), which is widely used in contact mechanics, is of the order $\mathcal{O} = n^4$. In this way, the MDR allows a very fine discretization with low computational complexity and enables detailed parameter identifications [67].
The oscillating rolling contact as introduced in section 3.1 is simulated with the MDR using a quasi-static incremental approach. Here, the rolling path W is divided into incremental steps with step-size ΔW. The displacement of the substrate U is then computed in every time step on basis of the equilibrium of forces. The simulation is divided into two parts, namely the rolling part and the deflection part.

Rolling Part On basis of the half-space assumption rolling only changes the normal displacement U_z. Thus, for an arbitrary spring at position s for step k this yields:

$$U_z\left(s,k\right) = d - \frac{\left(s \mp k\Delta W\right)^2}{R} \ , \tag{B.1.1}$$

$$f_z\left(s,k\right) = \Delta k_z U_z\left(s\right) \ . \tag{B.1.2}$$

Here $-k\Delta W$ in (B.1.1) simulates forward rolling and $+k\Delta W$ backward rolling. The corresponding contact region for step k is shifted as:

$$-a \pm k\Delta W \leq s \leq a \pm k\Delta W \ . \tag{B.1.3}$$

Displacement Part Firstly, the displacement is slightly increased so that the *test* displacement $\tilde{U}_x$ and the *test*-tangential force $\tilde{f}_x$ read:

$$\tilde{U}_x(s,k) = U_x(s,k-1) + \Delta U \ , \tag{B.1.4}$$

$$\tilde{f}_x(s,k) = \Delta k_x \tilde{U}_x(s,k) \ , \tag{B.1.5}$$

$$U(k) = U(k-1) + \Delta U \ . \tag{B.1.6}$$

Here $U_x(s,k-1)$ and $U(k-1)$ denote the *old* spring deflections respectively the *old* rigid body displacement. Given the test force, the stick and slip regions are identified on basis of the traction bound. The *new* displacements are then computed as:

$$\begin{array}{lll} \tilde{f}_x(s,k) \le \mu f_z(s,k) & \Rightarrow \text{stick-region:} & \Rightarrow U_x(s,k) = U_x(s,k-1) + \Delta U \ , \\ \tilde{f}_x(s,k) > \mu f_z(s,k) & \Rightarrow \text{slip-region:} & \Rightarrow U_x(s,k) = \mu \frac{E^*}{G^*} U_z(s,k) \ . \end{array} \tag{B.1.7}$$

Consequently, the *new* tangential forces result to:

$$f_x(s,k) = \Delta k_x U_x(s,k) \ . \tag{B.1.8}$$

In principle, rolling initially decreases the tangential force in the contact $F_x(k) = \sum f_x(s,k)$. This leads to an imbalance of the forces what in turn increases the displacement. Thus, the displacement step is repeated until:

$$F_x(k) \ge F_T(1-\varepsilon) \ , \tag{B.1.9}$$

where ε denotes the relative accuracy of the calculation. This loop is repeated for every single rolling step as shown in Fig. B.1, where the stepwise incremental simulation scheme is illustrated. In principle, the proposed scheme can be adapted to a system that takes into account the inertia of the contacting bodies, i.e. the macroscopic dynamics, as described in chapter 13 in the book of Popov and Heß[67].

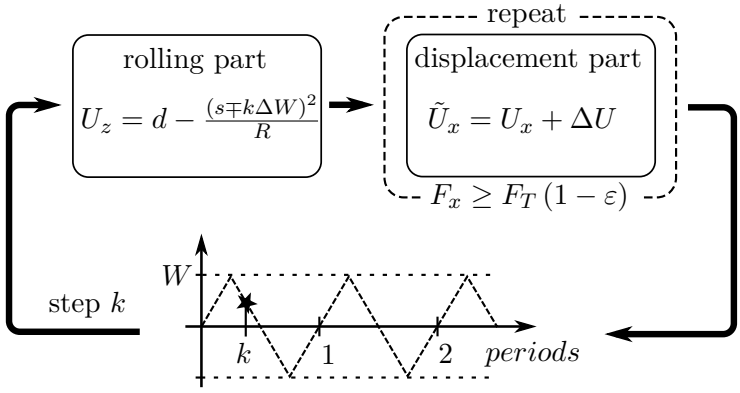

Fig. B.1: stepwise incremental simulation scheme for the oscillating rolling contact

B.2 CONTACT Simulation

In order to conduct a three-dimensional, quasi-static simulation of the oscillating rolling contacts, the well-known CONTACT software package is used, whose first version was released 1982. The program has since been continuously developed by the company *VorTech BV* and its fields of application have been expanded. It is freely available for academic use. The program implements the theories of rolling contacts by Kalker [116, 117, 118] and is based on the boundary element method (BEM). Here, the elasticity equations for the interior of the contacting bodies are transferred to equations for their bounding surfaces. Under the half-space assumption, the main resulting equation is the displacement and stress relation as given by the potential functions of Boussinesq and Cerruti, see section 2.1.1 and section 2.1.2. The code uses constant element discretization and the potential contact area is split into $mx \times my$ rectangular elements of size $\Delta x \times \Delta y$. The contact problem is solved using nested iteration processes. In case of a decoupled system the normal problem is solved first. As this gives the contact area and the traction bound, the tangential problem is solved subsequently. Here, the solver initially guesses a potential subdivision of stick- and slip area which is then updated on basis of contact conditions [88]. The iteration processes are based on a Newton-Raphson procedure, that (in this case) determines the indentation d and the tangential shift U on basis of the prescribed forces F_N and F_T. Once the requested relative accuracy ε is reached, the iteration process does not improve the solution any more. For tangential forces close to the maximum CONTACT lacks robustness [88] due to the non-linear dependence of total forces on creepages [55]. A so called world-fixed coordinate system is used in which the rolling body moves with velocity v in the x-direction and the particles in the contact area more or less stay at the same coordinate. The geometry of the contacting bodies is entered using a so-called Hertzian approach. Here, the initial distance between the undeformed surfaces $h(x, y)$ is entered directly. The rolling is then simulated as an incremental stepwise shift of the profile with ΔW being the step-size. In order to avoid inaccuracies or convergence problems ΔW should be comparable to the grid-size in the rolling direction Δx [88]. Because CONTACT has only a rudimentary graphical user interface (GUI), a MATLAB script is used to produce the text-based input files.

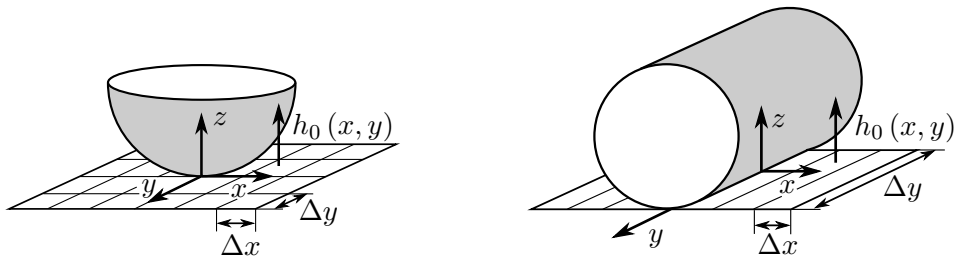

(a) spherical contact (b) cylindrical contact

Fig. B.2: numerical model of the CONTACT software. (a) spherical: discretization along the x- and y-direction. (b) cylindrical: just one line of elements along the x-direction

Spherical Rolling Contact For a rolling sphere the initial profile $h_0(x, y)$ reads:

$$h_0(x, y) = \frac{x^2}{2R} + \frac{y^2}{2R} . \tag{B.2.1}$$

In case of $w \parallel f_T$, the actual profile after k rolling steps reads:

$$h_k(x, y, k) = \frac{x^2}{2R} - \frac{k\Delta W}{R}x + \frac{(k\Delta W)^2}{2R} + \frac{y^2}{2R} . \tag{B.2.2}$$

For a mutual verification, the exact parameters of the experimental test rigs described in section 5.1.1 in Tab. 5.1.1 and in section 5.1.2 in Tab. 5.1.2 have been used. The number of elements varies with the amplitude due to the world fixed approach. For instance, with a grid-size of $\Delta x, \Delta y = 0.2$ mm and an incremental step size of $\Delta W = 0.2$ mm result 3050-4200 discretization elements. For the shakedown effect 10 periods of rolling are simulated resulting in 241-681 computation steps or $2 - 4\ h$ running time on a standard PC for each single parameter combination of f_T and w .

Cylindrical Rolling Contact For a rolling cylinder the initial profile $h_0(x, y)$ reads:

$$h_0(x, y) = \frac{x^2}{2R} , \tag{B.2.3}$$

and the actual profile after k rolling steps reads:

$$h_k(x, y, k) = \frac{(x + k\Delta W)^2}{2R} . \tag{B.2.4}$$

The cylindrical shaped roller with length L is modelled as a truncated $3D$ problem. This means that there is just one row of elements and all the contact quantities such as pressure or traction are constant along the y-direction. The numerical problem is thus two-dimensional[1] as depicted in Fig. B.2 (b). Again, the exact parameters of the experimental test rig described in section 5.1.3 in Tab. 5.1.3 have been used. The number of elements varies with the amplitude due to the world fixed approach. For a grid-size of $\Delta x = 0.02$ mm, $\Delta y = L$ and an incremental step size of $\Delta W = 0.02$ mm result 220-307 discretization elements. For each combination of f_T and w 10 periods of rolling are computed, resulting in 881-2641 computation steps or $1 - 2\ min$ running time on a standard PC per combination.

[1] The problem still resembles to the loading of a three-dimensional elastic half-space.

B.3 Time Integration

Newton's seconds law yields the general initial value problem for the motion of a mechanical system as:

$$\ddot{x}(t) = \frac{F(t)}{m} \quad \text{and} \quad x(0) = x_0, \quad \dot{x}(0) = v_0 \,. \tag{B.3.1}$$

The motion of the system can be computed using a stepwise numerical integration scheme. For the simple Euler method the solution is based on the difference quotients:

$$\dot{x} = \frac{x(t+\Delta t) - x(t)}{\Delta t} \quad \text{and} \quad \ddot{x} = \frac{\dot{x}(t+\Delta t) - \dot{x}(t)}{\Delta t} \tag{B.3.2}$$

what gives [97]:

$$\begin{pmatrix} x(t+\Delta t) \\ \dot{x}(t+\Delta t) \end{pmatrix} = \begin{pmatrix} x(t) \\ \dot{x}(t) \end{pmatrix} + \Delta t \begin{pmatrix} \dot{x}(t) \\ \frac{F(t)}{m} \end{pmatrix} \,, \tag{B.3.3}$$

where Δt denotes the time step. In rigid body dynamics one often uses multistep methods as the famous Runge-Kutta method [97]. Most of these classical procedures require knowledge of the exact time course of the force $F(t)$. This might be one reason for the widespread use of velocity dependent friction laws. However, in the present model the forces in the contact are a direct result of the spring displacements, thus the scheme proposed in (B.3.3) cannot be used. But this situation almost exactly corresponds to the situation in molecular dynamics (MD) where the forces that act on the molecules are a direct result of their actual relative position. This leads us to the commonly used Velocity-Verlet algorithm whose scheme is as follows [119]:

$$x(t+\Delta t) = x(t) + \Delta t \dot{x}(t) + \frac{1}{2}(\Delta t)^2 \frac{F(t)}{m} \,, \tag{B.3.4}$$

$$\dot{x}(t+\Delta t) = \dot{x}(t) + \frac{1}{2}\Delta t \left(\frac{F(t)}{m} + \frac{F(t+\Delta t)}{m} \right) \,. \tag{B.3.5}$$

The scheme enables to determine the new displacements first which then serve as input factors for the new forces $F(t+\Delta t)$.

B.4 Contact Models for the Micro-Walking Machine

Using the separation of space scales principle [65] as discussed in section 2.3.1, the contact spots of the micro-walking machine are modelled as linear springs as described in the sections 2.3.3 and 4.1.1. As the spring deflections in the normal and tangential directions directly depend on the actual motion of the rigid body, i.e. x, z and φ, a case distinction is being used to determine them. Here the subscript $(.)_{1/2}$ denotes the two contact spots, thus every case distinction is carried out separately for the two spots on the left (1) and the right (2) of the specimen.

Two-dimensional Contacts In the model described in section 4.1.1 each spring has one normal deflection $u_{z1/2}$ and one tangential deflection $u_{x1/2}$ aligned parallel in the z- and x-direction as in Fig. B.3 (a). Firstly, a *test* normal deflection $\tilde{u}_{z1/2}$ is computed:

$$\tilde{u}_{z1/2}(t) = z(t) \pm \kappa_3^{-1}\varphi(t) \ , \tag{B.4.1}$$

and it is checked whether a specific spring is released from the substrate:

$$\begin{array}{lll} \tilde{u}_{z1/2}(t) > 0 & \Rightarrow \text{spring in contact} & \Rightarrow u_{z1/2}(t) = z(t) \pm \kappa_3^{-1}\varphi(t) \ , \\ \tilde{u}_{z1/2}(t) \leq 0 & \Rightarrow \text{spring is released} & \Rightarrow u_{z1/2}(t) = 0 \ . \end{array} \tag{B.4.2}$$

After that, the tangential deflections $u_{x1/2}$ are computed via a second case distinction. For a sticking contact, the deflections are directly determined by the change of rigid body motion between the two time steps, i.e. Δx, Δz and $\Delta\varphi$. Thus, the *test* deflections are computed firstly:

$$\tilde{u}_{x1/2}(t) = u_{x1/2}(t - \Delta t) + \Delta x + \Delta\varphi \ , \tag{B.4.3}$$

where $u_{x1/2}(t - \Delta t)$ denotes the old deflections. If this *test* deflection exceeds the friction bound $\mu\kappa_2 u_{z1/2}(t)$, the contact slips. Consequently, the case distinction for the *new* tangential deflections reads:

$$\begin{array}{lll} |\tilde{u}_{x1/2}(t)| \geq \mu\kappa_2 u_{z1/2}(t) & \Rightarrow \text{spring slips} & \Rightarrow u_{x1/2}(t) = \mu\kappa_2 u_{z1/2}(t)\,\text{sign}\left(\tilde{u}_{x1/2}(t)\right) \ , \\ |\tilde{u}_{x1/2}(t)| < \mu\kappa_2 u_{z1/2}(t) & \Rightarrow \text{spring sticks} & \Rightarrow u_{x1/2}(t) = \tilde{u}_{x1/2}(t) \ . \end{array} \tag{B.4.4}$$

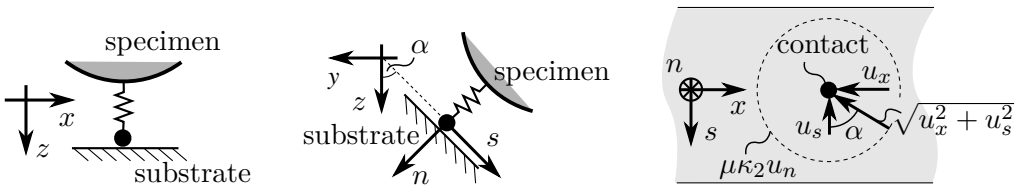

(a) 2D contact (b) 3D contact (c) topview

Fig. B.3: (a) contact model of initial model with linear spring. (b) contact model of the extended model with additional spring deflection u_s. (c) top view of the surface of the substrate of the extended contact model with friction bound $\mu\kappa_2 u_n$

Three-dimensional Contacts The contact geometry of the experimental specimen as introduced in section 5.2 differs slightly from the numerical model described in section 4.1.1. In order to identify appropriate parameter ranges and to enhance comparability an extended contact model is being used. The prism shaped substrate adds an additional deflection $u_{s1/2}$ to each spring. As shown in Fig. B.3 (b) and (c) $u_{s1/2}$ is aligned perpendicular to the normal deflection $u_{n1/2}$ as well as to the tangential deflection $u_{x1/2}$. The tangential stiffness of the two directions is the same as in the two-dimensional

contact, i.e. k_x in the dimensionful model. The normal direction of the contact is now inclined by 45° to the z-direction and the *test* normal deflection yields:

$$\tilde{u}_{n1/2}(t) = \frac{\sqrt{2}}{2}\left(z(t) \pm \kappa_3^{-1}\varphi(t)\right) . \tag{B.4.5}$$

The first case distinction reads:

$$\begin{aligned} &\tilde{u}_{n1/2}(t) > 0 \quad \Rightarrow \text{spring in contact} \quad \Rightarrow u_{n1/2}(t) = \tfrac{\sqrt{2}}{2}\left(z(t) \pm \kappa_3^{-1}\varphi(t)\right) , \\ &\tilde{u}_{n1/2}(t) \leq 0 \quad \Rightarrow \text{spring is released} \quad \Rightarrow u_{n1/2}(t) = 0 . \end{aligned} \tag{B.4.6}$$

Again, in case of sticking contacts, the deflections directly follow from the change of motion between the time steps, i.e. Δx, Δz and $\Delta\varphi$. This yields the tangential *test* deflections as:

$$\tilde{u}_{x1/2}(t) = u_{x1/2}(t - \Delta t) + \Delta x + \Delta\varphi , \tag{B.4.7}$$

$$\tilde{u}_{s1/2}(t) = u_{s1/2}(t - \Delta t) + \frac{\sqrt{2}}{2}\left(\Delta z - \kappa_3^{-1}\Delta\varphi\right) . \tag{B.4.8}$$

In case of slipping contacts, the friction bound $\mu\kappa_2 u_{n1/2}$ only gives the norm of the tangential deflections. Thus, one has to determine the angle $\alpha_{1/2}$ between $u_{x1/2}$ and $u_{s1/2}$ as shown in Fig. B.3 (c). With the test deflections $\tilde{u}_{x1/2}$ and $\tilde{u}_{s1/2}$, the case distinction for the three-dimensional contacts at time t thus finally reads:

$$\begin{aligned} &\sqrt{\tilde{u}_{x1/2}^2 + \tilde{u}_{x1/2}^2} \geq \mu\kappa_2 u_{n1/2} \quad \Rightarrow \text{spring slips} \quad \Rightarrow \alpha_{1/2} = \arctan\left(|\tfrac{\tilde{u}_{s1/2}}{\tilde{u}_{x1/2}}|\right) , \\ &\qquad\qquad \Rightarrow u_{x1/2} = \mu\kappa_2 u_{n1/2}\cos\left(\alpha_{1/2}\right) , \\ &\qquad\qquad \Rightarrow u_{x1/2} = \mu\kappa_2 u_{n1/2}\sin\left(\alpha_{1/2}\right) , \\ &\sqrt{\tilde{u}_{x1/2}^2 + \tilde{u}_{x1/2}^2} < \mu\kappa_2 u_{n1/2} \quad \Rightarrow \text{spring sticks} \quad \Rightarrow u_{x1/2} = \tilde{u}_{x1/2} , \\ &\qquad\qquad \Rightarrow u_{s1/2} = \tilde{u}_{s1/2} . \end{aligned} \tag{B.4.9}$$